EXPERIMENTAL EVALUATION OF A PROPULSIVE WING CONCEPT

BY

AARON TIMOTHY PERRY

THESIS

Submitted in partial fulfillment of the requirements
for the degree of Master of Science in Aerospace Engineering
in the Graduate College of the
University of Illinois at Urbana-Champaign, 2016

Urbana, Illinois

Adviser:

Assistant Professor Phillip J. Ansell

Abstract

The work presented in this thesis was performed in support of a NASA LEARN project which aimed to develop a novel propulsive wing airfoil section which could be applied to a future-generation high-efficiency aircraft in order to further improve gains in efficiency over current aircraft. The designed airfoil section extended the Griffith/Goldschmied airfoil concept to a Mach number of 0.7 for extended runs of laminar flow, pressure thrust, and wake filling. A low-speed wind tunnel test was performed using a model of the designed propulsive airfoil section in order to validate the tools which were used for design, as well as to verify the pressure thrust concept. Results from the airfoil test indicated that the suction-enabled airfoil was accurately modeled during the design phase. A large reduction of drag was also observed for the suction-enabled airfoil. Lift and drag compared well between computational predictions and experimental measurements for the airfoil test conditions. Experimental testing of a cross-flow fan was also performed in a transonic wind tunnel to characterize the fan power requirements and suction capabilities when embedded in a surface in transonic flow. Results from this test indicated that cross-flow fans are capable of aiding in pressure recovery, as well as producing a discrete pressure rise at the trailing-edge region of an airfoil. This pressure recovery and discrete pressure rise are are both necessary for the operation of the propulsive airfoil. Shaft power measurements were also taken during operation of the cross-flow fan, and results are presented to characterize the requirements of the fan over a variety of Mach number and RPM operating conditions. Finally, data from the cross-flow fan wind tunnel tests were scaled for use in a systems analysis which was also a part of the LEARN project.

To my wife Savannah

Acknowledgments

This work was sponsored by NASA LEARN grant No. NNX15AE39A. I would like to thank Hyun Dae Kim of the NASA Armstrong Flight Research Center and the NASA Aeronautics Research Institution, as well as professor Thong Dang of Syracuse University for providing guidance and CFD analysis with regards to the design of the cross-flow fan housing which was tested at the University of Illinois wind tunnel facilities.

I would also like to thank my advisor, Professor Phil Ansell, for guidance and support throughout the project, as well as for being willing to teach me how to operate the many different pieces of equipment which were used in this study. I would like to thank Brent Pomeroy for inspiring me to continue my education through his mentoring during my undergraduate studies, as well as for all of the MATLAB knowledge which I have learned from him. I would like to thank my fellow lab group members who helped out during my wind tunnel entries, specifically Rohit, Elle, and Cody. Thanks also goes to Yukti, an undergraduate student who assisted with some of my data processing. I would also like to thank my parents, who have played an enormous role in my education, and who have always been there to encourage me. I would finally like to acknowledge and thank my wonderful wife Savannah for being so supportive of my research efforts and for being my best friend that I know I can always count on.

Table of Contents

List of Tables

List of Figures

Nomenclature

Symbols

English

A	=	Area
b	=	span
c	=	chord length
C	=	polynomial constants
C_d	=	airfoil drag coefficient
C_l	=	airfoil lift coefficient
C_m	=	airfoil quarter-chord pitching moment coefficient
C_p	=	pressure coefficient
C_p^*	=	critical pressure coefficient
D	=	drag
D_o	=	fan diameter
f	=	general flow property
F	=	force
h	=	altitude, height
i	=	index number
l	=	length
L	=	lift, length
M	=	Mach number, moment
P	=	pressure of air, power
q	=	dynamic pressure
R	=	gas constant for air

Re = Reynolds number

t/c = thickness to chord ratio

T = temperature of air

U = wake velocity

U_o = fan tip speed

V = velocity, voltage

V/V_∞ = ratio of blowing/suction velocity to freestream velocity

W_s = shaft work

x = Cartesian coordinate in the horizontal direction

x/c = chord-wise location

y = Cartesian coordinate in the vertical direction

Greek

α = angle of attack

γ = heat capacity ratio

Δ = a difference between two quantities

λ = power coefficient

μ = dynamic viscosity

π = constant equal to 3.14159...

ρ = air density

τ = torque

ϕ = flow coefficient

ω = rotational speed

Subscripts

A = axial force component

ac = aircraft

amb = ambient condition

$c/4$ = quarter-chord location

$crit$ = critical Mach number condition

N = normal force component

ss = settling section

ts	=	test section
o	=	stagnation condition
$op, oper$	=	operating condition for hotwire probe
r	=	reference calibration condition
$rake$	=	pertaining to the wake rake
w	=	wake condition
∞	=	freestream condition

Superscripts

$(')$	=	force or moment per unit span

Abbreviations

CFF	=	cross-flow fan
CFD	=	computational fluid dynamics
CFM	=	cubic feet per minute
CNC	=	computer numeric control
ES	=	expansion surface
ESP	=	electronically-scanned pressure unit
HBWB	=	hybrid blended wing body
NLF	=	natural laminar flow
PID	=	proportional integral derivative controller
RPM	=	revolutions per minute
SFW	=	subsonic fixed wing
SLA	=	stereolithography
UAV	=	unmanned aerial vehicle
UIUC	=	University of Illinois at Urbana-Champaign
VFD	=	variable frequency drive
VI	=	virtual interface

Chapter 1

Introduction

1.1 Introduction to the Propulsive Wing Project

The NASA Subsonic Fixed Wing (SFW) project has defined a series of goals to be met by the next three generations of aircraft. Several of the specific goals listed for the N+3 generation (2025 time-frame) include a -71 dB noise reduction, an 80% reduction in NOx emissions, and an overall 60% reduction in mission energy expenditure [1]. All of these reductions are in reference to the current state-of-the-art commercial transport aircraft capabilities. In order to meet these ambitious goals, significant advancements will need to be made in aerodynamics and propulsion technologies, along with new methods to better integrate them within an airframe. Several groups have put significant effort into the development of alternative airframe configurations in an attempt to meet these goals, including the NX-3 hybrid blended wing body (HBWB), the D8 Double Bubble wide lifting fuselage configuration [2], and the Boeing SUGAR aircraft series [3]. Recent work on the development of the NX-3 has shown a promising decrease in fuel burn and noise for the configuration as compared to current aircraft. The NX-3 utilizes two conventional turboshaft generators to power an array of electric motors which are spread across the body of the aircraft [4]. While this hybrid-electric configuration allows for a more synergistic integration of the propulsion systems with the airframe, further improvements could be made to such a configuration by the integration of the propulsion system into the design of the wing sections.

The concept of a propulsive wing section has its origin in the original development of natural laminar flow airfoils with a discontinuous pressure rise, as first suggested by Griffith in the 1940's. The Griffith wing section was relatively thick ($t/c = 30\%$), and was designed with a favorable pressure gradient along most of the upper surface. This extended favorable pressure gradient led to long runs of laminar flow and therefore a reduction in skin friction drag. A suction slot located slightly upstream of the trailing edge region was used to provide a discontinuous pressure recovery for the airfoil. Wind tunnel tests were performed which verified the Griffith concept [5]. The concept was further developed by Goldschmied who utilized a similar airfoil (designed for an axisymmetric airship configuration) with the addition of mass flow ejection out of the trailing edge. During wind tunnel testing of the axisymmetric body, it was observed that, due to the sharp pressure rise at the suction slot, the static pressure on the aft portion of the airship was greater

than that at the front. This pressure difference led to a static pressure thrust which was responsible for negating a large portion of the airship total drag [6, 7]. The ejection of mass flow out of the trailing edge also contributed an additional component of thrust. During his wind tunnel investigation, Goldschmied was able to demonstrate a net drag value of zero on the axisymmetric body. This pressure thrust concept has since been verified by several other tests, and several thick-winged general aviation aircraft as well as a span-loader cargo aircraft have been conceptually developed using the Griffith/Goldschmied airfoil concept [8].

One factor which has limited the application of such a propulsive wing on a transonic aircraft is the fact that the Griffith/Goldschmied airfoil sections are all very thick. This thickness severely limits the application of such an airfoil to modern aircraft due to the corresponding low critical Mach numbers typically associated with a thick wing section. For example, the Goldschmied spanloader had $M_{crit} = 0.45$ [8]. Recent work has shown, however, that long runs of laminar flow due to favorable pressure gradients can be achieved with transonic airfoils that have a lower t/c, such as a design by Cella et al. which achieved up to 40% laminar flow on the upper surface of the airfoil at $M = 0.75$ [9]. These results suggest that it would be possible to extend the Griffith/Goldschmied airfoil concept into the transonic regime for use on transport aircraft.

A second significant issue preventing the application of such an airfoil to modern aircraft has been the lack of a good method for providing the required suction-based pressure recovery and trailing-edge mass flow ejection. The use of traditional axial fan propulsion does not lend itself to this application since studies have shown that such fans are sensitive to boundary layer ingestion and do not perform well under high back pressure [10, 11]. A concept which shows promise for this type of application is the cross-flow, or transverse fan. Cross-flow fans offer several advantages over axial fans when considered to provide suction and wake filling for such an airfoil concept. First, such a fan could easily be incorporated into the trailing edge of a wing to provide suction and blowing for the airfoil sections. Hancock [12] and Harloff and Wilson [13] first introduced the cross-flow fan to aviation. Since then, several studies have integrated cross-flow fans into airfoil sections as a means of providing circulation control, flow attachment, and reduced drag for a variety of flight speeds [14, 15]. Second, they have been shown to be far more effective at handling large back pressures than axial fans. Additionally, experimental work has shown that adiabatic compression efficiencies of up to 80% can be achieved [12]. While this efficiency is lower than what can be achieved by an axial fan, the benefits gained through aero-propulsive integration can offset this difference [16]. High fidelity CFD work has also shown that cross-flow fans are insensitive to boundary layer ingestion and inlet distortion issues that are common with axial fan configurations [17]. The potential for cross-flow fans to be driven by electric power also lends itself well to a hybrid electric distributed propulsion aircraft configuration.

The current study was performed in support of a NASA LEARN project which aimed to develop a transonic Griffith/Goldschmied airfoil section which utilizes a cross-flow fan to provide suction and wake filling. The resultant

airfoil could be incorporated into a wing section of a next-generation aircraft concept, such as the HBWB, to further reduce mission power consumption. High fidelity, state-of-the-art CFD simulations and inverse design methods were used to design a transonic airfoil section utilizing the Griffith/Goldschmied concept for increased laminar runs, reduced pressure drag, and wake filling. A full systems level analysis was also performed to compare mission power consumption between a baseline aircraft and an aircraft equipped with the transonic Griffith/Goldschmied section. The airfoil design and systems analysis portions of the study were performed by other members of the NASA LEARN project team, and are therefore not included as a part of this thesis. For more details on these additional aspects of the study, the reader is referred to Ref. 18.

The focus of this thesis is a series of wind-tunnel tests which were performed at the University of Illinois in support of the NASA LEARN project. These tests included a low-speed test of the designed airfoil section with the application of suction and blowing, as well as a transonic test of a cross-flow fan embedded within the wall of a modified supersonic wind tunnel. The equipment and methods which were utilized during the wind tunnel testing are discussed in Chapter 2, and the results of the tests are discussed in Chapter 3.

1.2 Cross-flow Fan Background Information

In order to provide a better understanding of cross-flow fans and how they function, a review of relevant literature was performed. This literature review includes a discussion of the various factors which influence the performance of such fans, as well as a summary of the various applications for which they have been utilized or suggested.

Cross-flow fans, also known as transverse fans, have their origins in the HVAC industry and were first patented by Mortier in the 1890's [13, 16, 19]. Their traditional use in this industry stems from the ability to easily incorporate such a fan within the ducting of an HVAC system due to the compactness of its geometry, as well as the ability for the fan to support a higher pressure difference than a traditional axial fan [19]. A cross-flow fan consists of two major parts. The first of these parts is the fan itself, which is an impeller-type fan that can be thought of as a cylinder where the circular circumferential wall has been replaced by a series of arced blades. An image and a diagram of a representative cross-flow fan are shown in Figure 1.1. The important geometric features which play a role in determining the performance of the fan are the blade outer diameter to inner diameter ratio, the number of fan blades, and the outer diameter and span of the fan. The shape of the blades also plays a role in determining the performance of the fan, though less work has been performed regarding the design of the blades due to the high cost of custom manufacturing.

The second major part of a cross-flow fan is its housing. The fan housing is composed of a rear wall and a vortex wall which serve to fix the locations of several important flow features (to be discussed). Some cross-flow fan housing designs also incorporate a primary vortex chamber on the vortex wall and a secondary vortex chamber on the rear wall.

The purpose of these chambers will also be discussed later. The design of the housing determines several important geometric properties related to the performance of the fan. The first of these is the creation of two discrete arcs of the fan which can be labeled as the inlet and outlet arcs. The inlet arc of the fan is the portion of the fan between the rear wall and vortex wall which is exposed to the incoming flow, and the outlet arc serves as the exit from the fan. In this sense, a cross-flow fan is similar to a two-stage compressor, where both the inlet and outlet arc of blades perform work on the flow as it is moved through the fan [16]. The ratio of the lengths of the inlet and outlet arcs can be used as one of the parameters governing the flow contraction of the fan. A second feature defined by the housing is the gap size between the fan outer diameter and the vortex and rear walls, usually expressed as a percentage of the fan diameter. Varying the size of the gap creates a trade-off in fan efficiency and noise production [16].

The aerodynamics of cross-flow fans are neatly summarized by Dang [16]. The important flow features relative to the performance of such fans are discussed here. The housing of the fan is the most crucial component towards determining the performance of the fan. In the absence of a housing, the fan will simply produce an eccentric vortex which revolves around the axis of the fan. The vortex wall of the fan housing serves to lock this rotating vortex into place, and thus creates one of the primary flow features of the cross-flow fan. Figure 1.1 (b) shows a diagram detailing the various flow regions within a cross-flow fan. In addition to the vortex region (*I* in the figure), a paddle-through (or secondary vortex) region is present near the rear wall of the fan (*II* in the figure). In both the primary and secondary vortex regions of the fan, no useful work is performed on the fluid. While the presence of these regions is not desirable, their existence is inherent to the operation of cross-flow fans and cannot be avoided. The region between these two flow features is referred to as the throughflow region, where fluid is accelerated through the center portion of the fan (*III* in the figure) [12, 16]. Another important aspect of the flow through a cross-flow fan is the direction of the entering and exiting flow. Figure 1.1 (b) shows vectors indicating the direction of flow at the inlet and outlet arcs of the fan. It has been observed that the fan performs most effectively when the flow tends to enter the inlet arc stage radially, and exit the outlet arc stage tangentially. It is therefore important when designing a cross-flow fan housing to ensure that the housing allows these to flow characteristics to be satisfied.

It is common in the literature to use several non-dimensional parameters to characterize the performance of cross-flow fans. Although the definitions may vary between authors, the most common parameters are a flow coefficient, a pressure coefficient, and some type of fan efficiency. The flow coefficient represents a mass flow parameter for the fan, which is typically a function of the ratio of the freestream velocity to the fan tip speed [12, 13, 15, 16]. The mass flow of the fan can also be quantified by simply using a corrected mass flow rate as in the work of Schreiber [20]. For operation in the range of best pressure ratio, values of the flow coefficient are typically between 0.6 and 0.8 [16], although the value may vary slightly depending on the specific definition of the coefficient. The pressure coefficient represents the rise in total pressure across both stages of the cross-flow fan. Typical values of this coefficient as defined

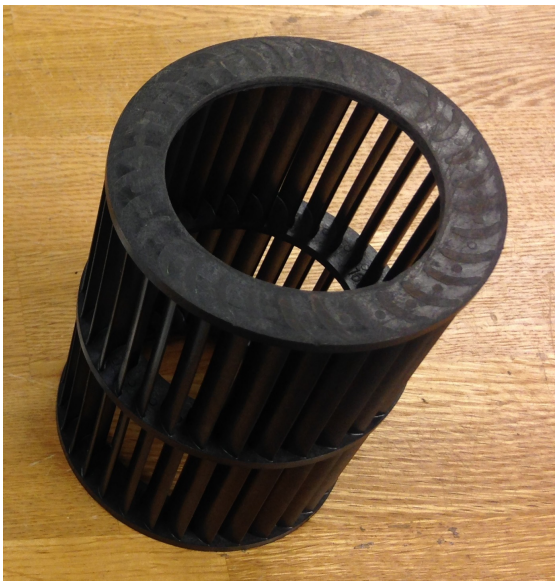

(a)

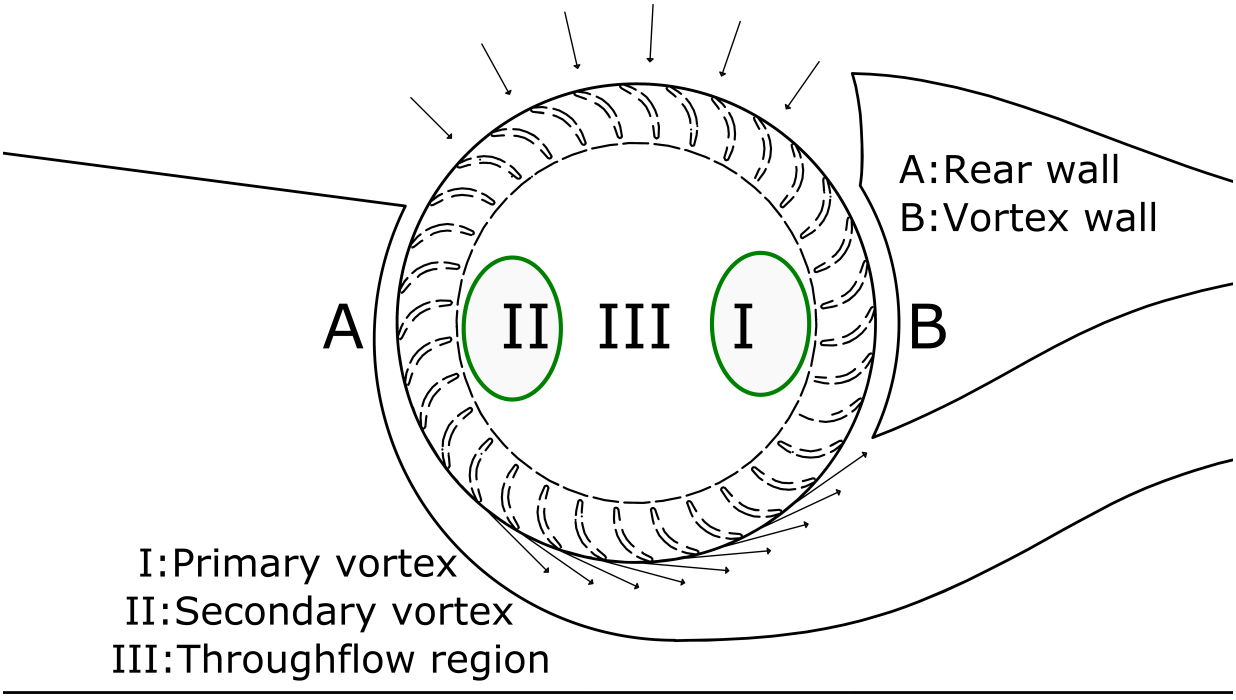

(b)

Figure 1.1: (a) An image of the cross-flow fan used in this study, and (b) a representative fan and housing cross section.

by Dang range between 2 and 2.5. Several different measures can be used to quantify the efficiency of a cross-flow fan. Common among the literature are the use of an adiabatic compression efficiency, a propulsive efficiency, and a

simple total efficiency. The total efficiency values which can be obtained by a carefully designed cross-flow fan are discussed in the following paragraph.

The use of cross-flow fans in the aviation industry was originally thought to be non-beneficial due to the seemingly low efficiencies of the fans. A 1980 study by Hancock demonstrated fan efficiencies near 50% for the baseline fan design used in the study. After a thorough redesign, however, Hancock was able to achieve a fan efficiency of nearly 80% by eliminating unnecessary curvature of the flow in the exit duct, as well as creating equal area inlet and outlet arcs for the fan to prevent adverse pressure gradients from reducing the performance of the inlet arc of the fan. Additional work by Harloff and Wilson also indicated that efficiencies in the upper 70% range could be obtained with a carefully designed fan and housing combination [13]. Although these efficiencies are still low compared to axial fan efficiencies, the benefits which can be gained by performing aero-propulsive integration as well as several characteristics of the fans such as their ability to support a greater pressure difference than axial fans can provide a substantial offset to the lower efficiency of the cross-flow fan [16].

Much of the knowledge which led to the creation of a cross-flow fan design which could reach an efficiency near 80% was gained through various experiments in which geometric parameters of the cross-flow fan and its housing were varied. Work by Hancock investigated the effect of varying the size of the primary and secondary vortex cavities, which were included to alleviate some of the losses associated with the vortex and paddle-through regions of flow within the cross-flow fan. Improvements in efficiency were seen when the size of the secondary cavity was decreased. Hancock also investigated the use of a guide vane in the exit duct of the fan, which did prove to create a more even distribution of total pressure across the duct, but did not provide any overall performance gains due to frictional losses. Finally, Hancock was able to achieve a high-efficiency design by reducing the inner to outer blade diameter ratio from 0.9 to 0.7, as well as by providing equal arc lengths exposed to the flow at both the inlet and the exit [12]. Harloff also performed a series of 800 test runs varying fan blade parameters such as the outer and inner blade angles, the blade diameter ratio, and number of blades. Housing parameters such as the secondary and primary vortex cavity size, inlet and outlet arc lengths, and exit duct height were all varied. Results of the test showed that efficiencies of up to 80% can be obtained [13]. Schreiber compared the performance of two cross-flow fans of different spans and determined that there was little difference in the per-unit-span performance parameters between the two cases. The only major difference was that the shorter fan could be run at a higher rpm due to its greater structural rigidity, and the longer span produced slightly more mass flow (the shorter span produced 86% of the mass flow per unit span produced by the longer span) [20].

The application of cross-flow fans to aircraft systems has its own place in the literature, beginning with Ackeret in the 1930's who suggested the use of a cross-flow fan for energizing the boundary layer of a thick airfoil section to reduce drag [21]. The application of cross-flow fans to thick airfoil sections has since been investigated by numerous

researchers. One notable series of studies was performed by Dang, Dygert, and Kummer [15, 19]. Computational methods were first utilized to design a modified Gottingen 570 airfoil which had a 34% thickness to chord ratio. The cross-flow fan was embedded in the trailing edge of the airfoil, with a cusp extending into the freestream flow above the fan. The cross-flow fan was used to provide flow attachment at large angles of attack, as well as to provide circulation control and a wake-filling propulsive effect. As a result of the flow attachment an circulation control, lift coefficients on the order of 6.5 were obtained. The designed airfoil was tested in a wind tunnel at a Reynolds number of 170,000 for verification. The same flow attachment and circulation control characteristics which were predicted by CFD were also observed in the wind tunnel test. The application of cross-flow fans to thick airfoil sections has also led to the development of several fan wing UAV-scale aircraft. Notable among this category are the FanWing and Propulsive Wing companies which have both developed flying prototypes of a thick-winged UAV completely powered by a cross-flow fan. Figure 1.2 shows an image of one such concept applied to a cargo aircraft. Computational work has also been performed in support of the development of fan wing type aircraft [22]. Due to the thick wing sections and the circulation control used to obtain very high lift coefficients, the flight speed of these aircraft is quite low, limiting their viability for commercial use [16].

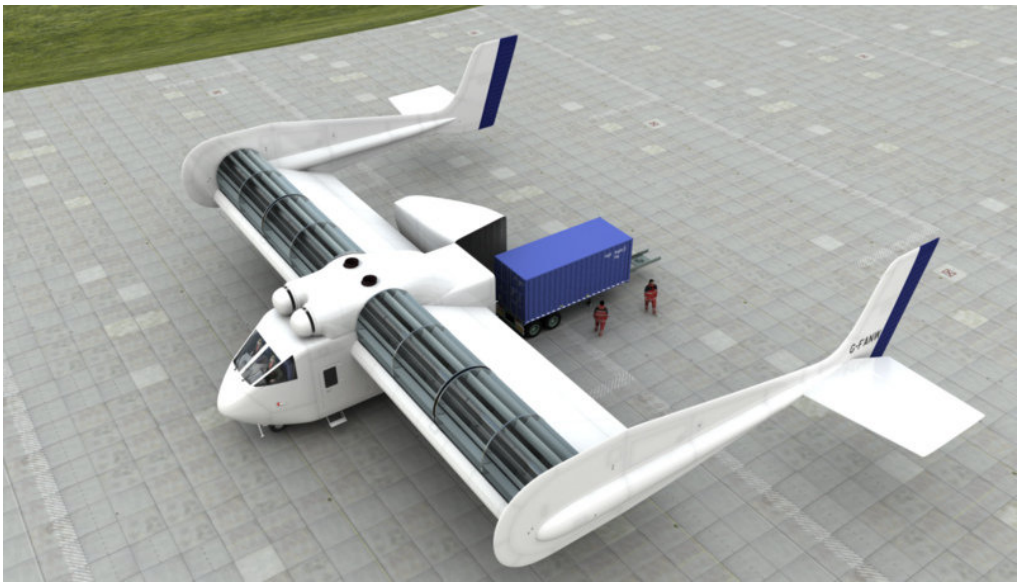

Figure 1.2: An image of a fanwing concept taken from www.fanwing.com.

Cross-flow fans have also gained attention for use in higher speed applications such as regional transport aircraft. This interest began in the 1970's with work from Hancock for the Lockheed-Georgia company. Several configurations were proposed to implement a cross-flow fan near the trailing-edge portion of a wing. In these configurations, the inlet to the fan was located on the upper surface of the airfoil to allow ingestion of the low-momentum boundary layer. The cross-flow fan was then used to energize the flow and provide blowing for either a Coanda flap or a

jet flap [12]. This work was further expanded upon by Gologan [14], who suggested three different trailing-edge implementations which could be used for both low-speed and high-speed applications. These implementations focused more on mechanisms which could be used to deploy the cross-flow fan/flap systems and adjust themselves depending on the speed of the aircraft. Simulations were also performed on a 15% thick airfoil section utilizing the same trailing edge implementation studied by Dang, Dygert, and Kummer. The results of these simulations were used to estimate the lift and drag coefficients which could be obtained on a regional transport aircraft using the CFF system. The modeled aircraft obtained a lift coefficient of 3.8 and a drag coefficient of -0.26, showing that the application of cross-flow fans could be beneficial for transport aircraft. Finally, work has been performed by Kummer developing a boundary layer ingestion system utilizing cross-flow fans in conjunction with axial fan propulsion on a hybrid blended wing body aircraft. This work has shown that when implemented in conjunction with axial fan propulsors to serve as a boundary-layer ingestion system, increases in the efficiency of the axial fans can be produced due to reduced inlet distortion effects [23].

Chapter 2

Experimental Methods

This chapter describes the experimental methods, testing equipment, and facilities which were used for both the low-speed and transonic wind tunnel tests. The transonic wind tunnel tests were performed in both Aerodynamics Laboratory A and the Aerodynamics Research Laboratory at the University of Illinois. Testing began in Aerodynamics Laboratory A, but was completed in the Aerodynamics Research Laboratory due to a transition of the tunnel facility from one laboratory to the other. The low-speed wind tunnel tests were all performed at the Aerodynamics Research Laboratory at the University of Illinois at Urbana-Champaign.

2.1 Transonic Wind Tunnel Testing

Wind-tunnel testing of a cross-flow fan was performed to characterize the performance of the fan when embedded in a surface in transonic flow. This section describes the wind tunnel facility, the design of the test setup, and the data acquisition equipment and data reduction methods which were used during the transonic testing of the fan.

2.1.1 Wind Tunnel Facility

Experimental testing of the cross-flow fan (CFF) was performed at the University of Illinois in the 5" $\times$ 5" Large Rectangular Supersonic Tunnel (LRST) facility [24]. The tunnel was originally configured with a converging-diverging nozzle designed for Mach 2 flow, driven by a compressed air tank farm pressurized to 150 psi. The tank farm was pressurized by an Ingersoll-Rand SSR-HPE300 compressor which utilized an Ingersoll-Rand DBP-1050 dryer to ensure that the compressed air was free of moisture. The tunnel was also equipped with a honeycomb flow straightener to improve the quality of flow through the tunnel. A 6" Flowserve Valtek Mark One pneumatic control valve was used to set the stagnation pressure of the tunnel, controlled with a PID controller in LabVIEW. The tunnel was equipped with a pitot pressure probe to measure the stagnation pressure in the chamber at the tunnel inlet, and a static pressure tap located in the test section region to measure the static pressure. Measurements of both of these pressures were made with two new Omega PX409-EH high accuracy 30 psi range pressure transducers. The purchase of these new pressure transducers was necessary as the original transducers had a 100 psi range and did not provide accurate read-

ings in the pressure range typical of transonic flow. A pitot tube was also connected to the compressed air supply pipe upstream of the gate value to allow for measurement of the tank pressure. A high capacity Omega PX309-200A5V pressure transducer was used to measure the tank pressure. An Omega TJ72-ICSS-116E-4 J-type thermocouple was also located in the stagnation chamber (next to the total pressure probe) to measure the tunnel total pressure [24].

The test section freestream Mach number, M_∞, was computed based on the measured stagnation pressure and test-section static pressure. With the assumption that the flow between the stagnation chamber and the test section was isentropic, Eq. 2.1 could be used to compute the freestream Mach number.

$$M_\infty = \sqrt{\frac{2}{\gamma - 1}\left[\left(\frac{P_o}{P_{ts}}\right)^{\frac{\gamma-1}{\gamma}} - 1\right]} \tag{2.1}$$

where P_o is the stagnation pressure, P_{ts} is the test-section static pressure, and γ is the ratio of specific heats for air. Since the PID controller was designed to control the stagnation pressure, it was necessary to specify a desired stagnation pressure which corresponded to the desired freestream Mach number. During tunnel operation, the computed Mach number was displayed by the LabVIEW virtual interface, and adjustments could be made to the desired stagnation pressure to ensure that the desired Mach number was achieved.

2.1.2 Modifications to the Wind Tunnel Facility

In order to utilize the tunnel for transonic flow, several modifications were made to the wind tunnel and associated instrumentation. The original converging-diverging nozzle would no longer suffice since it would not be able to provide good flow quality in the transonic regime. A new converging-only nozzle was designed to address this issue. The new nozzle required a smooth transition between the inlet height of 8" at the stagnation chamber and the test section height of 5". A fifth degree polynomial, given by Eq. 2.2, was chosen to represent the contour of the nozzle [24]. The polynomial was chosen as such to ensure a smooth transition to and from the contoured portion of the nozzle. The inflection point of the converging nozzle was located at half of the nozzle length [24].

$$y(x) = h\left[10\left(\frac{x}{L}\right)^3 - 15\left(\frac{x}{L}\right)^4 + 6\left(\frac{x}{L}\right)^5\right] \tag{2.2}$$

In Eq. 2.2, L = 10" is the length of the converging nozzle, and h = 3" is the height of the converging nozzle. The length of the nozzle was chosen to match the length of the converging portion of the previously installed Mach 2 nozzle. The new nozzle section was machined out of 6061 aluminum using a wire EDM cutter. A plot of the nozzle contour is shown in Figure 2.1.

A custom test section was also machined out of 6061 aluminum to allow the cross-flow fan to be embedded in the tunnel wall. The rear wall of the fan housing was incorporated into the test-section piece such that when the fan

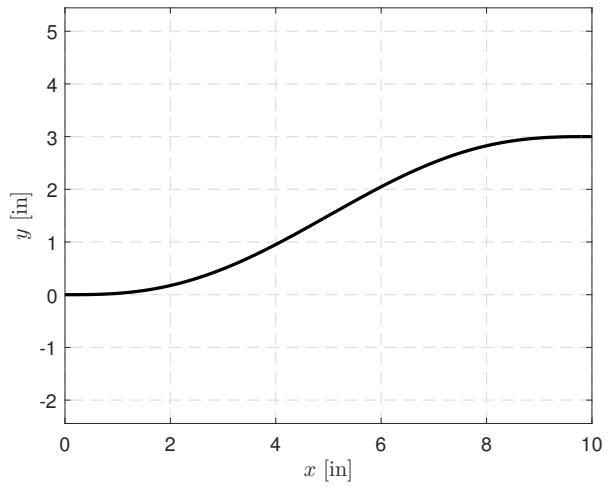

Figure 2.1: A graph of the spline used for the converging nozzle.

vortex wall and expansion surface were in place, the fan was embedded within the wall forming an inlet and outlet duct. Two iterations of the combined fan and housing design were performed in order to attain a fan setup which could properly supply suction through the inlet duct and blowing out of the exit duct. The details of these designs are discussed further in Section 2.1.3. The test section was also equipped with two 0.25" in diameter access holes through to the bottom of the wind tunnel to allow for probe access to the fan inlet and outlet ducts.

New tunnel side windows were also manufactured to allow for proper mounting of the cross-flow fan. The tunnel was designed with windows for optical access on either side of the test section, as well as laser sheet optical access in the test section ceiling. The two side windows were re-designed to allow for mounting of the cross-flow fan and the fan pulley drive assembly. One of the windows, which shall subsequently be referred to as the back window, was comprised of solid 6061 aluminum and was designed such that the fan pulley drive system and power measurement device could be mounted on the window outside of the wind tunnel. The front window consisted of a 6061 aluminum frame with a 1" thick 8" $\times$ 11" Plexiglas viewing region. Both of the windows were outfitted with embedded bearings to support the cross-flow fan shafts and allow for smooth rotation. The bearings were 22 mm in diameter and 7 mm deep, and were designed to support an 8 mm shaft. Both of the windows also had through-holes to allow for support of the expansion surface piece from both of its ends. The front window was also equipped with a hole to allow for polyurethane pressure tubes to attach to the expansion surface through the window for pressure tap measurements. A rendering of the tunnel showing the front-side window distanced from the tunnel is shown in Figure 2.2.

A cross section of the wind tunnel in its new configuration is shown below in Figure 2.3. The flow is from left to right, and the nozzle and test-section portions are shown as separate entities in the wind tunnel. Also shown in the diagram is the fan housing/expansion surface which is further discussed in Section 2.1.3.

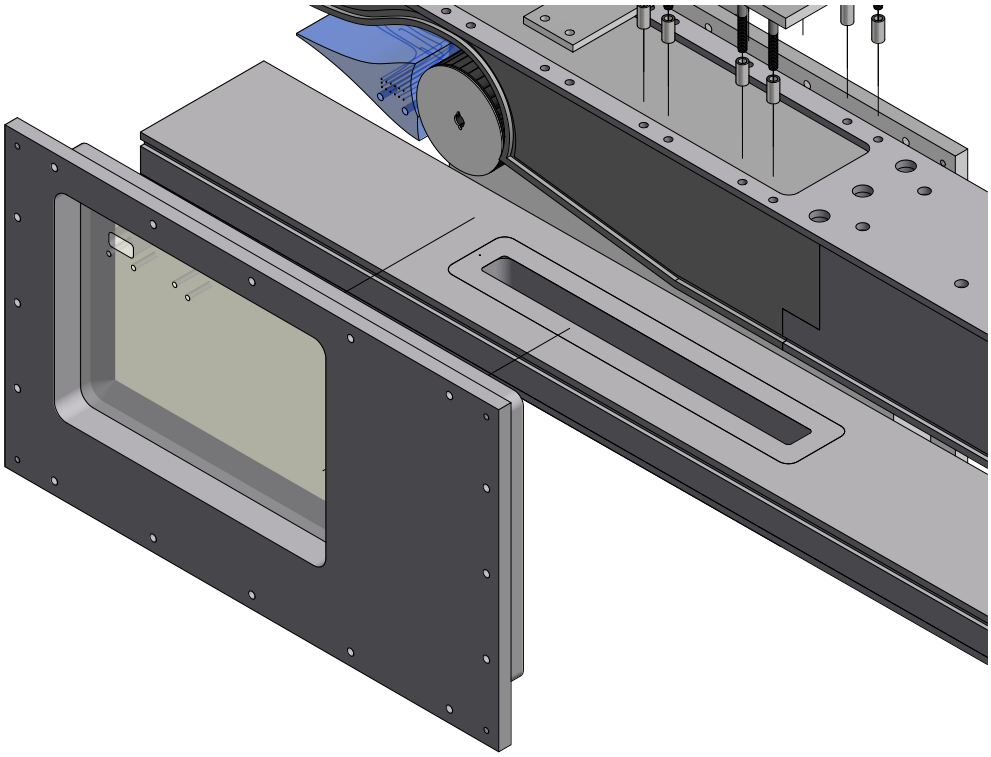

Figure 2.2: A rendering of the tunnel window setup.

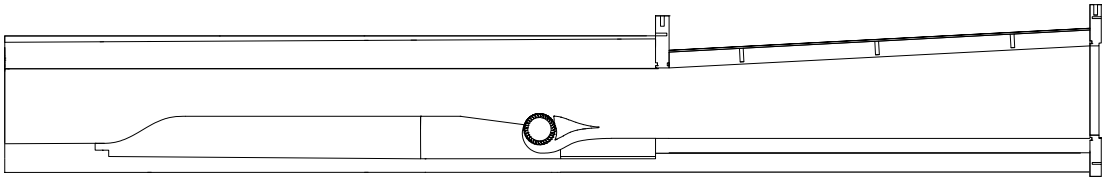

Figure 2.3: Wind tunnel cross sectional diagram.

2.1.3 Fan and Housing Design

2.1.3.1 Fan Design

An image of the fan selected for this study is shown in Figure 2.4. Several off-the-shelf cross-flow fans were purchased and considered for the study, and the chosen fan was extracted from a Lasko 42” Wind Curve model 2551 tower fan. The fan was composed of a hard plastic material and had 32 blades which were reinforced in the middle by a structural ring. The outer diameter of the fan was 3.42”, and the inner diameter was 2.4 ”. The fan was cut to fit the 5” width of the test section, and aluminum end caps were attached to the ends of the fan to provide structural reinforcement. An

8mm stainless steel shaft was force fit into each of the end caps to connect the fan to bearings embedded within each of the tunnel walls. The fan is shown with the end caps before they were attached in Figure 2.4(b).

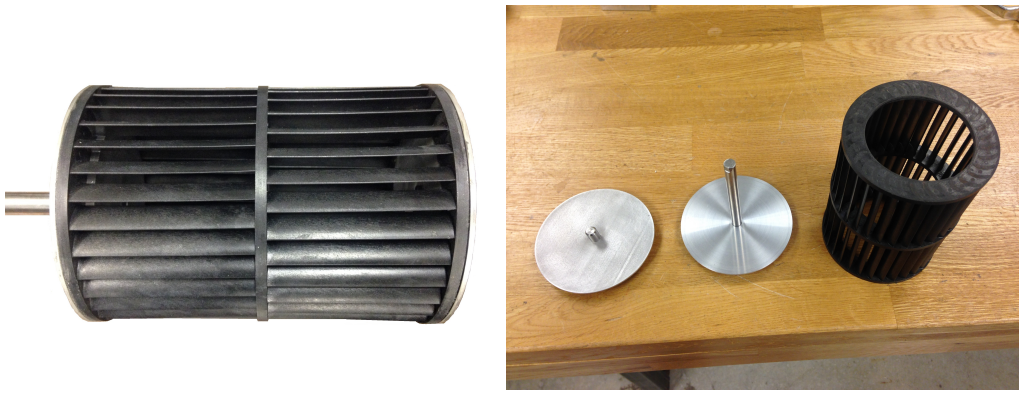

(a) (b)

Figure 2.4: The cross-flow fan which was investigated in this study, (a) assembled and (b) disassembled.

In order to reduce the vibrations which could occur when spinning the fan at high rotational rates, a simple procedure was used to enhance the balance of the fan. The two shafts of the fan were balanced on the two perfectly level grips of a CNC mill located in ARL so that the fan was free to rotate on its shafts. The fan was then perturbed from rest so that any imbalances could be noted as it rolled across the clamp. Small pieces of electrical tape were adhered to the fan blades in order to correct for any noted imbalances. This procedure was performed until the fan could be rolled from any angular starting position without visibly noticeable imbalances.

2.1.3.2 Initial Housing Design

The initial fan which was selected for the study was an aluminum fan with 22 blades and an outer diameter of 1.2". This fan was chosen for its small diameter which allowed the fan to be embedded several inches within the tunnel wall. A diagram of this fan in its housing embedded in the tunnel wall is shown in Figure 2.5. Freestream flow is from left to right, and the fan as it is shown rotates counter-clockwise. The inlet duct was designed to draw flow in at an angle of 60° with respect to the freestream flow, and the outlet duct was designed to exhaust tangent to the freestream flow. Also visible in the diagram are the two probe access holes which allowed for measurements of the flow properties to be taken in the inlet and outlet ducts of the fan. These properties could be used to compute fan efficiency parameters, as well as to extract the amount of work which was performed on the fluid passing through the duct by the fan.

The expansion surface piece, also referenced in Figure 2.5, was manufactured using stereolithography (SLA) from a polymer resin. Brass heat-set inserts with 8-32 threading were inserted into built-in holes in the sides of the expansion surface to allow for mounting to the new tunnel windows. From Figure 2.5, it can be seen that the expansion surface is used to define several important parameters for the fan housing design. In addition to forming the vortex wall for

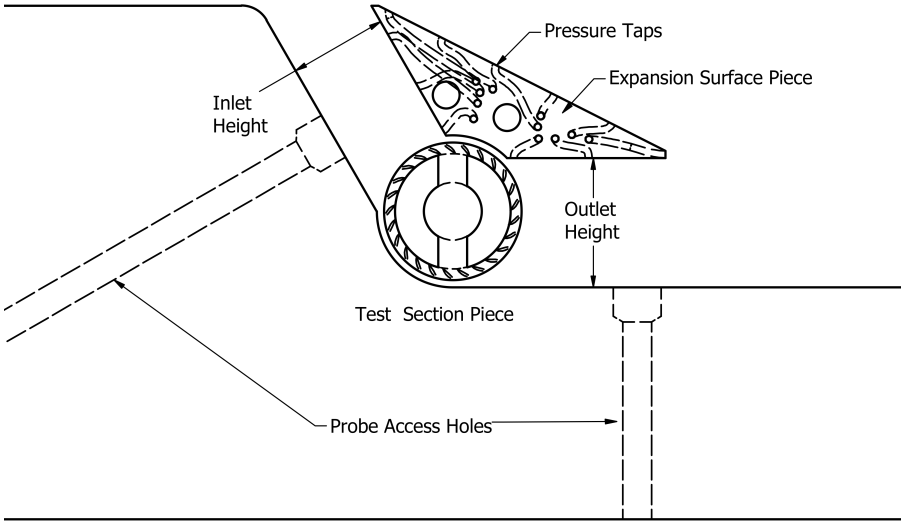

Figure 2.5: Original fan housing design.

Table 2.1: Initial Inlet and Outlet Heights

$ES\#$	h_1/D [in]	h_2/D [in]
1	0.4	0.93
2	0.4	0.7
3	0.6	0.3

the fan, the expansion surface design also defined the heights of the inlet and outlet ducts for the fan. The expansion surface also served to simulate a simple geometry of the trailing-edge region of an airfoil section. For the initial expansion surface pieces, this upper surface was simply a flat slope. A total of ten pressure taps were located around the expansion surface. Three of the taps were located in the inlet duct, two in the outlet duct, and the remainder located on the upper surface exposed to the freestream flow. These taps were included in the expansion surface to investigate whether or not the embedded cross-flow fan could provide enough suction to promote attached flow over the representative trailing edge region of an airfoil in transonic flow.

Due to the relative ease of manufacturing SLA parts, several expansion surface pieces were made with a variety of inlet and outlet duct heights. These quantities are given in Table 2.1 for each of the expansion surfaces which were designed for the initial fan and housing, where h_1 is the inlet height, h_2 is the outlet height, D is the fan diameter, and $ES\#$ is the expansion surface number. The purpose of varying these geometric parameters was to easily converge upon a fan housing design which gave the desired suction performance.

The initial test results (discussed briefly in Chapter 3) indicated very poor performance from the fan due to several ineffective housing design factors. First, it became evident that the fan diameter was far too small for such an application, since the required rpm to achieve the desired suction was completely unattainable. For this reason, the

final fan with a diameter of 3.42” was chosen to reduce the rpm requirement. Second, based on conclusions from the previously discussed literature, it was realized that the fan will perform most effectively when the flow approaches the first stage radially, and the exit duct must curve and leave room below the fan to allow the flow to exit tangentially. With these considerations in mind, a new fan and housing were designed.

2.1.3.3 Final Housing Design

A detailed image of the fan and its final housing in the tunnel is shown below in Figure 2.6. Due to the larger diameter of the final cross-flow fan as well as the requirement that flow should be able to enter the fan radially, the new housing was designed to allow a large arc of the fan to be exposed to the freestream flow on the inlet side. As a result, the the final housing was equipped with an outlet duct but no inlet duct. A diffusing ramp of 7.5° was also incorporated into the tunnel wall leading up to the fan inlet arc to allow flow to enter the fan radially over the upstream region of the fan. The angle of 7.5° was chosen as the recommended angle to promote attached flow in an inlet expansion by Farokhi [25]. The fan rear-wall housing was also built into the aluminum test section, leaving room under the fan to allow the flow to exit tangent to the blades. The gap between the fan outer diameter and the housing walls was chosen to be 0.125” in order to keep the gap below 5% of the fan diameter as suggested for proper performance [17]. As indicated by the red arrow, the fan rotates counter-clockwise in this configuration with the flow moving from left to right. As before, the test-section piece was machined out of 6061 aluminum. The black line which is offset 0.25” from the edge (visible in the photo) is an O-ring which was used to create a seal when the tunnel wall was installed. Also visible in the image are the pressure tubes connected to the side of the expansion surface.

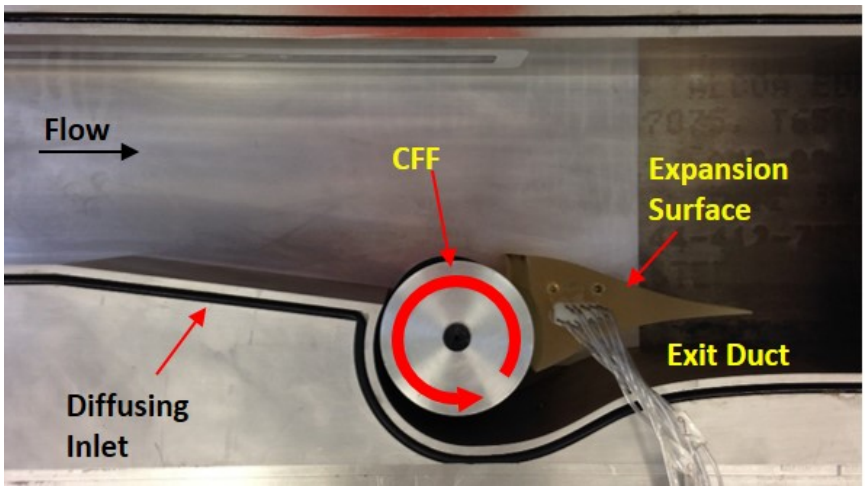

Figure 2.6: Cross-flow fan housing and tunnel setup.

The design of the expansion surface was also modified in several regards. The upper surface was contoured to simulate the trailing edge of the transonic Griffith/Goldschmied airfoil which has been discussed in Section 2.2. The arc of the expansion surface which is closest to the fan functioned as the vortex wall for the fan. Above the vortex wall, a small cusp was extended upwards to bring the top of the expansion surface level with the test section floor as well as to promote the radial entry of flow into the fan. The expansion surface was also equipped with 13 pressure taps distributed evenly across the upper and lower (inside the duct) surfaces to measure the pressure distributions over the surface as before. The lower surface of the expansion surface was shaped to match the contour of the rear wall, forming a constant-area exit duct. A diagram showing the location of the pressure taps is shown in Figure 2.7. A probe access hole was also located directly downstream of the fan in the exit duct to allow for surveys of total pressure, total temperature, and velocity across the exit duct. The expansion surface piece was again manufactured using SLA, and brass heat-set inserts were used to mount the piece to the tunnel walls. An image of the expansion surface piece with steel tubes inserted into the pressure tap exit holes on the side of the piece for easy connection to the polyurethane tubes is shown in Figure 2.8.

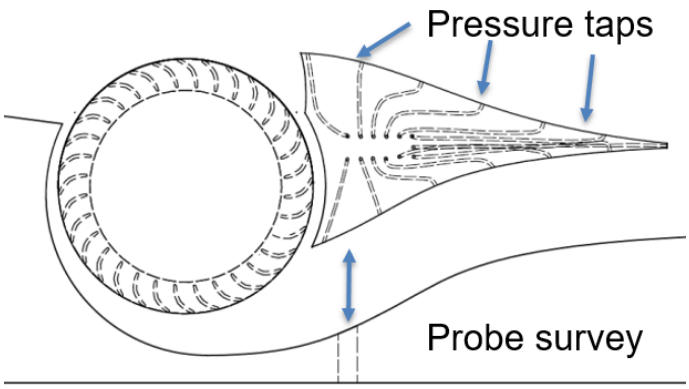

Figure 2.7: Location of pressure taps and probe access hole.

2.1.4 Fan Power Drive

The components which were incorporated into powering the cross-flow fan are discussed in this section. These include the motor, motor drive, all of the mechanical couplings, and a torque transducer which was used to measure the shaft power of the fan system. An image of the fan power drive system from the outside of the tunnel is shown in Figure 2.9.

Figure 2.8: The expansion surface piece with tap inserts.

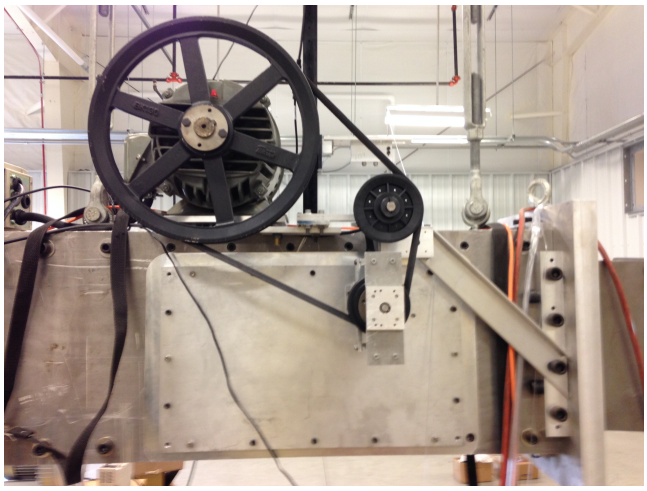

Figure 2.9: The cross-flow fan power drive system.

The shaft on one side of the fan passed through the tunnel back window and was connected to the fan power drive shaft with a zero-backlash flexible shaft coupling. The shaft coupling was 1.4” long and was composed of two sections joined by a rubber center piece. Each section was attached to its respective shaft by tightening the coupling with a screw. An image of the shaft coupling used is shown in Figure 2.10(a).

The first component of the fan power drive was an Interface Force T4 rotary torque transducer which provided direct measurements of shaft torque and rpm. The torque transducer shaft was free-rotating and did not interfere with the power transmission from the motor to the fan. both the driver and driven shaft of the torque transducer were 8 mm in diameter. On the driver side, another zero-backlash shaft coupling connected the torque transducer to a transition shaft which had an 8mm diameter on one end and an 0.5” diameter on the other end for attachment to the driven

pulley. A photo of the torque transducer is given in Figure 2.10(b). An image of the cross-flow fan connected to the torque transducer with the shaft coupling is shown in Figure 2.11. Also shown in the figure is the custom aluminum mounting block which was used to hold the torque transducer in place, as well as the transition shaft which interfaced with the pulley system.

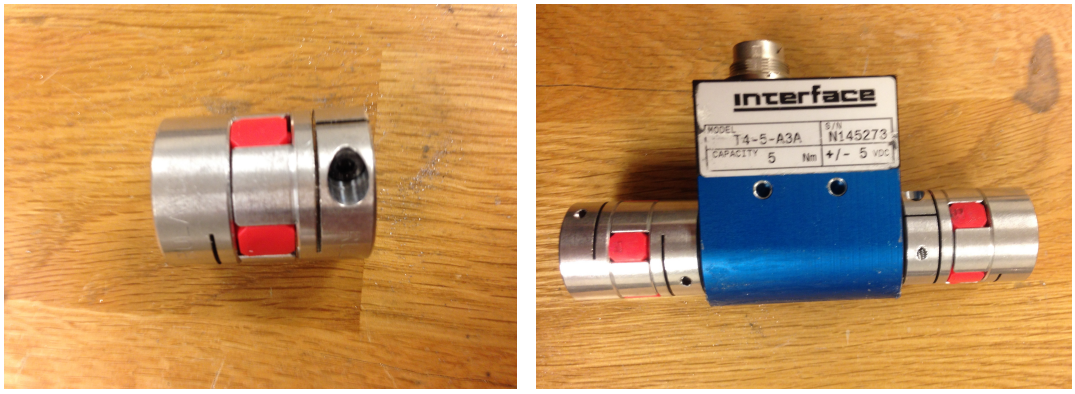

(a) (b)

Figure 2.10: (a) Zero-backlash flexible shaft coupling and (b) T4 rotary torque transducer.

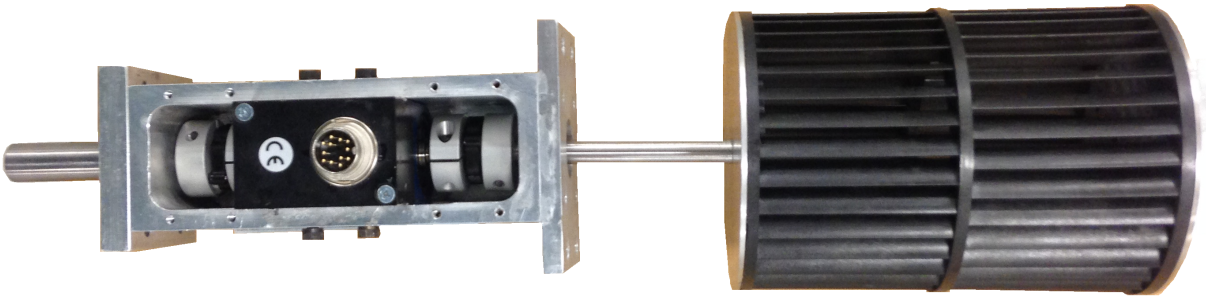

Figure 2.11: An image of the cross-flow fan connected to the torque transducer.

The next component of the power drive system was a V-belt pulley system which was used to increase the rpm of the driving motor by a factor of 3.6. The driver pulley had a diameter of 12.75” and was attached to the 1.125” in diameter motor shaft with an H-style split-tapered bushing. The driven pulley was 3.55” in diameter and was attached to the 0.5” end of the transition shaft with an H-style split-tapered bushing. An additional bracket was mounted onto the tunnel to support the driven pulley from the outside to eliminate any wobbling due to the tension of the V-belt. The idler pulley was 4” in diameter and was fastened to an 0.5” in diameter hardened precision steel shaft with two clamp on shaft collars. An additional support bracket was also attached to the idler pulley shaft support which attached the pulley support to the tunnel wall. The support brackets were added to ensure that the driver, driven, and idler pulleys

were all aptly supported to minimize vibrations and loss of power through the belt drive. A 53" A-section V-belt was used to transmit the power from the motor pulley to the driven pulley.

The motor which drove the system was a 5 hp 208V 3-Phase AC motor which was manufactured by U.S. Electrical Motors, and was mounted to the top of the wind tunnel. In order for the motor to be mounted to the wind tunnel, a custom adapter plate was manufactured. The plate was 0.325" thick and was machined out of 6061 aluminum. The plate had eight countersunk holes to allow it to interface with the $\frac{1}{4} - 20$ threads on the top of the tunnel. Each of these holes was aligned with a $\frac{3}{4}$" steel spacer to raise the mounting plate off of the wind tunnel outer surface. The motor interfaced with the plate through four $\frac{1}{2}$" slots allowing the placement of the motor to be varied. An image of the adapter plate is shown in Figure 2.12. The speed of the motor was controlled by a Saftronics model C102005-1 5hp 230V variable frequency drive. The maximum speed of the motor was about 5000 rpm, leading to a maximum fan speed of about 15,000 rpm. Due to the limitations of the VFD, however, the maximum attainable rpm was 8000. The only input to the VFD was the desired electrical frequency, so it was necessary to utilize an external measurement to determine the fan rpm. The torque transducer provided this required rpm measurement, which was monitored in LabVIEW during testing. The electrical frequency required for a desired rpm was thus iteratively obtained. A rendering of the motor, pulley system, and torque transducer attached to the wind tunnel is shown in Figure 2.13.

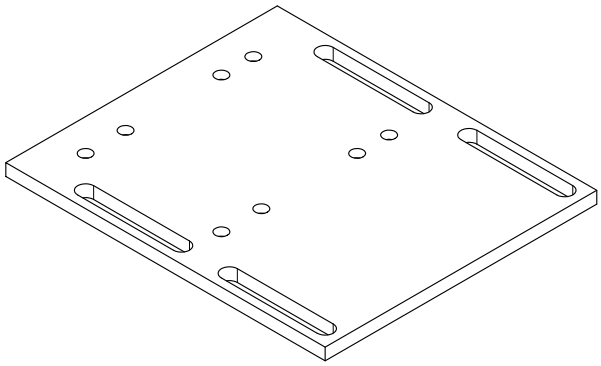

Figure 2.12: A rendering of the motor adapter plate.

The VFD output voltage was proportional to the driving frequency, as determined by a three part piece-wise linear curve. The default frequency vs. voltage curve which was programmed into the VFD did not supply adequate power to run the cross-flow fan in transonic flow, so it was necessary to make modifications. The final frequency vs. voltage curve which was programmed into the VFD during the experiment is shown in Figure 2.14. Most of the tests were run

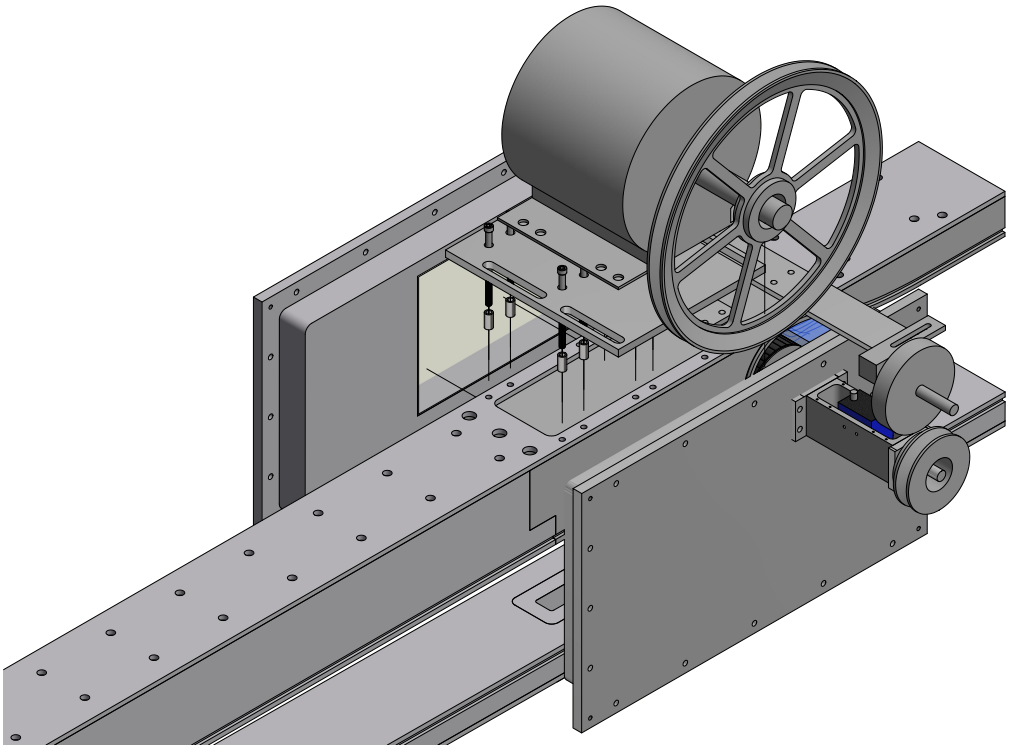

Figure 2.13: A rendering of the motor and tunnel setup.

in the 20 Hz to 40 Hz range, so it was important to ensure that the VFD would supply adequate voltages within this range.

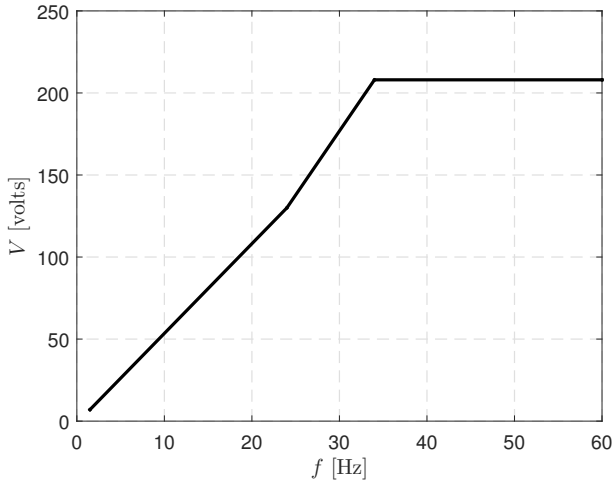

Figure 2.14: The voltage vs. frequency curve for the VFD.

2.1.5 Data Acquisition

All tunnel operation and data acquisition for the transonic testing of the cross-flow fan was performed using an ASUS Cooler Master computer with an AMD Phenom II X4 782 MHz processor and 3.25 GB of RAM. The computer was run with a Windows XP 32-bit operating system. A program had previously been developed using National Instruments LabVIEW to simultaneously control the stagnation pressure of the wind tunnel and acquire the data of interest. The primary data acquisition interface was a National Instruments NI cDAQ-9174 CompactDAQ chassis. This is a four-slot chassis which was connected to the data acquisition computer through USB. The chassis was equipped with a National Instruments NI 9201 8-channel analog input module, as well as a National Instruments 9265 4-channel current output module. The current output module was used to send a current to control the position of the gate valve, which was used to set the tunnel stagnation pressure. Analog signals from the tank, static, and stagnation pressure transducers, the stagnation thermocouple, the hotwire anemometer, and torque transducer were all acquired with the 8-channel analog input module, at a sampling rate of 2 kHz. The tank, static, and stagnation pressure as well as stagnation temperature were additionally displayed on the control panel which is shown in Figure 2.15. The pressure readings were shown on Precision Digital display units, and the temperature reading was shown on an Omega thermocouple display unit. Additional thermocouple measurements in the outlet duct were interfaced with the computer through a National Instruments USB-TCO1 thermocouple measurement device. A National Instruments USB-6009 low-cost multifunction DAQ with 12 digital I/O channels was also connected to the computer to record the pulse train signal generated by the torque transducer for rpm measurements.

Figure 2.15: The wind tunnel control panel.

2.1.6 Pressure Measurements

Pressure measurements for the transonic cross-flow fan testing can be divided into three categories. As previously mentioned, static and total pressure measurements were taken to characterize the tunnel conditions. Measurements of static pressure from the taps located on the expansion surface piece were also taken. Finally, total pressure measurements across the outlet duct were recorded. The equipment and methods which were used to acquire each of these pressure measurements are discussed in this section.

2.1.6.1 Surface Pressures and C_p Distributions

As discussed in Section 2.1.3, the expansion surface was equipped with pressure taps on both the upper surface exposed to the freestream flow and within the exit duct of the fan. Each of the pressure taps was connected to a polyurethane tube which passed through the tunnel side window. These pressure tubes were routed to a Model 98RK Pressure Systems Inc. Net Scanner electronically-scanned pressure system which was connected to the data acquisition computer through an Ethernet connection. The NetScanner rack chassis was equipped with 8 pressure modules, each of which had 16 pressure ports. Module number 5 had a pressure range of $\pm$15 psi and was used to measure all of the expansion surface pressures in this study.

All pressures measured by the NetScanner were referenced to the local ambient pressure. Since the transonic wind tunnel was pressurized, the total pressure in the tunnel was different than the ambient pressure of the laboratory. It was therefore necessary to take a supplemental measurement of the ambient pressure using a Pressure Systems NetScanner model 9034. The NetScanner 8RK module 5 was zeroed before each sequence of runs. This process required a supply of compressed nitrogen at a pressure of 100 psi which was used to move a manifold within the NetScanner chassis to allow the module to be zeroed.

Due to the compressible nature of the flow in the transonic wind tunnel, the incompressible Bernoulli's equation could not be used in conjunction with the tunnel static and stagnation pressures to compute the freestream dynamic pressure defined by Eq. 2.24. The compressible Bernoulli equation, given by Eq. 2.3, was instead used to relate the dynamic pressure to the measured test-section static pressure and stagnation pressure. Flow in the tunnel was assumed to be isentropic so that the tunnel stagnation pressure was the same as the test-section total pressure. The stagnation density, ρ_o, could be calculated according to the ideal gas law based on the measurements of the total temperature, T_o, and the total pressure, P_o, as shown by Eq. 2.4 where R is the specific gas constant for air. The freestream density could then be calculated according to the isentropic relation given in Eq. 2.5 where M is the Mach number. Combining

these equations, the dynamic pressure could then be calculated by Eq. 2.6.

$$\frac{V_\infty^2}{2} + \left(\frac{\gamma}{\gamma-1}\right)\frac{P_\infty}{\rho_\infty} = \left(\frac{\gamma}{\gamma-1}\right)\frac{P_o}{\rho_o} \tag{2.3}$$

$$\rho_o = \frac{P_o}{RT_o} \tag{2.4}$$

$$\rho_\infty = \rho_o\left(1+\frac{\gamma-1}{2}M^2\right)^{\frac{-1}{\gamma-1}} \tag{2.5}$$

$$q_\infty = \left(\frac{\gamma}{\gamma-1}\right)P_o\left(1+\frac{\gamma-1}{2}M^2\right)^{\frac{-1}{\gamma-1}} - \left(\frac{\gamma}{\gamma-1}\right)P_\infty \tag{2.6}$$

The pressure coefficient, C_p, for any of the pressure taps could then be calculated based on the dynamic pressure. The conventional definition of the pressure coefficient is given by

$$C_p = \frac{P-P_\infty}{q_\infty}, \tag{2.7}$$

where P is the pressure measured local to the expansion surface by the pressure tap. Since the surface pressures were measured relative to the ambient pressure in the laboratory environment, it was necessary to add the recorded atmospheric pressure to the measured values to ensure that the absolute value of the local pressure was utilized. The test-section static pressure, P_∞, was measured using an absolute pressure transducer, so no additional calculation was necessary before the computation of the pressure coefficient.

2.1.6.2 Total Pressure Measurements

In order to survey the total pressure, total temperature, and velocity within the outlet duct, a Zaber T-LSR300A motorized linear slide was installed onto the wind tunnel in alignment with the probe access hole, shown previously in Figure 2.7. The Zaber traverse was controlled with a routine in LabVIEW which accurately placed the probe in desired survey locations across the exit duct. Signals were sent to the traverse through USB communication. The locations which were chosen to be surveyed began 0.05" from the SLA piece in the duct, and decreased in increments of 0.05" until the floor of the duct was reached. A rendering of the traverse mounted to the wind tunnel is shown in Figure 2.16.

For measurement of the total pressure within the duct, a custom made total pressure probe was mounted to the traverse and connected to an additional port in module 5 of the NetScanner pressure system using 0.063" tubulation polyurethane tubing. An image of the total pressure probe is shown in Figure 2.17. The probe consisted of an outer support tube which was 0.125" in diameter and made of standard steel. The functional portion of the probe consisted

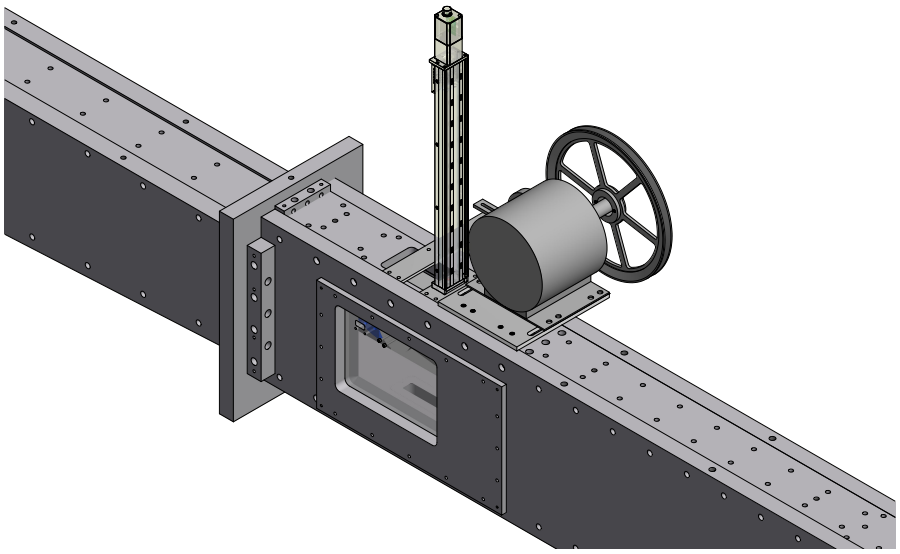

Figure 2.16: A rendering of the Zaber mounted on the wind tunnel.

of an annealed steel tube which was 0.05” in diameter. This tube was bent 90° to be aligned with the flow in the duct. Since the total pressure was also measured with the NetScanner, it was necessary as before to add the measured atmospheric pressure to obtain the total pressure at each survey location.

Figure 2.17: The total pressure probe which was used.

2.1.7 Hotwire Measurements

To take velocity measurements in the outlet duct, a TSI model 1201 hotwire probe was used. The probe was inserted into a TSI two-sensor probe support which was attached to the Zaber traverse. The probe support was wired to a TSI Incorporated IFA 100 System Intelligent Flow Analyzer with a BNC cable. The voltage of the hotwire as determined by the flow analyzer was then sent to the data acquisition system as an analog signal, as previously discussed. Measurements of velocity were taken at the same points in the duct as for the total pressure survey. An image of the probe support is shown in Figure 2.18.

2.1.7.1 Hotwire Configuration and Calibration

The standard procedures which are outlined in the IFA 100 manual were executed to configure the hotwire probes for use. First, a shunt probe was inserted into the probe support and the resistance of the anemometer circuit was

Figure 2.18: The TSI probe support which was used.

zeroed. The change in resistance which was required to zero the display with the shunt probe in place was recorded as the cable resistance. The hotwire probe cold resistance was then measured by removing the shunt and inserting the probe into the probe support and measuring the cable-subtracted resistance with the anemometer in standby mode. The operating resistance of the probe was then set by turning the resistance knob while the operating resistance setting was selected. The operating resistance of the probe was chosen to be the resistance recommended by the manufacturer for each probe serial number. The operating resistance of the probe (serial # 17-17) which was used to measure the velocity in the duct was 9.48 Ω. The bridge compensation was set to 115 as suggested by the manual by turning the bridge compensation knob. Finally, a waveform generator was attached to the anemometer to generate a square wave, and an oscilloscope was attached to the output. The frequency compensation knob was tuned to ensure that the frequency response of the hotwire probe was within an acceptable range.

In order to calibrate the hotwire probe, it was necessary to expose the probe to the freestream flow in the tunnel test section. This was accomplished by drilling a 0.25" in diameter hole in the front tunnel window which would allow the probe support to be passed through and the probe to be positioned in the center of the tunnel. $\frac{1}{4}-20$ threads were added to the hole to allow for sealing during normal tunnel operation. In order to calibrate the probe in the blowdown tunnel, it was necessary to first shut the manual valve upstream of the automatic gate valve which controlled the tunnel pressure. With the manual valve shut, the gate valve was open to about 80% capacity. The manual valve was then opened by small increments with the data acquisition system running in order to record the tunnel conditions and hotwire probe voltage for each of the manual valve positions. Under the same assumptions as mentioned in Section 2.1.6.1, the flow velocity could be calculated according to Eq. 2.8 for each of the valve positions and correlated to the recorded hotwire voltages.

$$V_\infty = \sqrt{2\left(\frac{\gamma}{\gamma-1}\right)\left(\frac{P_o}{\rho_o}-\frac{P_\infty}{\rho_\infty}\right)} \tag{2.8}$$

The acquired calibration voltages were corrected to the total temperature of the tunnel at zero velocity using the temperature correction method discussed in Section 2.1.7.2. This correction was necessary as the total temperature in

the tunnel changed as the tunnel speed was increased. A fourth order polynomial was fit to the voltage vs. velocity data in order to produce the calibration curve given by Eq. 2.9. An image of the probe support set up in the calibration position is shown in Figure 2.19, and an example of the calibration curve for the hotwire probe is shown in Figure 2.20.

$$v = C_0 + C_1 V + C_2 V^2 + C_3 V^3 + C_4 * V^4 \tag{2.9}$$

Where v is the velocity, V is the measured voltage, and the values of the calibration coefficients $C_0 - C_4$ for probe #17-17 are given in Table 2.2.

Table 2.2: Calibration Coefficients

C_0	C_1	C_2	C_3	C_4
6006.110719	-9702.420538	5874.374585	-1576.774882	160.679353

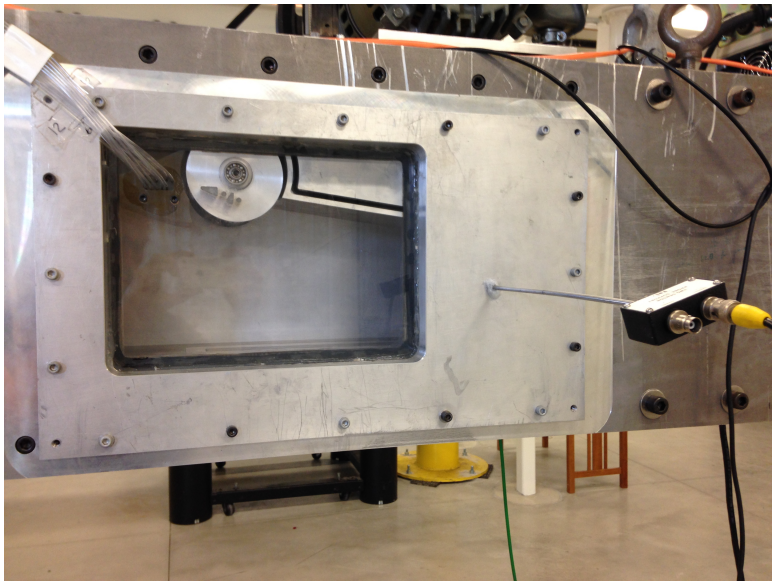

Figure 2.19: Probe support installed in tunnel window for calibration.

2.1.7.2 Hotwire Temperature Correction

The resistance of a hotwire probe as well as the voltage necessary to produce a constant probe temperature will vary with changing temperature of the surrounding fluid. As a result, it was necessary to use standard correction methods to adjust the measured hotwire voltages due to changes in temperature during testing. In standard low-speed use of a hotwire probe, the total temperature of the flow is usually assumed to be constant, and voltage measurements are corrected for the difference in temperature between the test conditions and the calibration conditions. During transonic testing in a blow-down tunnel, however, the stagnation temperature would change during the course of a single tunnel

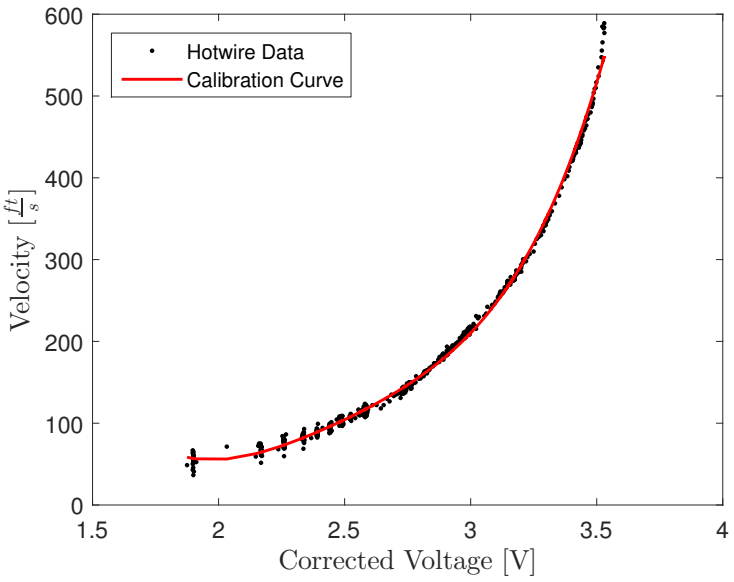

Figure 2.20: Probe 17-17 calibration curve.

run. it was thus necessary to correct each data point to the original tunnel-off stagnation temperature data point during calibration. As previously mentioned, this correction was performed for the voltages measured during the calibration as well, in order to avoid the necessity of a look-up table for voltage and temperature.

The measured hotwire voltages were corrected using the methods of Tropea et. al. [26] accoring to Eq. 2.10, where T_{oper} is the hotwire operating temperature, T_{ref} is the tunnel stagnation temperature during the first calibration point, and T_o is the stagnation temperature corresponding to the measured voltage.

$$V_{cor} = V\sqrt{\frac{T_{oper} - T_{ref}}{T_{oper} - T_o}} \tag{2.10}$$

The operating temperature can be calculated according to Eq. 2.11 which was given in the IFA 100 manual. Here, R_{op} is the operating resistance, R_0 is the probe resistance at 0° C, and R_{100} is the probe resistance at 100° C. The values of each of these resistances were taken from the manufacturer specifications for each probe.

$$T_{oper} = (R_{op} - R_0)\left(\frac{100}{R_{100} - R_0}\right) \tag{2.11}$$

2.1.8 Thermocouple Measurements

During acquisition of the duct total temperatures, an Omega TJ36, J-type thermocouple was mounted to the traverse and routed to a National Instruments USB-TC01 Thermocouple measurement device using J-type thermocouple wire.

Again, the duct survey measurements were set to the same locations as those of the total pressure surveys. An image of the thermocouple used in this study is show in Figure 2.21.

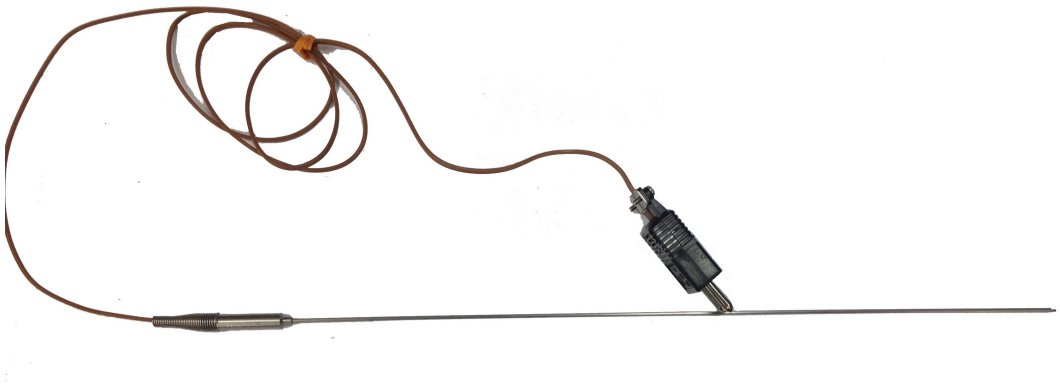

Figure 2.21: Omega TJ36 thermocouple probe.

2.1.9 Torque and RPM Measurements

An Interface Force T4 rotary torque transducer was used to directly measure the cross-flow fan shaft torque and rpm while in operation. The transducer utilized a non-contact measurement technique, which prevented interference of the shaft rotation during operation. The range of the torque transducer was ± 5 Nm. The torque transducer sent an analog ± 5 V signal corresponding to the measured torque, with a maximum error of $\pm 0.2\%$ of the full range of operation. This analog signal was acquired using the main data acquisition board along with the other analog measurements previously mentioned. The transducer also output a TTL pulse signal, each pulse of which corresponded to one revolution of the shaft. This TTL signal allowed for a direct reading of the fan rpm which was acquired using the 32-bit counter channel available on the NI USB-6009 data acquisition board.

The LabVIEW routine which acquired the TTL signal was incorporated in such a way that the measurement was sensitive to the number of samples taken. If the number of samples was not high enough, the number of pulses measured with each call to the LabVIEW VI varied in a significant enough manner to affect the measured rpm. This issue was addressed by recording the measured rpm over a series of calls to the VI for several different sample sizes. The standard deviation in rpm measurement was calculated for each of the different sample sizes. The results of this exercise are shown in Figure 2.22. As the number of samples increased, the time to record the samples also increased, so a trade-off was necessary. The final sample size which was chosen was 1000.

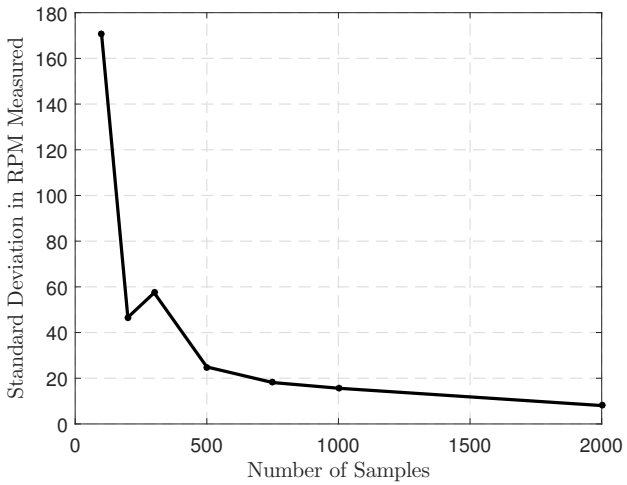

Figure 2.22: Sample size dependency of rpm measurements.

Measurement of the cross-flow fan rpm and torque allowed for a direct computation of the power consumed by the fan, denoted W_s. The power in kW was computed as follows:

$$W_s = 2\pi\tau\frac{rpm}{60}, \tag{2.12}$$

where τ is the measured torque in Nm.

2.1.10 Calculation of Mass Flow

Measurements of the total temperature, total pressure, and velocity in the outlet duct were utilized to calculate the mass flow rate of air through the duct. First, it was necessary to compute an average value for each of these properties in the duct using a trapezoidal integration method. Breaking the distance across the duct into discrete segments, the integral of the property f across the duct is given by:

$$F = \int_0^L f\,dy = \frac{l}{2}\sum_{k=1}^{N}(f_{k+1} + f_k) \tag{2.13}$$

where F is the value of the integral, N is equal to the number of discrete segments, L is the total distance across the duct, and l is the length of each discrete segment. The average value of the flow property across the duct can then be computed by:

$$f_{average} = \frac{F}{L} \tag{2.14}$$

Since none of the other properties were known in the duct, it was necessary to make several assumptions to compute the mass flow. Since there were pressure taps located inside the duct, it was assumed that that static pressure across the duct was equal to the value of the static pressure measured by the nearest pressure tap inside the duct. Second, it was assumed that the flow across the duct was isentropic, allowing for calculation of a Mach number. The Mach number was calculated according to Eq. 2.15, where P is now the static pressure from the pressure tap, and P_o is the average total pressure in the duct.

$$M = \sqrt{\frac{2}{\gamma - 1}\left[\left(\frac{P_o}{P}\right)^{\frac{\gamma-1}{\gamma}} - 1\right]} \tag{2.15}$$

The total density of the duct was calculated according to the ideal gas law, and then the static density was calculated from the isentropic relation using the computed duct Mach number in Equation 2.5. This then allowed for a direct calculation of the duct mass flow rate from Eq. 2.16.

$$\dot{m} = \rho V A \tag{2.16}$$

where A is the cross-sectional area of the duct at the survey location. The velocity of the flow at the inlet to the fan was also computed since no direct measurement could be made. This computation was performed by taking the mass flow rate calculated from the exit duct properties and dividing it by the freestream density and the area of the inlet arc.

2.1.11 Scaling of Test Data

In order to scale the experimental data to determine the power required to run a cross-flow fan that spanned the length of an actual aircraft wing, it was necessary to use several non-dimensional parameters. The first of these parameters was the flow coefficient, ϕ, defined as:

$$\phi = \frac{V_\infty}{\omega D_o} \tag{2.17}$$

where ω is the angular velocity of the fan, and D_o is the diameter of the fan. This coefficient represents the ratio of the freestream velocity to twice the fan tip speed. Previous work by Dygert and Dang [15] suggests that this parameter can be used to dynamically scale fan data between two different flight conditions. The aircraft fan tip speed which would be required to produce the same amount of suction/blowing as the experiment was then computed by matching flow coefficients between the two cases and solving for $U_{o,ac}$, the aircraft fan tip speed.

The second non-dimensional parameter was the power coefficient, λ, defined by Dang [16] as:

$$\lambda = \frac{W_s}{\frac{1}{2}\rho D_o U_o^3 b} \tag{2.18}$$

where W_s is the fan shaft work, ρ is the freestream density, D_o is the fan diameter, U_o is the fan tip speed, and b is the span of the fan. Data from the wind tunnel tests were used to compute this power coefficient at a Mach number of 0.7.

It was then assumed that when implementing the cross-flow fan on the SUGAR Refined aircraft the power coefficient would remain constant across the portion of the span containing the cross-flow fan. For a first estimate of the power required by the CFF wing, a constant tip speed was also assumed, although this assumption would be difficult to realize on a physical aircraft due to the change in diameter of the cross-flow fan across the wing span. However, a representative constant tip speed could be approximated by breaking the fan up into several span-wise sections which each ran at the same tip speed. Therefore, this assumption holds for a first estimate of the power required by the cross-flow fan system. Using the power coefficient calculated from the experimental data in conjunction with the flight conditions and SUGAR Refined wing geometry, an estimate of the total power required to run cross-flow fans in both wings was calculated according to the following integral:

$$P = 2\int_0^{b/2} \frac{W_s}{b} dy \tag{2.19}$$

where

$$\frac{W_s}{b} = \frac{1}{2}\rho D_o U_o^3 b \tag{2.20}$$

and b is the length of the portion of the span covered by the cross-flow fan.

2.2 Low Speed Wind Tunnel Testing

A low-speed wind tunnel test was performed on the designed Griffith/Goldschmied airfoil with suction and blowing. Although the airfoil was designed for Mach 0.7 flow, the low-speed test was performed in order to validate the CFD design methods which were utilized. This section describes the wind tunnel facility, the design of the test setup, and the data acquisition equipment and data reduction methods which were used during the low-speed testing of the airfoil model.

2.2.1 Wind Tunnel Facility

All of the low-speed tests of the airfoil model were performed in the subsonic, low-turbulence, open-return wind tunnel located in the Aerodynamics Research Laboratory (ARL). The tunnel had a rectangular test section measuring 2.8' $\times$ 4'. The test section was designed such that the downstream end of the test section was 0.5" wider than the upstream end to account for growth of the tunnel wall boundary layer. The inlet portion of the wind tunnel was comprised of a nozzle with an area contraction ratio of 7.5:1, and a series of honeycomb flow straighteners and flow conditioning

screens. The wind tunnel diffuser transitioned from a rectangular cross at the test section to a circular cross section near the tunnel exhaust where the fan was located. A diagram of the wind tunnel is shown in Figure 2.23.

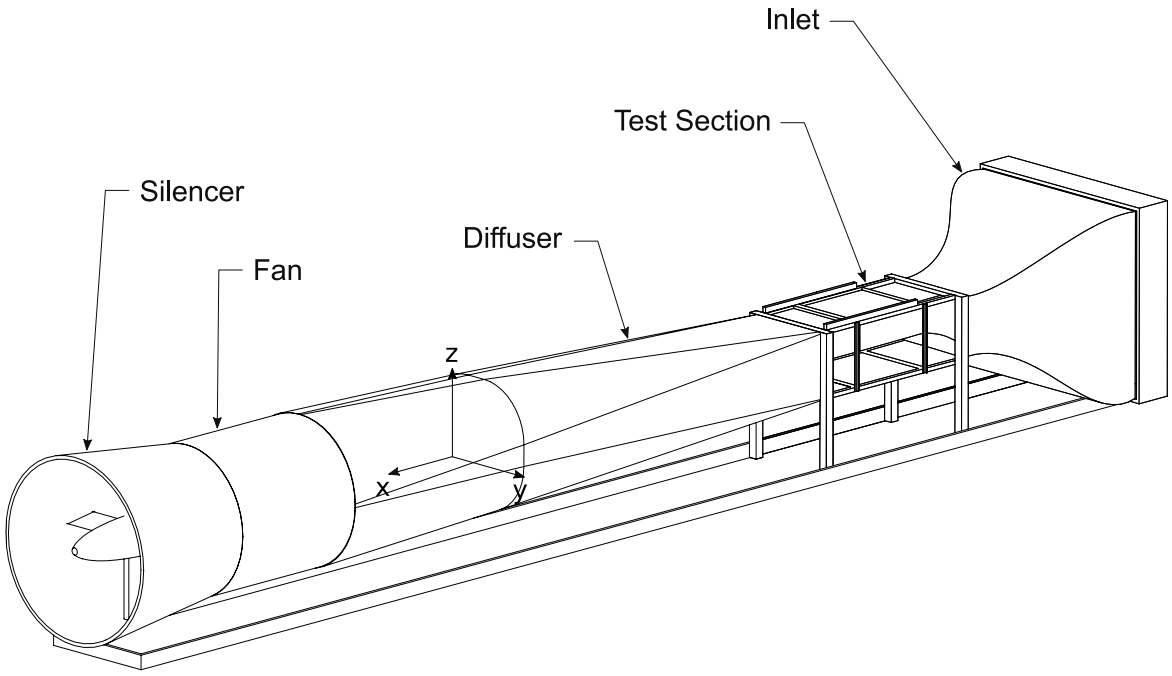

Figure 2.23: The low-speed wind tunnel located in ARL.

The wind tunnel fan was powered by a 125 hp AC motor driven by an ABB ACS 800 Low Voltage AC Drive. The fan was capable of producing a maximum flow speed of 242 ft/s which corresponded to a maximum fan rpm of approximately 1200. This setting provided a maximum chord-based Reynolds number of 1.5×10^6 /ft, where the Reynolds number was calculated according to Eq. 2.21. In this equation, Re is the Reynolds number, ρ is the air density, V_∞ is the velocity of the freestream flow, c is the airfoil chord length, and μ is the dynamic viscosity of air.

$$Re = \frac{\rho V_\infty c}{\mu} \tag{2.21}$$

During operation, a proportional controller was used to control the wind tunnel Reynolds number to within 0.5% of the desired value. After each airfoil angle of attack which was tested, the Reynolds number was checked and adjusted to ensure that it remained at the desired value.

Calculation of the test section flow velocity could be performed based on the pressure difference between the static pressure in the inlet (P_{ss}) and the test section (P_{ts}). The wind tunnel was equipped with a ring of pressure taps around the inlet and test section so that there was one pressure tap on each of the four walls in these two locations. The pressure taps at each location were connected through a single tube to the two sides of a differential pressure

transducer. With the measurements provided by this transducer, the velocity of the test section could be computed by Eq. 2.22. In this equation, A_{ss} and A_{ts} represent the areas of the inlet settling section and test section respectively, and ρ_{amb} is the ambient air density. This equation is valid under the assumption of a steady, inviscid, incompressible flow which is justified due to the low operational Mach number of the tunnel ($M_\infty \leq 0.18$).

$$V_\infty = \sqrt{\frac{2(P_{ss} - P_{ts})}{\rho_{amb}\left(1 - \left(\frac{A_{ts}}{A_{ss}}\right)^2\right)}} \tag{2.22}$$

The ambient air density was calculated according to the ideal gas law,

$$\rho_{amb} = \frac{P_{amb}}{RT_{amb}} \tag{2.23}$$

where the ambient temperature and pressure were measured in the testing area near the inlet to the wind tunnel.

2.2.2 Airfoil Model

The airfoil investigated in this study was a transonic Griffith/Goldschmied type airfoil which was designed for long runs of laminar flow and significantly reduced pressure drag. The reduction or elimination of pressure drag was accomplished through a built-in suction and blowing system. The suction slot on the airfoil was located in the center 14" of the span from a chord-wise location of $0.825c$ to $0.875c$. The airfoil model was constructed in three pieces using stereolithographic 3D printing methods, and had a chord length of 18". The primary piece consisted of the leading edge of the airfoil and terminated just before the suction slot on the upper surface. The second largest piece was the trailing-edge portion of the airfoil, which incorporated the suction and blowing systems. The final piece of the airfoil model was the lower-surface section which joined the leading edge to the trailing edge. All three of the 3D printed sections were fastened to two steel spars which were clamped to a wind tunnel force balance. Countersunk screws were used to fasten the pieces so that the holes could be smoothed over for testing. A rendering of the airfoil model is shown in Figure 2.24. Each of the three separate sections are different in color so that they may be more easily observed, and the suction slot region is shown in white.

Two separate trailing edge pieces were manufactured, one with a blowing slot for mass flow ejection and one without the blowing slot. Both trailing edge pieces were designed with a suction plenum which was open on the airfoil surface. The suction slot was then completed by inserting an additional 3D printed grating which was contoured to match the airfoil profile. Three different plenum covers were manufactured to investigate the sensitivity of the suction system to the type of grating used. One of the covers was designed with three large rectangular openings in the stream-wise direction. These slots were angled at 90° downward relative to the horizontal. Another cover was designed with

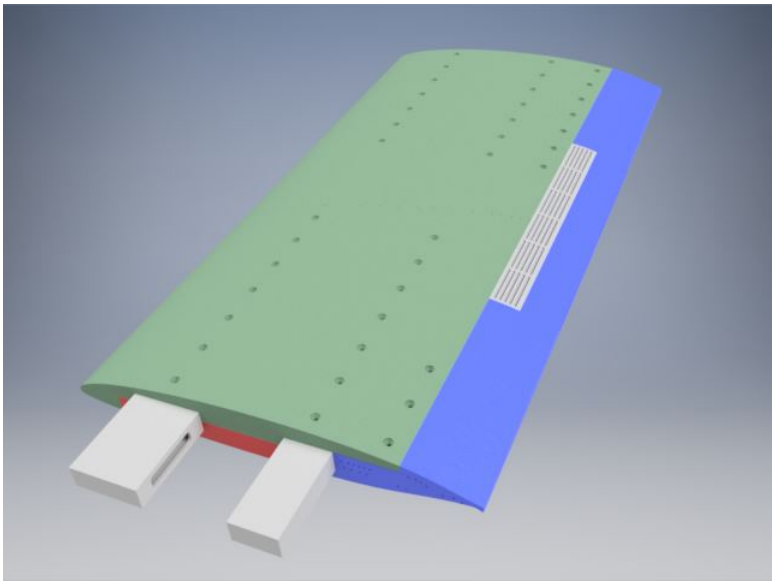

Figure 2.24: A rendering of the airfoil model.

five stream-wise rectangular openings, angled at 65°. The final cover was a porous plate design, with a series of rows with equally-spaced circular holes angled at 60° relative to the horizontal. A side-by-side comparison of the three suction plenum covers is shown in Figure 2.25. The blowing-enabled trailing edge was equipped with a blowing plenum as well as a blowing slot which spanned the same center 14" of the airfoil model. The suction and blowing plenums were transitioned to circular holes at the end of the airfoil span opposite where the spars are exposed. These circular holes allowed the suction system to be attached to the airfoil through the ceiling of the wind tunnel. A diagram showing the internal suction and blowing plenums is given in Figure 2.26.

The model was also equipped with a series of 64 pressure taps which were printed into the model material. Each of the taps were 0.06" in diameter. The pressure taps on the upper and lower surface were swept across the span at an angle of 12° with respect to the airfoil center chord to prevent the potential transition of flow due to an upstream tap from affecting the flow seen by a downstream tap. The pressure taps which were located in the trailing-edge region were routed to the span-wise end of the airfoil next to where the spars extend so that polyurethane tubing could be attached to these taps through the wind tunnel floor. The pressure taps which were located on the other two sections of the airfoil were routed to an internal cavity between the two spars. The main spar was of hollow construction with access holes on the sides inside the airfoil cavity as well as outside the airfoil where the spars extend. These access holes allowed polyurethane tubing to be threaded through the spar and attached to the pressure taps inside of the airfoil cavity. All of the pressure taps were attached by inserting a small length of 0.04" in diameter polyurethane tubing into the tap and fastening it in place with epoxy. Tubing adapters were then used to attach the standard 0.06" polyurethane

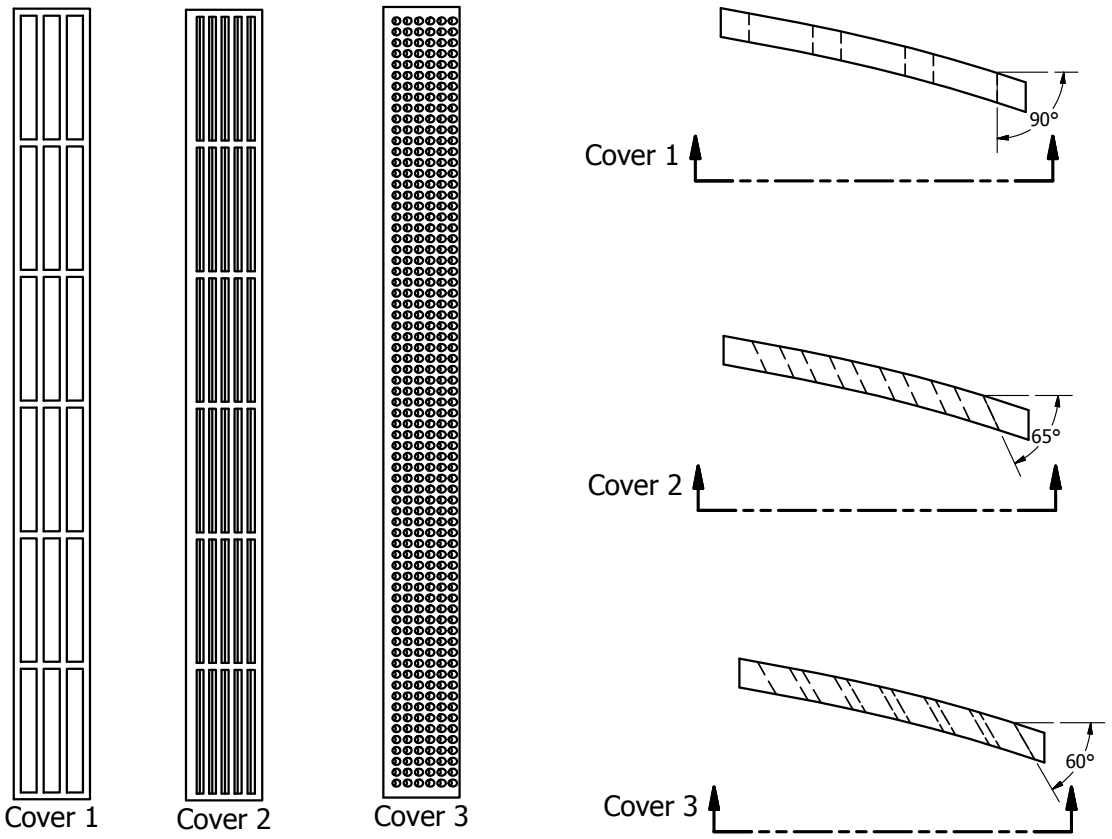

Figure 2.25: A diagram of the suction plenum covers.

tubing to the 0.04” polyurethane tubing. The blowing trailing edge piece was designed with fewer pressure taps due to the additional internal space consumed by the blowing plenum.

The airfoil model was mounted vertically inside the wind tunnel with the upper surface facing the control room. The spars extended through the tunnel floor and were fastened to an external three-component force balance which was used in this study only to set the angle of attack of the airfoil model. No force measurements were made with the balance because the airfoil did not have an isolated load path to the balance, due to the attached suction system. The spars were attached to the balance with L-brackets which were tightened on each side of the spars to hold them in place. Due to the thin nature of this airfoil, the spars were aligned in a manner not typical for the existing brackets. As a result, it was necessary to use several 0.25” aluminum shims to hold the spars in place in the brackets. A custom tunnel ceiling was installed which featured a large rotating aluminum turntable above the airfoil model. The airfoil model was pinned to the ceiling with a single 3/4” bolt which fastened into the top of the main spar. The rotating

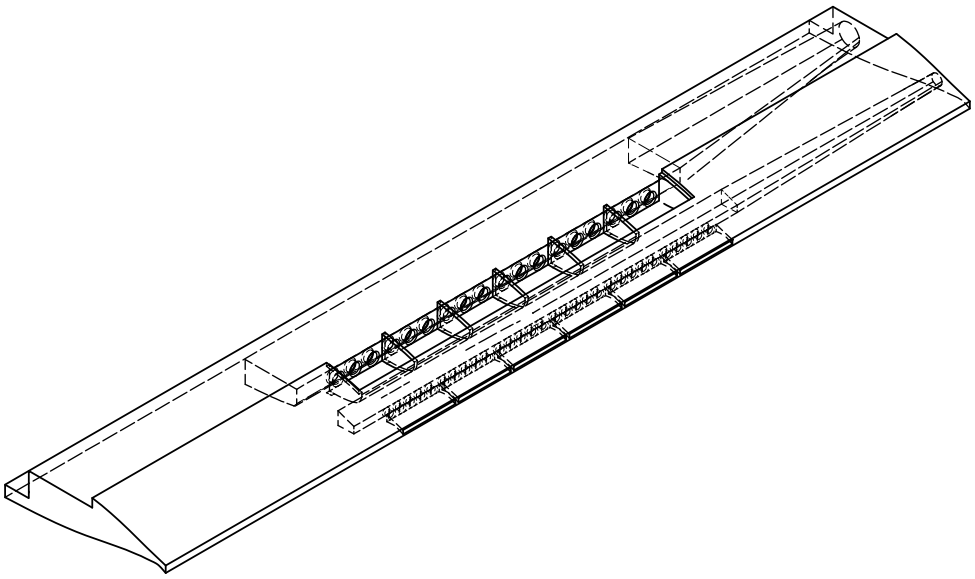

Figure 2.26: A diagram of the internal suction and blowing plenums.

ceiling was implemented in order to allow the suction system to interface with the airfoil model from the top of the wind tunnel while simultaneously allowing for changes in the airfoil angle of attack. An image of the model mounted inside the wind tunnel is shown in Figure 2.27.

2.2.3 Suction System

The suction and blowing for the airfoil model was supplied by an Atlantic Blowers three phase AC centrifugal blower. The blower was connected to the 208 V power supply located near the tunnel inlet. The suction level of the blower was controlled by varying the speed of the blower motor. The blower motor speed was regulated using a TECO variable frequency drive (VFD) which was rated for a 2 hp motor. The suction and blowing ports on the blower were equipped with standard 2" NPT threads and an over-pressure relief valve on the pressure side of the blower. A pipe adapter was installed in order to transition the 2" ports to 1.25" rubber hoses which could interface with the airfoil model. Custom adapters which reduced the 1.25" hose inner diameter to the diameters of the suction and blowing plenum holes in the airfoil model (0.858" and 0.432" respectively) were machined out of steel. The blower system was mounted to the top of the wind tunnel, and the suction and blowing hoses were attached to the airfoil model and sealed with a silicone

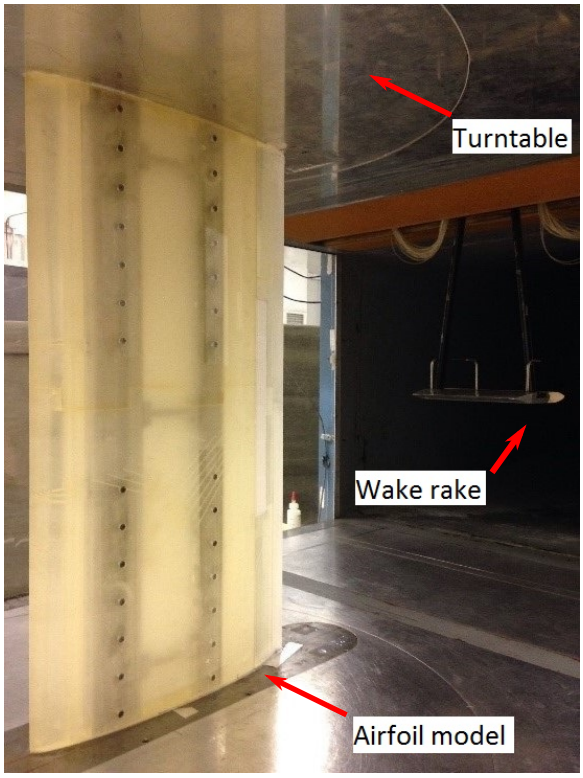

Figure 2.27: The airfoil model installed inside the wind tunnel.

sealant. The hoses were long enough to allow the airfoil model and tunnel ceiling to rotate freely as the angle of attack was changed. An image of the centrifugal blower is shown in Figure 2.28.

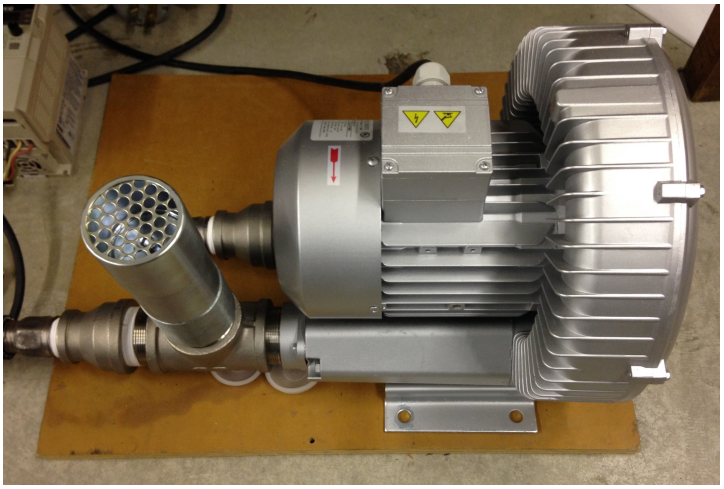

Figure 2.28: Atlantic Blowers centrifugal blower.

2.2.4 Wake Traverse System

Measurements of the total pressure in the wake of the airfoil were taken by a wake rake system which was installed in the test section of the tunnel 1.17 chord lengths downstream of the trailing edge of the airfoil model. The wake rake can be seen in Figure 2.27 downstream of the airfoil model (on the right half of the image). The wake rake consisted of a series of 59 total pressure probes, each of which was manufactured from 0.04" steel tubing and aligned in an array parallel to the freestream flow across a total width of 9.75". The wake rake was mounted to a two-axis Zaber traverse system which was installed above the wind tunnel in a large wooden plenum. The plenum was installed to ensure that no air would leak into the tunnel during operation. An image of the plenum is shown in Figure 2.29. The vertical (airfoil span-wise) and horizontal position of the wake rake could be precisely controlled with the traverse system. During all testing, the vertical position of the wake rake was set to be located at the center-span of the airfoil model. Due to the nature in which the pressure taps on the airfoil model were swept along the span, no taps were present on the airfoil section upstream of the center-span wake survey location. This ensured that laminar flow would be maintained over this region for accurate drag measurement.

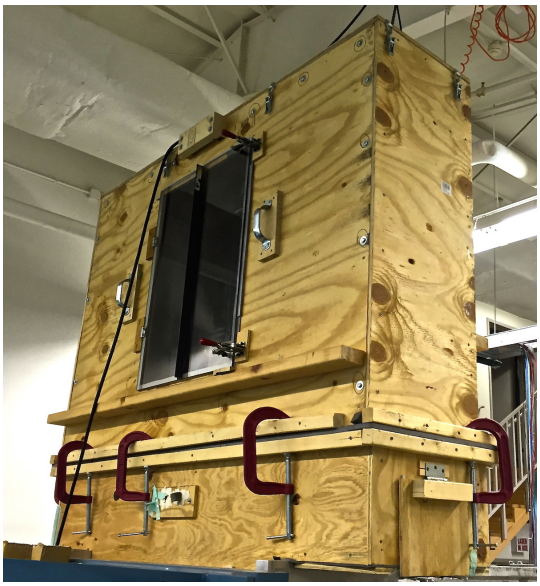

Figure 2.29: An image of the plenum enclosing the Zaber traverses.

The two-axis wake-rake positioning system was composed of two linear actuators which were manufactured by Zaber Technologies. Each of the actuators consisted of a built-in stepper motor, encoder, and controller. The stage of the traverse was mounted to a lead screw which allowed the traverse stage to be precisely positioned. The vertical traverse was a standard Zaber model A-LST1000A-E01-KT07 traverse with a 1000 mm range of motion. The horizontal traverse was a custom made Zaber A-LST1250B-E01-ENG1561-KT07 with a 1250 mm range of motion.

A table summarizing the mechanical properties and performance parameters of both of the Zaber traverses is given in Table 2.3. All of the motion for the two-axis system was controlled by programs in LabVIEW, where the vertical location of the traverse was set in the program input files, and the horizontal range of motion was determined through an automated wake-locating routine, as discussed in Section 2.2.6.3.

Table 2.3: Zaber Traverse Performance Metrics

	Vertical Stage	Horizontal Stage
Model	A-LST1000A-E01-KT07	A-LST1250B-E01-ENG1561-KT07
Microstep Size	0.124023438 μm (0.00000488281251 in)	0.49609375 μm (0.000019531250 in)
Linear Motion per Motor Revolution	1.5875 mm (0.062500 in)	6.35 mm (0.250 in)
Travel Range	1000. mm (39.37 in)	1250. mm (49.21 in)
Accuracy (Unidirectional)	250. μm (0.00984 in)	250. μm (0.00984 in)
Repeatability	$< 2\mu$m ($<$ 0.00005 in)	$< 2\mu$m ($<$ 0.00008 in)
Backlash	$< 5\mu$m ($<$ 0.0002 in)	$< 10\mu$m ($<$ 0.0004 in)
Maximum Speed	22 mm/sec (0.87 in/sec)	100. mm/sec (3.94 in/sec)
Minimum Speed	0.0012 mm/sec (0.000047 in/sec)	0.00465 mm/sec (0.000183 in/sec)
Speed Resolution	0.0012 mm/sec (0.000047 in/sec)	0.00465 mm/sec (0.000183 in/sec)
Peak Thrust	700. N (157 lb)	260. N (58.5 lb)
Maximum Continuous Thrust	560. N (126 lb)	260. N (58.5 lb)
Mass	6.90 kg (0.473 slug)	6.90 kg (0.473 slug)

2.2.5 Data Acquisition System

All of the data acquisition during the low-speed wind tunnel testing was performed on a Dell Precision T3400 computer equipped with 4GB of RAM and a 2.83 GHz Intel quad-core processor running a 32-bit Windows XP operating system. The data acquisition and tunnel equipment were controlled through a LabVIEW graphical user interface. This LabVIEW program allowed the user to specify the tunnel Reynolds number and view experimental data as it was collected. Modifications to input files could be made to specify sequences of testing parameters, such as the airfoil angle-of-attack range. Analog signals controlling the force balance and wind-tunnel VFD were sent through RS-232 communication. Digital signals sent through USB were used to control the two-axis wake traverse system. Digital signals were also acquired through USB from a National Instruments USB-TC01 Thermocouple measurement device. Signals from the DTC/Initium system were acquired through a TCP/IP Ethernet connection. All of the analog signal communications to the computer were converted with a National Instruments PCI-6052E 16-bit analog to digital converter board.

2.2.6 Pressure Measurements

The pressure measurements which were acquired during the low-speed testing can be broken into two categories. The first of these are measurements of the static pressure distribution around the airfoil, and the second are measurements of the total pressure in the airfoil wake. Measurements from both of these categories were acquired through a DTC Initium differential pressure system manufactured by Esterline, Inc. This system consisted of the Initium unit connected to five model ESP-32HD miniature electronically-scanned pressure (ESP) units. Each of these units had 32 pressure ports which could be connected to the model pressure taps or wake rake. The ports were designed to be connected to 0.063" tubulation pressure tubing. The units were also equipped with a run-reference port (R_r), a calibration reference port (R_c), two ports to move the internal calibration manifold (C_1 and C_2), and a calibration pressure port (Cal).

The five ESP modules were labeled J_1 through J_5 and had the following pressure measurements ranges. The J_1 module had a ± 5 psid range and was connected to the airfoil leading-edge pressure taps since the highest pressure differences from test-section static were expected to be measured there. Modules J_2 and J_3 had ± 1 psid ranges and were connected to the remainder of the airfoil pressure taps. Modules J_4 and J_5 had ± 0.35 psid ranges and were connected to the pressure probes on the wake rake, since the lowest pressure differences were expected in that region. The modules connected to the airfoil pressure taps (J_1 - J_3) were referenced to the test-section static pressure (P_{os}) to allow for direct calculation of the pressure coefficient through division of this measured quantity by the dynamic pressure. The modules which were connected to the wake-rake total pressure probes (J_4 and J_5) were referenced to the ambient laboratory pressure which was assumed to be the same as the tunnel total pressure. Before each test run, the Initium system was zeroed to ensure accurate readings.

2.2.6.1 C_p Distributions

One of the ports on module J_3 was connected to the steady-state pressure location just downstream of the flow conditioning inside the nozzle. This allowed for a direct measurement of $(P_{ss} - P_{ts})$ which was used to calculate the tunnel dynamic pressure. Assuming the velocity could be calculated according to Eq. 2.22, the dynamic pressure

$$q_\infty = \frac{1}{2}\rho_\infty V_\infty^2, \tag{2.24}$$

could be calculated as:

$$q_\infty = \frac{P_{ss} - P_{ts}}{1 - \left(\frac{A_{ts}}{A_{ss}}\right)^2}. \tag{2.25}$$

The pressure coefficient, C_p, for each of the pressure taps around the airfoil could then be calculated based on the dynamic pressure. The conventional definition of the pressure coefficient is given by

$$C_p = \frac{P - P_\infty}{q_\infty}, \tag{2.26}$$

where P is the measured pressure local to the airfoil surface, and P_∞ is the freestream static pressure. Since the pressure modules which were used to measure the static pressure distribution around the airfoil were referenced to the test-section static pressure (which was assumed to be equal to the freestream static pressure), the pressure coefficient could then be directly computed by dividing the measurement of $(P - P_{ts})$ by the calculated dynamic pressure, assuming that the free stream static pressure was equal to the measured test-section static pressure.

2.2.6.2 Airfoil Force and Moment Coefficients

The measured static pressure distribution around the airfoil was also used to calculate the airfoil lift coefficient (C_l) and quarter-chord pitching moment coefficient (C_m). The computation of these values began by breaking the airfoil up into a discrete number of panels, each of which was bounded by a node placed at the locations of the pressure taps. The airfoil surface was approximated by fitting straight lines between each pair of adjacent nodes so that the normal and axial forces on each segment due to the static pressure on that segment could be calculated easily. The value of the static pressure acting on each segment was assumed to be the average of the pressures measured at each tap bordering the segment. Since the static pressure acted in a direction normal to each of the segments, the contribution to the sectional chord-normal force from each panel with index i , $\Delta F'_{N_i}$, was calculated according to Eq. 2.27, where x_i is the x-location of the i'th panel node. The contribution to the chord-axial force from each panel, $\Delta F'_{A_i}$, was calculated according to Eq. 2.28, where y_i is the y-location of the i'th panel node.

$$\Delta F'_{N_i} = \frac{P_i + P_{i+1}}{2}(x_{i+1} - x_i) \tag{2.27}$$

$$\Delta F'_{A_i} = \frac{P_i + P_{i+1}}{2}(y_{i+1} - y_i) \tag{2.28}$$

The total sectional chord-normal (F'_N) and chord-axial (F'_A) forces were then calculated simply by summing the contributions from each of the discrete panels. The forces were computed explicitly by Eq. 2.29 and 2.30 respectively.

$$F'_N = \sum_{i=1}^{n-1} \Delta F'_{N_i} \tag{2.29}$$

$$F'_A = \sum_{i=1}^{n-1} \Delta F'_{A_i} \tag{2.30}$$

The sectional lifting force of the airfoil, L', is defined as the force acting normal to the direction of freestream flow. In order to calculate L', it was therefore necessary to take the components of the chord-normal and chord-axial forces which act in the direction of lift. This calculation was accomplished by taking the product of the chord-normal force with the cosine of the angle of attack and subtracting the product of the chord-axial force with the sine of the angle of attack, as shown in Eq. 2.31. In this equation, α is the airfoil angle of attack with respect to the freestream flow.

$$L' = F'_N cos\alpha - F'_A sin\alpha \tag{2.31}$$

The contribution from each of the discrete panels to the sectional quarter-chord pitching moment ($\Delta M'_{c/4_i}$) was also calculated from the chord-normal and chord-axial force contributions of each panel according to Eq. 2.32. In this equation, $x_{c/4}$ is the x-location of the airfoil quarter-chord position.

$$\Delta M'_{c/4_i} = \Delta F'_{N_i}\left(x_{c/4} - \frac{x_i + x_{i+1}}{2}\right) + \Delta F'_{A_i}\left(\frac{y_i + y_{i+1}}{2}\right) \tag{2.32}$$

As before, the total sectional quarter-chord moment coefficient can simply be calculated as the sum of the contributions from each of the discrete panels as shown in Eq. 2.33.

$$M'_{c/4} = \sum_{i=1}^{n-1} \Delta M'_{c/4_i} \tag{2.33}$$

The non-dimensional lift coefficient and quarter-chord pitching moment coefficient were calculated through division by the dynamic pressure times the airfoil chord, and the dynamic pressure times the chord squared, respectively. In Eq. 2.34 and 2.35, c is the airfoil chord length.

$$C_l = \frac{L'}{q_\infty c} \tag{2.34}$$

$$C_m = \frac{M'_{c/4}}{q_\infty c^2} \tag{2.35}$$

2.2.6.3 Wake Drag Calculation

Measurements of the total pressure in the wake of the airfoil as previously described in Section 2.2.4 were used to compute the drag coefficient (C_d) of the airfoil section using standard momentum-deficit theory as outlined by

Jones [27] and Schlichting [28]. This theory rests on the assumption that there exists a plane far downstream of the model in the test section where the wake static pressure and freestream static pressure are equal to each other. A schematic of this flow is shown in Figure 2.30. The flow properties at this theoretical plane are denoted with the subscript 1. Under this assumption, the sectional drag force can be found from Eq. 2.36. In this equation and in the subsequent equations to follow, properties which were measured at the plane corresponding to the location of the wake-rake are denoted with the subscript w. The w plane was assumed to exist between the trailing edge of the airfoil and plane 1.

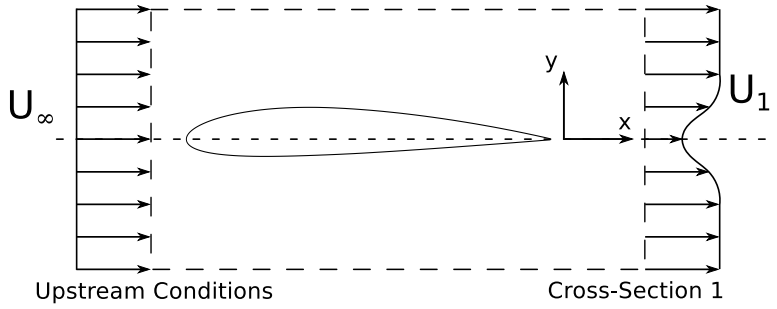

Figure 2.30: Control volume for the one-dimensional momentum deficit method.

$$D' = \int \rho U_1 (U_\infty - U_1)\, dy_1 \tag{2.36}$$

In order to cast this equation in a useful form, several steps must be completed. First, by assuming that an incompressible streamtube passes through planes 1 and w, the conservation of mass equation can be written as,

$$U_1 dy_1 = U_w dy_w. \tag{2.37}$$

By substituting this representation of the conservation of mass into Eq. 2.36, the following is obtained:

$$D' = \int \rho U_w (U_\infty - U_1)\, dy. \tag{2.38}$$

In order to express the sectional drag in terms of the pressures which were measured in the wind tunnel, the following three applications of Bernoulli's equation at plane w, plane 1, and the tunnel stagnation condition o were used,

$$P_\infty + \frac{1}{2}\rho U_\infty^2 = P_{o,\infty} \tag{2.39a}$$

$$P_1 + \frac{1}{2}\rho U_1^2 = P_{o,1} \tag{2.39b}$$

$$P_w + \frac{1}{2}\rho U_w^2 = P_{o,w}. \tag{2.39c}$$

Solving for the velocities in Eq. 2.39 and substituting into Eq. 2.38 yields a new expression for the sectional drag. If it is also assumed that there are no total pressure losses between planes 1 and w, so that $P_{o,1} = P_{o,w}$, the drag can then be expressed in the form of Eq. 2.40.

$$D' = 2\int \sqrt{(P_{o,w} - P_w)}\left(\sqrt{(P_{o,\infty} - P_\infty)} - \sqrt{(P_{o,w} - P_\infty)}\right) dy. \tag{2.40}$$

Further assuming that all of the pressure loss in the wake is due to the velocity deficit, it was also assumed that $P_w = P_\infty$. This assumption in conjunction with Bernoulli's equation for planes w and o yields the following representation of the wake dynamic pressure,

$$q_w = q_\infty - \left(P_{o,\infty} - P_{o,w}\right). \tag{2.41}$$

Substitution of this expression for the wake dynamic pressure into Eq. 2.40 yields the final expression for the sectional drag,

$$D' = 2\int \sqrt{q_\infty - (P_{o,\infty} - P_{o,w)}}\left(\sqrt{q_\infty} - \sqrt{q_\infty - \left(P_{o,\infty} - P_{o,w}\right)}\right) dy. \tag{2.42}$$

Which can be solved since the value of q_∞ is known. The quantity $(P_{o,\infty} - P_{o,w})$ can be directly computed from the measured pressure values. Since the quantity which was actually measured was $(P_{o,w} - P_{amb})$ inside the airfoil's wake, and $(P_{o,\infty} - P_{o,amb})$ outside of the wake, the desired pressure difference could be computed as

$$P_{o,\infty} - P_{o,w} = \left(P_{o,\infty} - P_{amb}\right) - \left(P_{o,w} - P_{amb}\right). \tag{2.43}$$

By substitution of this pressure difference into Eq. 2.42 and through trapezoidal numerical integration, the contribution of drag from the portion of the wake between pressure probe with index i and index $i+1$ on the wake rake can be written as

$$\Delta D'_i = \left[\sqrt{q_\infty - \left(P_{o,\infty} - P_{o,w_i}\right)}\left(\sqrt{q_\infty} - \sqrt{q_\infty - \left(P_{o,\infty} - P_{o,w_i}\right)}\right) + \right.$$
$$\left.\sqrt{q_\infty - \left(P_{o,\infty} - P_{o,w_{i+1}}\right)}\left(\sqrt{q_\infty} - \sqrt{q_\infty - \left(P_{o,\infty} - P_{o,w_{i+1}}\right)}\right)\right]\left(y_i - y_{i+1}\right). \tag{2.44}$$

The total sectional drag of the airfoil could then be determined by summing the contributions from each part of the wake using

$$D' = \sum_{i=1}^{n_{rake}-1} \Delta D'_i, \tag{2.45}$$

where the number of probes used to measure the wake is given by n_{rake}. During the wake measurement process, the edge of the wake region was determined by the locations where the magnitude of the rate of change of wake pressures in the y-direction was less than 0.01 psi/inch across both of the wake tails. Only pressure measurements from within the region of the wake bounded by these wake tails were used in calculated the drag of the airfoil.

Finally, the drag coefficient of the airfoil could be computed as

$$C_d = \frac{D'}{q_\infty c}. \tag{2.46}$$

2.2.7 Flow Visualization

The flow over the upper surface of the airfoil was visualized using a fluorescent oil surface flow visualization technique. This technique allowed for the identification of regions of laminar or turbulent flow, separation, and flow re-attachment. Flow visualization was performed at several angles of attack and a Reynolds number of 1.8×10^6. The flow visualization was primarily useful in determining whether or not the suction system was performing properly by promoting attached flow at the design angle of attack. The flow visualization method will now be described in detail.

First, the airfoil upper surface was covered with black contact paper. The contact paper served to provide a high-contrast background for the fluorescent oil in order to improve picture quality. Before application of the contact paper, it was necessary to wipe the airfoil model clean with rubbing alcohol to ensure that the adhesive side of the contact paper would adhere to the surface and to ensure that there would be no impurities trapped beneath the paper causing roughness. The contact paper had a smooth surface and was thin enough to ensure that the airfoil shape was approximately unaltered. An additional benefit of coating the airfoil model in contact paper was that the pressure taps were all covered to ensure that no oil was introduced into the pressure measurement system. Finally, two strips of yellow electrical tape were placed along the stream-wise length of the airfoil approximately one quarter of the airfoil span inboard from both edges. The chord-wise location in inches was marked on the pieces of tape to allow for a mapping of the observed flow features.

In preparation for the flow visualization process, a thin layer of 5W-30 motor oil was applied to the contact paper surface using a high-quality lab wipe. After this base coat of oil was evenly spread across the surface, a mixture of mineral oil and an oil-based fluorescent leak detector dye was applied to the surface with an airbrush. The airbrush was connected to a pressurized nitrogen tank which was set to supply 45 psi. The use of an airbrush ensured that the entire surface could be coated evenly with a fine spray of oil droplets. Throughout the oil application process, a black light was used to illuminate the oil mixture to ensure the entire surface was covered.

Once the surface was covered with a satisfactory layer of oil droplets, the airfoil was set to the desired angle of attack, and the wind tunnel was run at the desired Reynolds number for approximately four minutes. During this time,

the oil droplets on the surface of the airfoil would streak to show the time-averaged flowfield which was present on the surface. The tunnel was then turned off, and after the fan had completely stopped the airfoil was moved back to 0° angle of attack in order to photograph the surface. The overhead lights in the laboratory were turned off and the black lights were positioned once again to illuminate the surface and cause the leak detector die to fluoresce. Images of the oil pattern on the surface were then captured by a Nikon D3100 digital SLR camera mounted on a tripod. After a sufficiently good quality image was taken, the airfoil surface could be wiped clean and the process could be repeated for any desired conditions.

Chapter 3

Results and Discussion

In order to evaluate the design of a newly proposed propulsive wing concept, several wind tunnel tests were performed. First, testing of a cross-flow fan embedded in a duct was performed at transonic speeds. The purpose of this test was to characterize the performance of the embedded fan in the same conditions which would be present if the fan system were to be implemented on an actual aircraft, as well as to expand the understanding of cross-flow fan behavior further into the compressible flow regime. The results of this experiment are presented in Section 3.1. A second, low-speed wind tunnel test was performed to evaluate the performance of the designed airfoil with suction and blowing. This test was performed in a low-speed tunnel since no dedicated transonic tunnel with a large enough test section was available during the period of research. This test served to validate the computational methods which were utilized during the design of the airfoil section. The results of the low-speed test are presented in Section 3.2.

3.1 Cross-flow Fan Test Results

The transonic CFF performance was evaluated in this experiment through the collection of fan rpm and torque measurements, expansion surface pressure distributions, and surveys of the total pressure, total temperature, and velocity in the fan exit duct. Data were collected at various freestream Mach numbers ranging from 0.3 to 0.75, as well as at a variety of fan speeds ranging from 3000 rpm to 8000 rpm. These quantities can be used to evaluate the fan's ability to promote attached flow over the expansion surface, determine the mass flow of the embedded suction/blowing system, as well as to compute various non-dimensional quantities which characterize the performance of the cross-flow fan. These quantities were also used to scale the results of this experiment up to an actual aircraft scale.

While a significant amount of time was dedicated to testing the first cross-flow fan configuration (as discussed in Section 2.1.3.2), the results of those tests are only mentioned briefly as motivation for the final configuration. With the exception of this brief discussion, the rest of the results discussed in this section pertain to the final cross-flow fan and housing design which were described in detail in Section 2.1.3.3.

3.1.1 Expansion Surface Pressure Measurements

3.1.1.1 Initial Housing Results

The results for the initial housing design pressure distribution measurements are shown in Figure 3.1. In these plots, the data points that form the lower portion of the closed C_p distributions represent the static pressure measurements which were taken within the inlet and outlet ducts of the expansion surface. From Figure 3.1, it can be noted that there is virtually no difference in the pressure distributions as the fan rpm was varied from zero to 7000 rpm in increments of 1000 rpm. This result indicates that the fan embedded in its housing did not provide any assistance with pressure recovery. The same result was observed for Mach numbers of 0.5 and 0.6, shown in parts (a) and (b) of the figure, respectively.

A simple qualitative flow visualization analysis was also performed to verify the pressure distribution results. Small tufts of black thread were attached to the upper surface of the expansion surface with aluminum tape. The tunnel was then run at several Mach numbers and a variety of fan speeds. During all of these tests, the tufts were observed to bend in the upstream direction and chaotically vibrate in the flow. This visualization indicated that the flow was in fact detached, and that the fan was not performing properly.

Data were also taken in the inlet and outlet ducts, but no useful information could be learned from these data since the fan was not performing as desired. The results of this initial test led to a re-design of the cross-flow fan and housing configuration. The results from the testing of this second fan were much more promising, and shall now be discussed.

3.1.1.2 Final Housing Results

The pressure distributions which were measured across the upper surface of the expansion surface (the side exposed to the freestream flow) are shown in Figure 3.2 for a variety of test conditions. Each sub-figure corresponds to a sweep through several values of rpm at a fixed Mach number. The pressure distributions inside of the exit duct are not shown in these plots since they did not aid in determining whether or not the flow over the expansion surface was attached. It should also be noted that the pressure tap which was routed to the leading edge of the upper portion of the expansion surface did not properly form during the manufacturing process, and as such the first functioning pressure tap was located at approximately $\frac{x}{c} = 0.15$. The region of the expansion surface where the data was taken is shown underneath the plots in Figure 3.3. The locations of the active pressure taps corresponding to the data points are shown in the figure.

Figure 3.2 (a) depicts the pressure distribution at $M = 0.4$ for the fan-off case as well as for 5000 and 6400 rpm cases. Several observations can be noted from these distributions. First, the fan-off distribution of pressure across the surface indicates separated flow, as evident by the plateau in C_p across the stream-wise length of the surface.

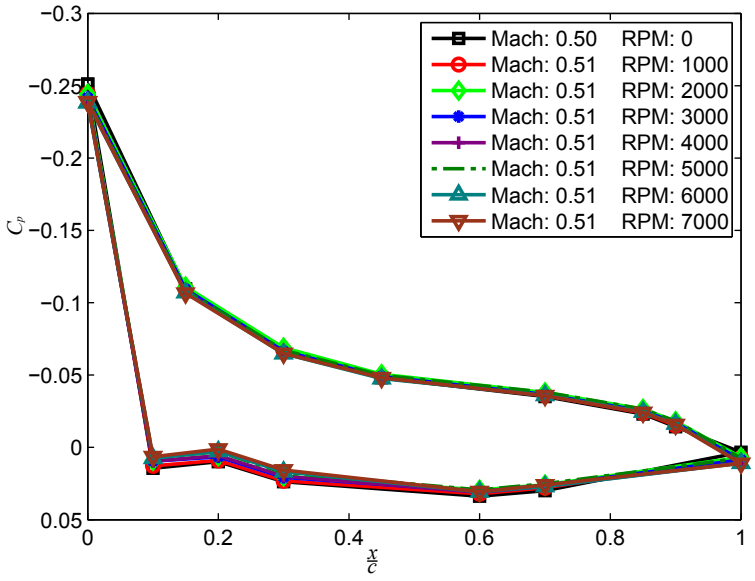

(a)

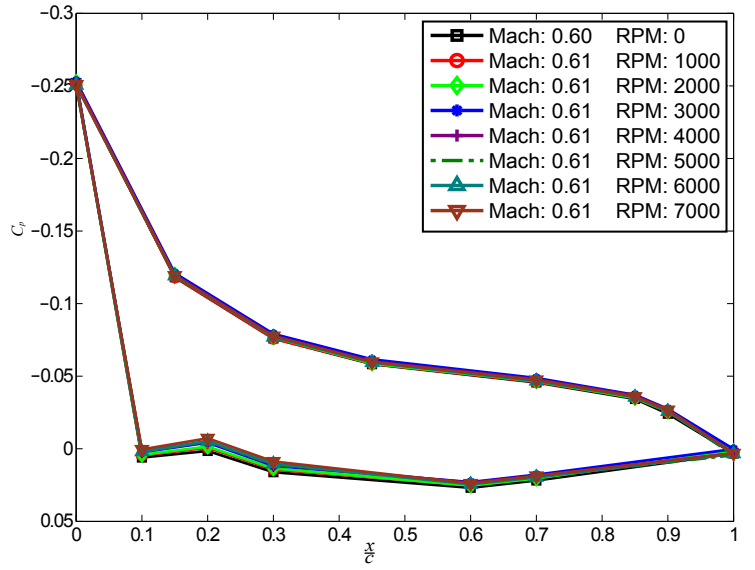

(b)

Figure 3.1: Expansion surface pressure distributions for the initial housing design for (a) $M = 0.5$ and (b) $M = 0.6$.

Conversely, the fan-on cases indicate an attached flow as evident by the concave-type pressure recovery across the expansion surface. This recovery in the surface pressure shows that the cross-flow fan is effective in retaining flow attachment over the simulated trailing edge in transonic conditions. This observation also serves to validate the second iteration of the fan and housing design, since such pressure recovery characteristics were not observed for the first cross-flow fan and housing setup. A distinct increase in pressure between the fan-off and fan-on cases is also present, as indicated by the shift of the entire curve towards the positive C_p direction. This indicates that the cross-flow fan can

provide the discrete static pressure rise necessary for the pressure thrust concept to work. Figure 3.2 (b) depicts the pressure distribution at $M = 0.5$ for rpm values of 0, 5500, and 7000. The same pressure recovery characteristics can be seen here as previously. In both the $M = 0.4$ and $M = 0.5$ cases, it can be noted that increasing the fan speed by approximately 1500 rpm did not drastically change the pressure distribution. This insensitivity of the pressure increase induced by the fan with increased rpm indicates that there is a saturation effect of the pressure recovery across the suction slot due to an increasing rotational rate of the fan.

Figure 3.2 (c) shows the pressure distribution at $M = 0.6$. The same pressure recovery attributes are again observed at this speed. For the $M = 0.6$ case, data were only collected at zero and 5600 rpm. Any significant increase in the rpm of the fan caused an over-current error to occur, indicating that the VFD was operating above safe limits. Any significant decrease in the rpm limited the power available to the fan and cause the motor to stall. For these reasons, no additional fan speeds were investigated for the $M = 0.6$ case. This case was still quite important for the results of the study, however, since this Mach number was the closest to the airfoil design Mach number of 0.7 for which a full data set was collected.

The expansion surface pressure distributions which were collected in this study show promise for the application of a cross-flow fan to provide suction when embedded in a transonic laminar flow airfoil. The cross-flow fan was able to provide flow attachment over the representative trailing edge expansion surface piece in transonic flow as well as a discrete rise in static pressure, indicating that it could do the same for the designed transonic Griffith/Goldschmied wing section. While no pressure data were collected at $M = 0.7$ due to the previously mentioned power limitations of the motor and VFD, it is reasonable to assume that the observed transonic cross-flow fan performance characteristics would hold true at $M = 0.7$.

3.1.2 Outlet Duct Measurements

Measurements of the total pressure, total temperature, and flow velocity were taken at 0.05” increments across the height of the exit duct. Due to the exposed inlet arc of the cross-flow fan in the second housing, no measurements could be made of the fan inlet conditions. The results of each of these duct surveys are discussed in this section. All of the duct surveys discussed here refer to surveys of the properties across the exit duct of the second cross-flow fan and housing configuration.

3.1.2.1 Total Pressure in the Exit Duct

Measurements of total pressure across the fan exit duct are shown below in Figure 3.4. Surveys for Mach numbers of 0.4 (a), 0.5 (b), and 0.6 (c) are shown for a variety of fan speeds. The average value of the total pressure in the duct is also shown as a vertical dashed line on the plots. In both cases (a) and (b) the total pressure in the duct can be seen to

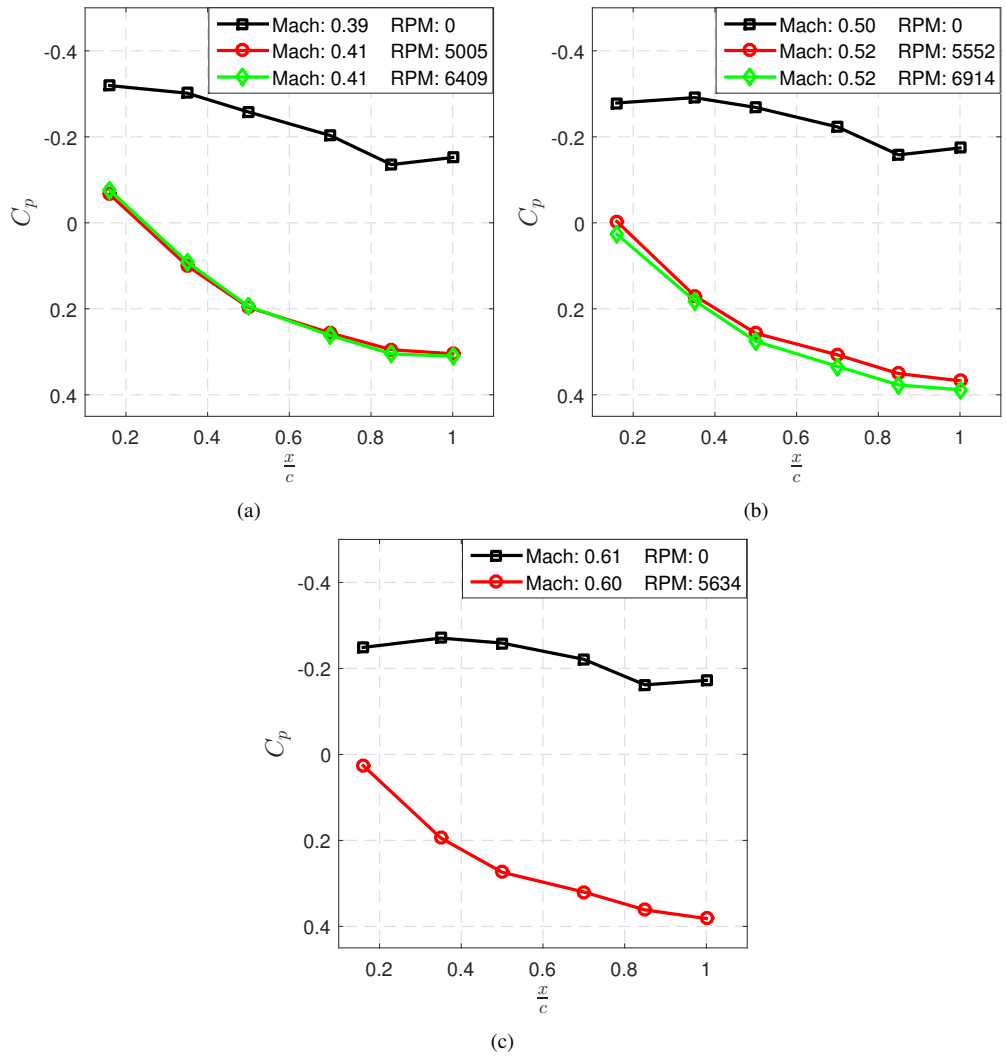

Figure 3.2: Expansion surface pressure distributions for (a) $M = 0.4$, (b) $M = 0.5$, and (c) $M = 0.6$.

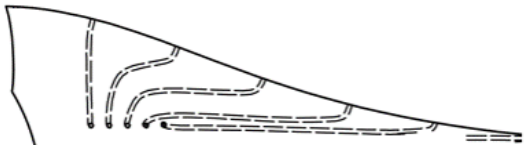

Figure 3.3: Expansion surface pressure distribution region for shown data.

increase as the fan speed increases, indicating that the fan is performing work on the fluid to raise the total pressure. This observation also serves as a validation of the second cross-flow fan and housing design. It can also be observed that the profiles indicate a region of higher total pressure towards the top of the exit duct. This observation holds true for each of the Mach number cases. This same observation was also made during the cross-flow fan experiments performed by Hancock [12]. As the Mach number of the freestream flow increases, the region of higher total pressure

is shifted towards greater pressure values. It can also be noted that as the Mach number is increased, the value of the total pressure in the lower half of the duct can be seen to decrease. The combination of these effects leads to a skewing of the total pressure in the duct towards higher values in the upper half and lower values in the lower half as the freestream Mach number is increased. The non-uniformity of these profiles across the duct show the sensitivity of the fan performance to the shape and location of the exit duct. Some of the non-uniformity can be attributed to the fact that there is a high level of swirl to be expected in the exit duct. As before, the fan rpm for the $M = 0.6$ case could not be increased beyond 5600, and a comparison between different rpm cases could not be made.

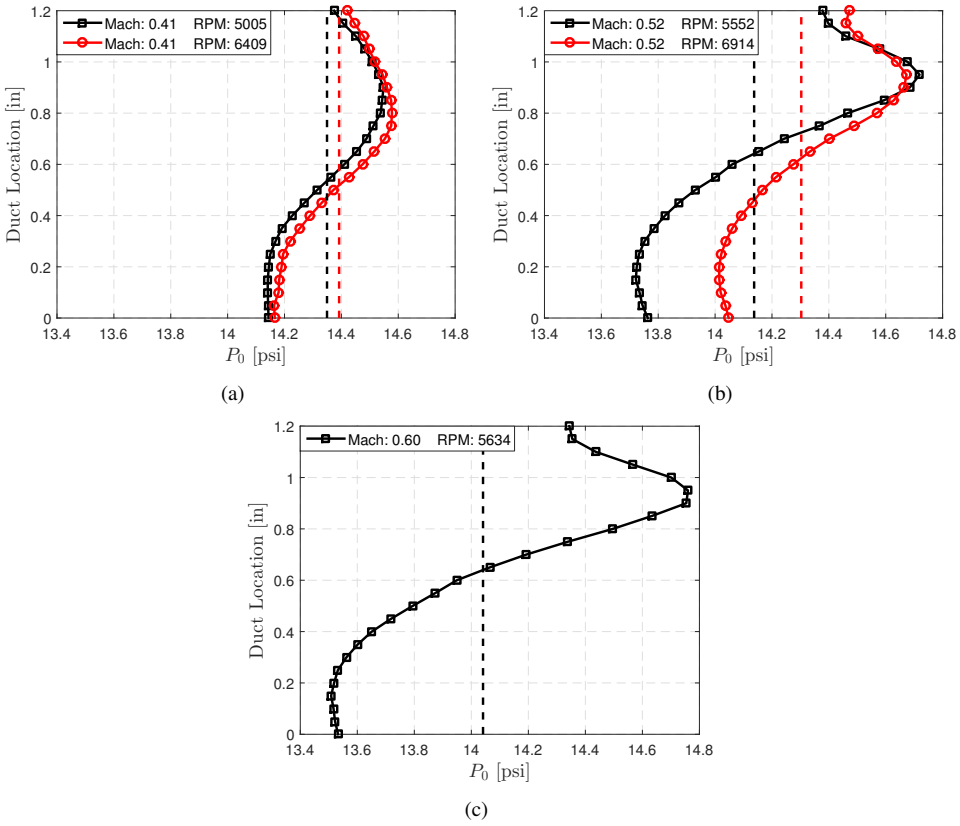

Figure 3.4: Duct total pressure distributions for (a) $M = 0.4$, (b) $M = 0.5$, and (c) $M = 0.6$.

3.1.2.2 Total Temperature in the Exit Duct

The profiles of total temperature across the exit duct are shown below in Figure 3.5. Again, cases are shown for $M = 0.4$ (a), $M = 0.5$ (b) and $M = 0.6$ (c). The total temperature profiles were much more constant across the duct than the total pressure profiles. A total temperature increase occurred in both cases (a) and (b) when the fan speed was increased. The shape of the temperature distribution remained relatively unchanged as the fan speed was increased, as well as when the freestream Mach number was increased from 0.4 to 0.5 to 0.6. This even distribution of the

temperature profile is in contrast to the pressure distribution which became more skewed as the Mach number was increased. In all cases, the average total temperature across the duct is shown as a dashed vertical line. In case (a), the average temperature increased by approximately 5.5° Celsius, and approximately 9° Celsius in case (b). Again, no second case was recorded for the $M = 0.6$ case. For case (c), the data points corresponding to the lower 0.2" of the outlet duct are missing, as the probe was damaged while this duct survey was being performed. The increase in total temperature in the exit duct as the fan speed was increased also indicated that the fan was performing work on the flow, and that the fan and housing combination was functioning as intended.

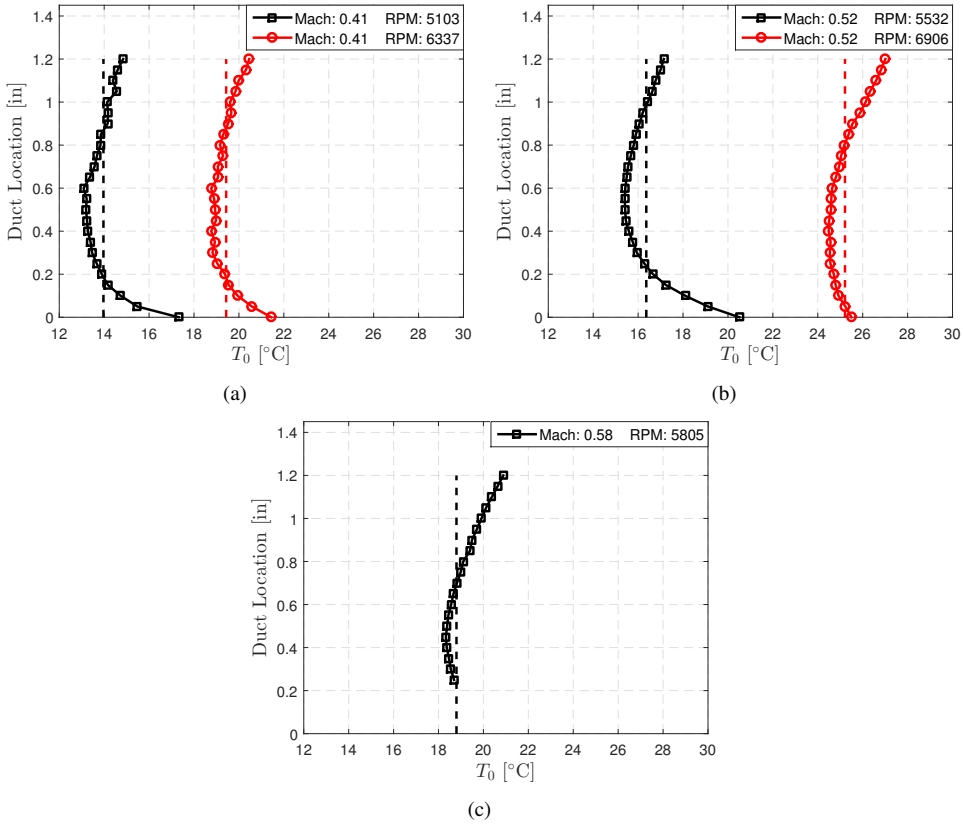

Figure 3.5: Duct total temperature distributions for (a) $M = 0.4$, (b) $M = 0.5$, and (c) $M = 0.6$.

3.1.2.3 Velocity in the Exit Duct

The velocity distributions in the exit duct were of particular importance to the study since the designed Griffith/Goldschmied type airfoil required a mechanism to provide mass-flow ejection out of the trailing edge. Measurements of the velocity in the duct were used to verify that the cross-flow fan was capable of providing the required suction and blowing velocities.

The measured velocity distributions across the exit duct are shown in Figure 3.6, for $M = 0.4$ (a), $M = 0.5$ (b) and $M = 0.6$ (c). The average duct velocities are also shown as vertical dashed lines. The average duct velocity can be seen to increase with fan rpm as expected in both the $M = 0.4$ and $M = 0.5$ cases. The shape of the velocity profile also remains relatively unchanged as the fan rpm is increased, with a slightly greater increase in velocity towards the floor of the duct. A slight decrease in velocity towards the duct ceiling can also be seen for the $M = 0.5$ case as the fan speed is increased. The shapes of the velocity profiles in the duct closely resemble the shape of the total pressure profiles, as would be expected.

As the freestream Mach number is increased, the upper half of the velocity profile is extended into regions of higher velocity, while the lower portion of the duct remains near 150 ft/s for all cases. This observation indicates that the larger increase in velocity towards the ceiling of the duct is partially due to the increase in freestream Mach number, and not solely due to the work performed by the fan. For the M = 0.4 case, the maximum duct velocity recorded was 220 ft/s. For the $M = 0.5$ case, the maximum velocity increased to 250 ft/s, and for the $M = 0.6$ case, the maximum velocity was 300 ft/s. However, less variation in the average duct velocity can be seen as the Mach number is increased. The average velocity for the $M = 0.4$ case (rpm = 5100) was 168.27 ft/s, which increased to 182.26 ft/s for the $M = 0.5$ case (rpm = 5600), and 196.4 ft/s for the $M = 0.6$ case (rpm = 5700). Since the difference in rpm is small between these cases, the difference in average velocity can be attributed to the increase in freestream Mach number.

The resulting averaged duct properties for each of the run cases mentioned above are presented in Table 3.1. The sixth column of the table contains the variable $\left(\frac{V}{V_\infty}\right)_{inlet}$, which is simply computed as the ratio of duct inlet velocity to freestream velocity. This parameter was used during the airfoil design phase to specify the quantity of suction required to attain proper airfoil performance. The final airfoil design required this ratio to attain a value of 0.0625. All of the measured duct velocities surpassed this requirement, attaining velocity ratio values around 0.1 for all cases. It is also interesting to note that this ratio remained relatively constant between the various Mach number and rpm cases.

The same quantity was also computed for the outlet duct velocity, $\left(\frac{V}{V_\infty}\right)_{outlet}$. The airfoil required this ratio to attain a value of 0.25, which was met and exceeded by all of the cases. As with the inlet velocity ratio, the outlet velocity ratio also remained relatively unchanged at a value near 0.35 between the different Mach number and rpm cases. The only exception is the $M = 0.4$ case where the values were closer to 0.4. This may indicate that the cross-flow fan was producing a higher relative duct velocity at lower Mach numbers. At Mach numbers near 0.4, the effects of compressibility and the potential for choking and separation on the fan blades was much lower than the higher Mach number cases, which may contribute to this effect.

The mass-flow rate in the exit duct was also computed for each of the test cases using the averaged duct data. Isentropic flow assumptions were used with the average values of the flow properties in the duct in conjunction with

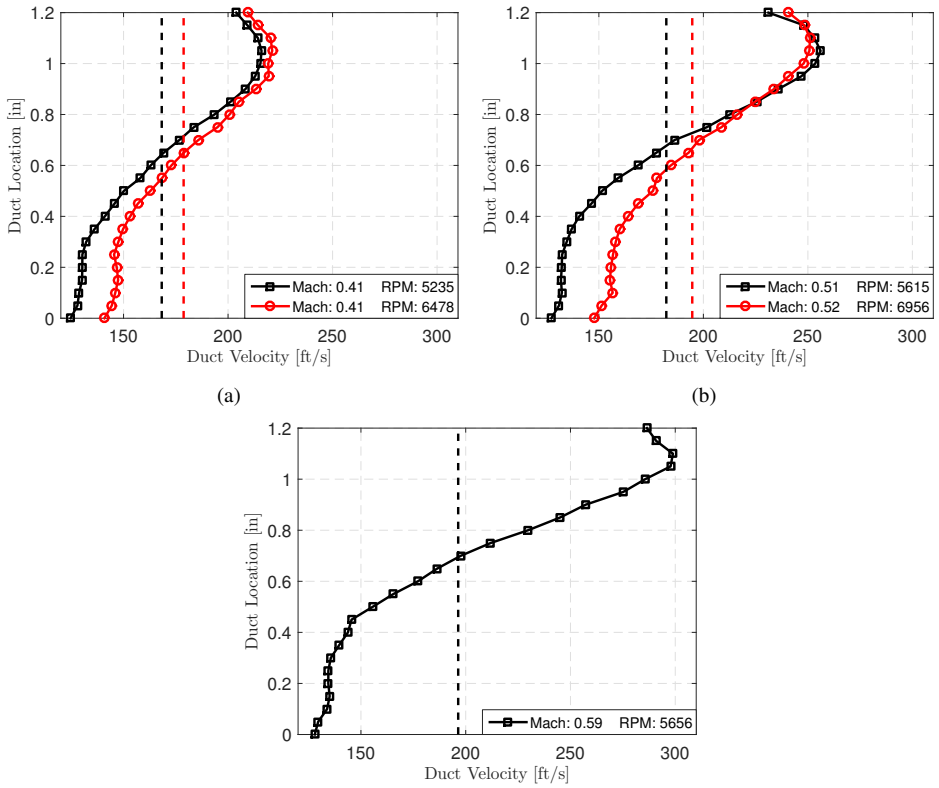

Figure 3.6: Duct velocity distributions for (a) $M = 0.4$, (b) $M = 0.5$, and (c) $M = 0.6$.

static pressure measurements taken from the taps located inside of the exit duct to compute the duct Mach number, allowing the mass flow rate to be calculated. The differences in mass-flow rate between the two different fan speeds for each Mach number case were relatively small. For the $M = 0.4$ case, the mass-flow rate actually decreased when the fan speed was increased. This could be due to the fact that the total temperature increase was relatively large when compared to the total pressure increase, which could have led to a decrease in density and therefore mass-flow rate, even with an increased volume flow rate. The decrease could also be due to the assumption which was made in the calculation that the static pressure was constant across the exit duct. This was seen as a weak assumption, but necessary since static pressure surveys were not performed.

Table 3.1: Duct Survey Results

M	rpm	$P_o[lbf/ft^2]$	T_o [° R]	V [ft/s]	$\frac{V}{V_\infty}_{inlet}$	$\frac{V}{V_\infty}_{outlet}$	$\dot{m}$ [slug/s]
0.41	5114.23	2066.33	516.81	168.27	0.125	0.38	0.0160
0.41	5993.73	2072.46	526.65	178.75	0.123	0.40	0.0157
0.52	5566.38	2035.77	521.13	182.26	0.110	0.33	0.0169
0.52	6925.31	2059.63	537.05	194.68	0.115	0.35	0.0177
0.59	5698.14	2021.91	525.51	196.41	0.103	0.31	0.0177

3.1.3 Fan Power Measurements

The mechanical power of the fan during all operating conditions was calculated from the measured torque and rpm values collected by the torque transducer. During testing, the fan was ramped up to speed before the tunnel air was turned on to prevent the fan from rotating backwards when the flow began. As a result, measurements of torque and rpm were made during every tunnel run as the Mach number was increased from zero to the desired test condition. This approach allowed for the collection of a wide range of data characterizing the power requirements of the cross-flow fan at a constant rpm as the freestream Mach number was varied. A plot of fan power vs. Mach number and fan rpm is shown in Figure 3.7. This figure includes all of the power data which were collected during the ramp-up phase of each wind tunnel run. The power consumed by the fan can be seen to increase both as the freestream Mach number increases and as the fan rpm increases.

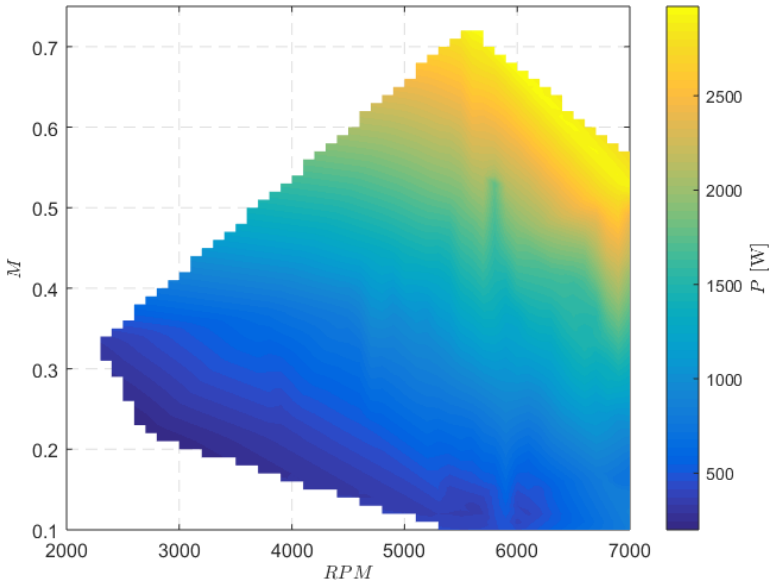

Figure 3.7: Fan power consumption as a function of M and rpm.

These data are also represented in Figure 3.8 where three lines of power vs. Mach number for a constant rpm are shown. It is important to note that the rpm of the fan did decrease slightly as the tunnel speed increased and more torque was applied. The value of rpm which is listed for each of these three lines corresponds to the steady-state rpm after the tunnel had reached its operating speed. The total variation in rpm from the beginning to the end of the tunnel startup period was typically on the order of magnitude of several hundred rpm. From Figure 3.8, the fan power increases linearly with Mach number for all three rpm cases, indicating a linear change in torque with changing Mach number at a fixed rpm. It can be noted that the slope of this line increases as the fan rpm is increased. Fan power data were collected up to $M = 0.73$. At this freestream Mach number, the motor system was unable to sustain stable

operation of the fan. As a result, pressure data and duct surveys were not performed at this Mach number. The 5" span of cross-flow fan used in this experiment consumed roughly 3 kW of power at an rpm of 5800. While this value does not mean much by itself, it proved to be very valuable to the study. The freestream Mach number for the airfoil configuration in this study was 0.7, allowing the fan power data collected during the experiment to be scaled up to the full aircraft system.

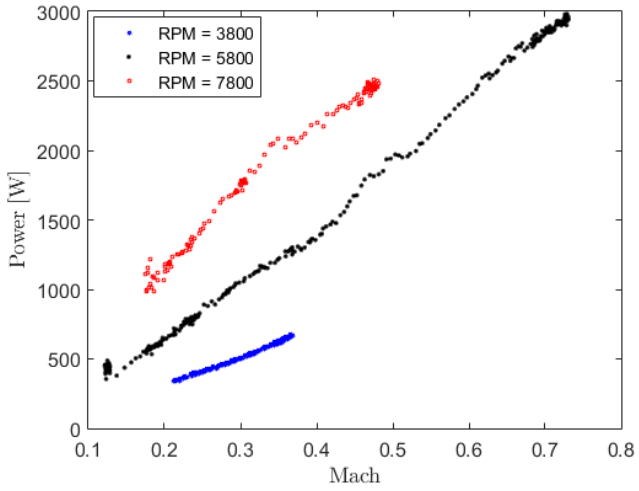

Figure 3.8: Fan power vs. M for various rpm.

3.1.3.1 Power Scaling Results

The Boeing SUGAR Refined aircraft was chosen as a baseline aircraft on which the proposed propulsive wing concept would be implemented. In order to evaluate whether or not the addition of the propulsive wing to the baseline aircraft would bring about any gains in overall power consumption, an aircraft systems-level analysis was required. While this analysis was not performed or discussed by the author of this thesis, the cross-flow fan power measurements were utilized to obtain an estimate for the power which would be required by a propulsive wing with an embedded cross-flow fan system. This scaling of power data was performed through the use of the flow and power coefficients, discussed in Section 2.1.11.

The values of the flow coefficient, ϕ, for both the inlet (suction) and outlet (blowing) side of the cross-flow fan which were computed from the experimental data are given in Table 3.2. The values for the aircraft suction and blowing flow coefficients were chosen to match those of the experimental data in order to properly scale between cases. This assumption, in conjunction with the inlet and outlet areas of the designed airfoil suction and blowing slots, was used to compute the fan tip speed which would be necessary to produce the same flow coefficient on the full-scale aircraft. The values of the experimental and scaled tip speeds are also given in the table.

Table 3.2: Fan Flow Coefficient for Test Conditions

	Experimental	Aircraft Scale
$\phi_{suction}$	0.7985	0.7985
$\phi_{blowing}$	0.7983	0.7983
U_o [ft/s]	85.395	76.8

The quantities which were used to compute the power coefficient as well as evaluate the power integral are given below in Table 3.3. These values were either directly measured or computed from the experimental data. Here, b refers to the span of the cross-flow fan in the wind tunnel, U_o is the fan tip speed, D_o is the fan diameter, and W_s is the power consumed by the fan. The flight conditions and scaled power values are given in Table 3.4. Initial results indicate that the fan system would consume 187 kW of mechanical power when implemented over the center 70% of the wing span on the SUGAR Refined aircraft cruising at an altitude of h = 40,000 ft with a flight speed of M = 0.7. In this table, $b/2$ refers to the portion of the semi-span of the full aircraft wing where the cross-flow fan will be utilized, and the subscripts *root* and tip denote the fan diameters at the wing root and most outboard portion of the fan respectively. It can be noted that the tip speed which is required of the full-scale aircraft is lower than that which was produced during the experiment. This indicates that the cross-flow fan was performing more work than necessary to provide flow attachment when implemented in the wind tunnel, which further expounds the observation made previously that there is a saturation in the effect of increasing the fan speed on flow attachment.

Table 3.3: Pre-scaled Test Data

W_s [W]	2880.8
b [in]	5
ρ [$slug/ft^3$]	0.0021364
D_o [in]	3.457
U_o [in]	85.395
λ	26.61
M	0.7014
rpm	5661.3

Table 3.4: Scaled Power Data

W_s [kW]	187.58
$b/2$ [ft]	42.4
ρ [$slug/ft^3$]	0.0005428
$D_{o,root}$ [in]	11.28
$D_{o,tip}$ [in]	4.94
U_o [in]	76.8
M	0.7

These initial power scaling results have been utilized in conjunction with a performance simulation of the SUGAR Refined aircraft with the transonic Griffith/Goldschmied airfoil and cross-flow fan system incorporated into the wing. The simulation has been used to quantify the fuel savings which could be gained if such a system were incorporated

on the wings of a transport aircraft, based on the power consumption and configuration changes required for proper implementation of the system. For further results of this study, the reader is directed to Perry et al. [18].

3.2 Airfoil Test Results

The low-speed wind tunnel tests which were performed served to validate the computational methods which were used to design the airfoil through comparisons of lift, drag, and moment polars, as well as comparisons of the pressure distributions around the airfoil between experimental results and computational predictions. Oil surface flow visualization was also performed on the upper surface of the airfoil model. The results of the low-speed wind tunnel tests and their comparison to the computational predictions are discussed in this section.

The computational results which are presented here for the purpose of comparison were not a part of the work completed by the author of this thesis. For details concerning the computational methods utilized for the airfoil design, the reader is directed to Perry et al. [18].

All of the testing of the airfoil was performed at a Mach number of 0.18, which corresponded to a Reynolds number of 1.8×10^6. Testing was also performed for a variety of suction levels, as well as with and without blowing out of the trailing edge of the model. Measurements of the airfoil wake profile were also acquired for comparison between different suction and blowing configurations. Testing was also performed with three different suction plate designs. Comparisons between these different configurations are also made in this section.

3.2.1 Comparison to Simulation

The primary purpose of the low-speed wind tunnel tests was to verify the computational methods which were utilized during the design of the airfoil. The low-speed tests also served to experimentally validate the static pressure thrust concept. The lift, drag, and moment characteristics of the airfoil as a function of airfoil angle of attack (α) are shown in Figure 3.9. In this figure, only the region of interest of the polars is shown to allow easy comparison between the different cases. In addition to the computational predictions, also shown on the plot are experimental results for the airfoil without suction, the airfoil with suction only, and the airfoil with suction and blowing.

It is important to note that the suction and blowing quantities presented in the legend of the figure are given in terms of hertz. This value represents the electrical frequency which was used to run the centrifugal blower which provided the suction to the airfoil. The blower was run at the highest rpm when the AC frequency was 60 Hz, and half rpm when it was run at 30 Hz. A mass-flow meter was purchased to measure the exact suction mass-flow which was applied to the airfoil model. Unfortunately, the addition of the mass flow meter into the pneumatic circuit which connected the blower to the airfoil model created such a large blockage that the blower could no longer adequately

provide suction to the model. As this was the case, it was necessary to quantify the amount of blowing in terms of the driving frequency of the blower motor.

From Figure 3.9, a comparison between the full power suction case and the predicted suction-only case can be made. Due to motor over-heating issues, experimental data were only collected over an angle of attack range of -3° to 3° for the full-power suction case. It can be noted that the experimentally measured lift curve slope was slightly less than that which was predicted by the simulations. Other than this slight difference in slope, the experimental measurements of C_l were close in value to those predicted in the simulation. Also shown on the figure is a half-power blowing case. In order to run the blowing case, it was necessary to cover half of the blowing slot in order to reduce the demands on the blower. It was also necessary to run the blower at half power in order to prevent overheating issues which occurred as a result of routing all of the suction mass flow through the small opening to the blowing plenum. From Figure 3.9, the blowing lift curve was slightly less linear than the suction case, deviating from the predicted values to a greater extent as the angle of attack was increased. At an angle of attack of 2°, a distinct decrease in the lift curve slope can be noted. The results of the blowing case should not be taken as representative of the actual capabilities of the airfoil section when the proper amount of suction and blowing is applied. Due to the limitations imposed by the blower capabilities, these results can only be taken as a first step towards validating the capabilities of the airfoil section with suction and blowing. The final case which is also shown in Figure 3.9 is an airfoil polar with no suction or blowing applied. It can be noted that both the suction only, and the suction and blowing case both show an increase in lift over the baseline (no suction) case. At an angle of attack of 4°, a shift in the lift curve can be noted in the baseline case.

The drag produced by the airfoil for the baseline, suction, and blowing cases as well as the computational predictions are also shown in Figure 3.9. Since the primary goal of the airfoil design was to use the pressure distribution in conjunction with suction and blowing to reduce pressure drag, the drag polars are of primary interest. It can be noted that near the design angle of attack of 0°, the experimentally-measured drag compares quite well with the computationally-predicted drag. This result is very encouraging, indicating that the static pressure thrust concept of a Griffith/Goldschmied airfoil can be applied to transonic wing sections. Away from the design angle of attack, the experimental drag values differ from the predicted values in a slightly more significant manner. The drag for the blowing case is also shown. As expected, the drag does not compare well to the predicted values, since the blowing system was not functioning at full capacity. The final point to note from the drag polars is that there was a significant decrease in drag between the baseline case and both the suction and blowing cases, indicating that the system was effective in negating the drag of the airfoil section. A net thrust was not realized, however, again due to the poor performance of the blowing system.

The final subplot of Figure 3.9 shows the airfoil moment coefficients. All three of the experimental cases exhibited moment values that were slightly more positive than the values predicted by the simulation. The suction only case did show a decrease in moment over the baseline case. It is interesting to note that the application of suction only, or suction and blowing seems to have a relatively small effect on the moment produced by the airfoil section.

In general, there is fairly good agreement between the computational and experimental airfoil polars. The small differences that do exist can be largely attributed to the fact that the actual quantity of suction and blowing could not be adequately measured or controlled during the experiment. If the required values for suction and blowing mass flow were actually met, it is expected that the experimental and computational results would be much more aligned. It is also interesting to note that the slope of the C_m vs. α curve is negative for negative angles of attack and through the design angle of attack up to about 2°. At this point, however, the slope becomes positive which is an undesirable characteristic from an aircraft stability point of view.

Figure 3.10 shows a comparison between the computational and simulation results of the C_p distributions around the airfoil for several angles of attack. At all of the angles shown, the experimental data match the computational predictions quite well, although there is a slight offset in the pressure values on the order of ΔC_p = 0.03 - 0.05. For all of the cases, the pressure distributions over the suction slot and trailing-edge regions appear to be accurately modeled by the simulation. The oscillations which are present in the computational data near the suction slot were not captured in the experiment because no pressure taps could be placed in the suction region. Due to the limited number of pressure taps which were built into the airfoil, some error in the computation of lift and pitching moment is to be expected.

3.2.2 Comparison Between Configurations

In order to understand the effects of suction level on the performance of the airfoil, polars were also collected at several different suction levels. Figure 3.11 shows the full airfoil lift, drag, and moment polars for the no-suction baseline case, an 83% of full power (50 Hz) suction case, and a full-power (60 Hz) suction case. From Figure 3.11, it can be noted that the lift curve has been shifted towards higher C_l for both the 83% and 100% power cases. Although the changes in the lift curve with suction level are small, the shift between the no suction and the 83% case is on the same order of magnitude as the shift between the 83% case and the 100% case for α up to 1° , indicating that increasing the suction level thins the boundary layer and effectively adds camber to the airfoil. It can also be noted that the shift in lift curve slope which has been previously discussed for the no-suction case which occurs at $\alpha = 4^\circ$ is no longer present. This is most likely due to the fact that the suction is able to keep the flow fully attached to the airfoil trailing edge as the angle of attack is increased. As a result, the suction-enabled airfoil reaches a $C_{l,max}$ value which is roughly 0.1 higher than the no-suction case. After stall occurs, the suction and no-suction data points can be seen to follow the same path. The suction and no suction lift slopes as the angle of attack becomes more negative can also be seen

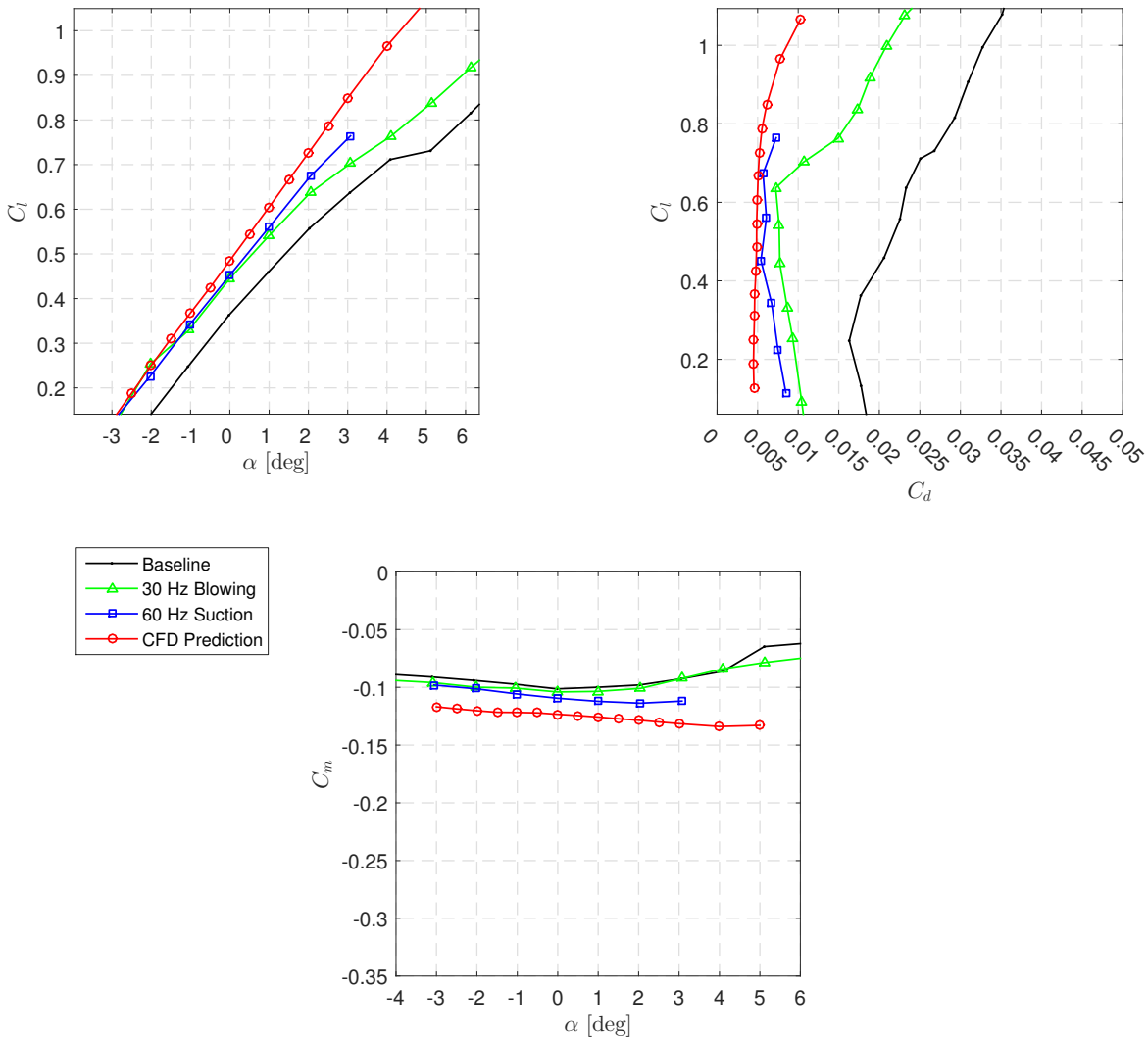

Figure 3.9: Performance of suction-enabled airfoil predicted from computational simulations at $M_\infty = 0.18$, along with experimental measurements with suction and blowing.

to converge to the same path. Due to an increase in attached flow across the upper surface, the suction-enabled airfoil experiences negative stall at the same angle at which the baseline airfoil does.

As before, the largest difference between cases can be noted in a comparison of drag. Comparing the 83% case to the no-suction case, the decrease in drag is between a ΔC_d of 0.01 and 0.02. Increasing the suction level to 100% further reduced the drag coefficient by a ΔC_d of 0.0025. It can also be noted that the shape of the drag bucket is relatively preserved between the different suction level cases. The shape of the drag bucket for the no-suction case is much less symmetric than the other two cases, however. The drag values for the positive angles of attack are much higher than those for the negative angles. This difference in C_d again can be attributed to the fact that the flow over

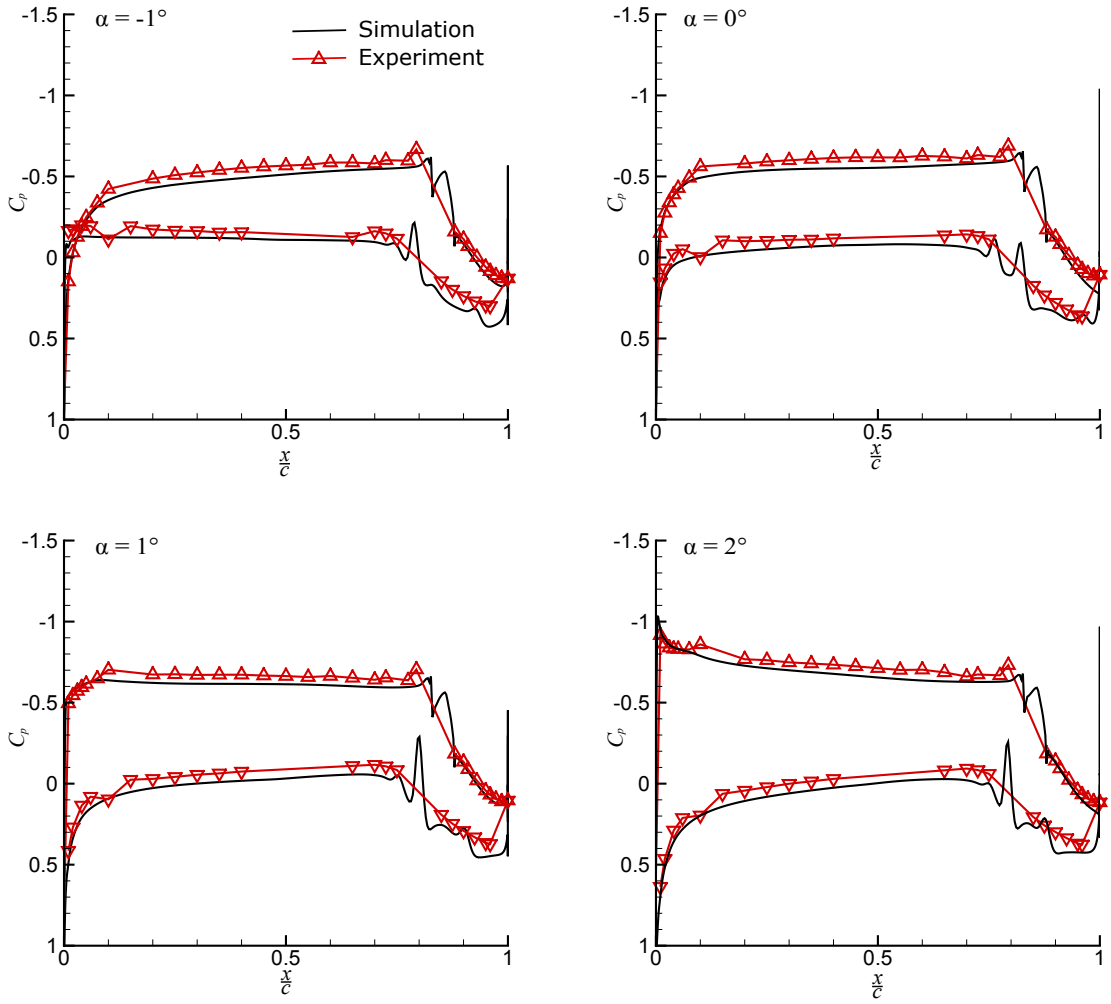

Figure 3.10: Airfoil C_p distributions from computational simulations at $M_\infty = 0.18$ and experimental measurements.

the trailing edge region was most likely separated without the presence of suction to keep it attached as the angle of attack was increased.

A comparison of the airfoil moment coefficients is also shown in Figure 3.11. The same trend can be noticed that for the negative angles of attack there is no discernible difference between the suction and no-suction cases, while there is a large difference for the positive angles of attack. As the angle of attack is increased, the pitching moment for the baseline airfoil becomes much more positive than the pitching moment of either of the suction cases. As the airfoil stalls, however, the suction and no-suction cases are again associated with consistent values. Only a small difference can be noted between the two different suction level cases, as the pitching moment curve is shifted slightly in the negative direction when increasing the suction from 83% to 100%.

Overall, the aerodynamic performance of the airfoil section is greatly improved when suction is applied. The improvement over the baseline case is seen to be greater as the angle of attack of the airfoil is increased. This observation is due to the fact that without suction, the flow across the trailing-edge region of the airfoil will separate and drastically deteriorate the airfoil's performance. As discussed, these trends can be observed in the lift, drag, and moment data which were collected during the experiment. While the addition of suction does improve the lift of the airfoil, the primary improvement is seen in the reduction of drag. This impact on the performance is a desirable characteristic for the propulsive wing section, because this indicates that were the airfoil suction system to fail when implemented on the aircraft, the vehicle would not see a large loss of lift. While large drag penalties would arise in such an instance, it would not lead to a direct catastrophic failure in the operation of the aircraft.

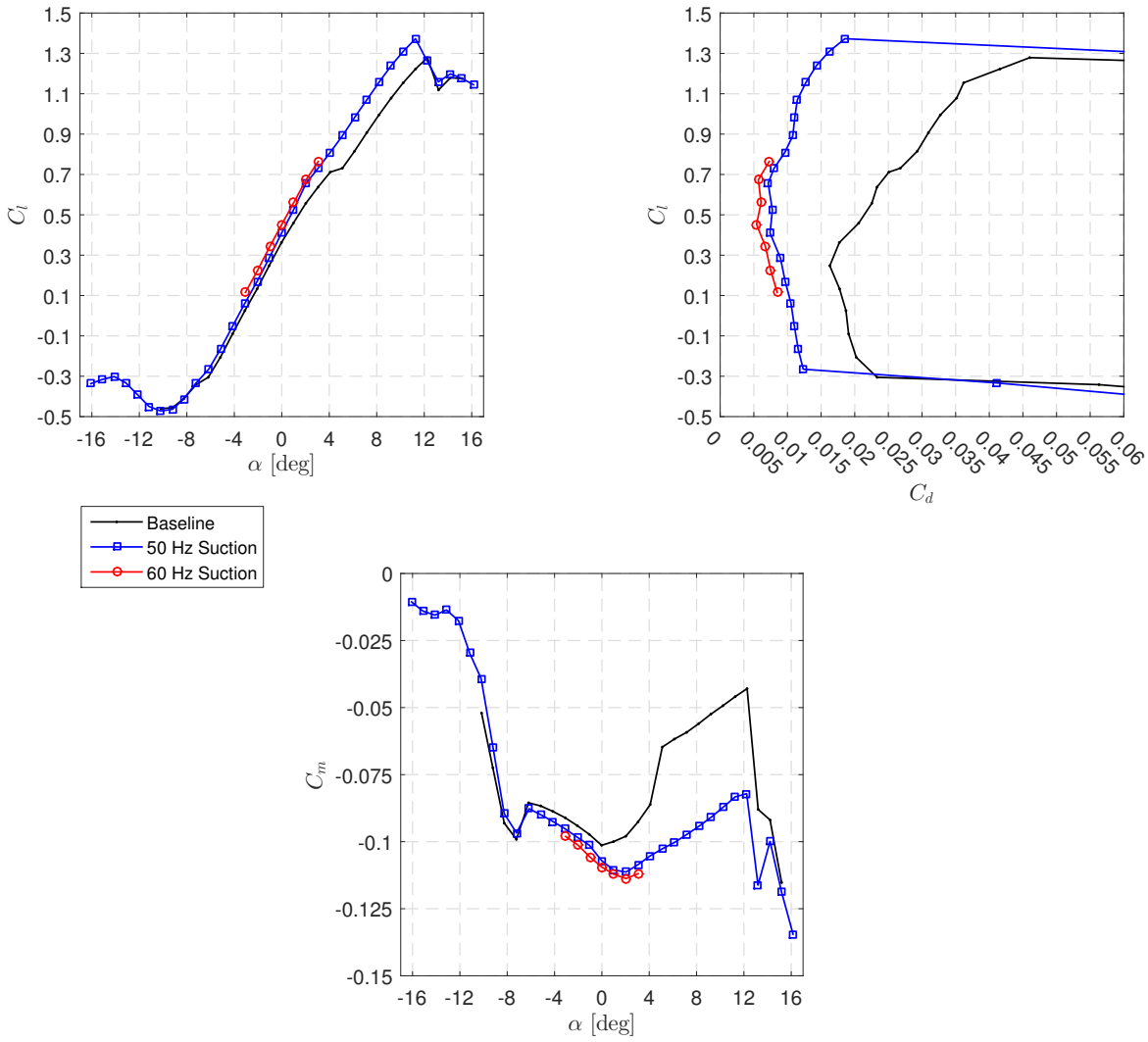

Figure 3.11: Performance of the airfoil at several suction levels.

As discussed in Section 2.2.2, the airfoil suction system had the ability to be equipped with one of three different suction-slot cover plates. As discussed, these were a three-slotted plate, a five-slotted plate, and a porous plate. A comparison in the lift and drag produced by the airfoil configured with these different suction plates is shown in Figure 3.12. All of the suction cases shown in the figure were taken at 83% full power (50 Hz), while the blowing cases were of varied power levels as indicated by the figure legend. All three of the blowing cases were performed with the five-slotted suction plate installed on the airfoil model, with half of the blowing slot covered in order to accommodate the capabilities of the centrifugal blower. All of the data points shown in the figure were taken at $\alpha = 0^{\circ}$, which was the design angle of attack of the airfoil.

Comparing the lift between the different cases shown yields several observations. First, all of the suction and blowing cases exhibit a gain in lift over the baseline case, where no suction was used. The smallest gain corresponded to the suction case with the five-slot cover plate, with a ΔC_l of 0.05. The rest of the suction and blowing cases exhibited ΔC_l's between 0.1 and 0.15 over the baseline case. When comparing between the three different cover plates, the three-slotted plate and the porous plate attained C_l values of 0.49, while the five-slotted plate only attained a C_l value of 0.41. The three different blowing cases also show a trend of increasing lift with increasing blowing level, with the highest C_l value of all the cases attained by the 50 Hz blowing case with a value of 0.525. It can also be noted that there is a greater increase in lift between the 30 Hz and 40 Hz blowing cases than there is between the 40 Hz and 50 Hz cases. This is likely due to a saturation effect caused by the blower approaching its capacity to supply increased suction and blowing. Finally, it can be observed that higher values of C_l can be attained when the airfoil is performing as designed with suction and blowing, as opposed to the suction only cases.

Values of the drag coefficient are also shown for comparison between the cases. Again, all of the suction and blowing cases exhibited large reductions in drag over the baseline, no-suction case. The porous plate suction case exhibited the lowest drag, with a C_d of 0.00434, corresponding to a ΔC_d of 0.0134 over the baseline case. The three-slot plate produced the next-lowest drag value, with a C_d of 0.00624. The five-slot suction case as well as the 30 Hz and 40 Hz blowing cases all exhibited C_d values between 0.007 and 0.008. It is interesting to note that the highest level of blowing (50 Hz) produced the lowest decrease in drag over the baseline, with a C_d value of 0.01256, which also corresponded to the highest value of lift as previously discussed. It is also important to note that these drag values correspond to slightly different values of C_l due to the increased lift which was also supplied by the suction and blowing system.

The overall results from comparing these different configurations with different levels of suction and blowing indicate a clear advantage in providing both suction and blowing to the airfoil. It can also be noted that the porous plate suction slot cover provided the best lift and drag performance when compared to all of the other cases. It is expected

that if the blowing cases were ran with the porous plate as well, the drag values attained would be comparable to the suction-only case.

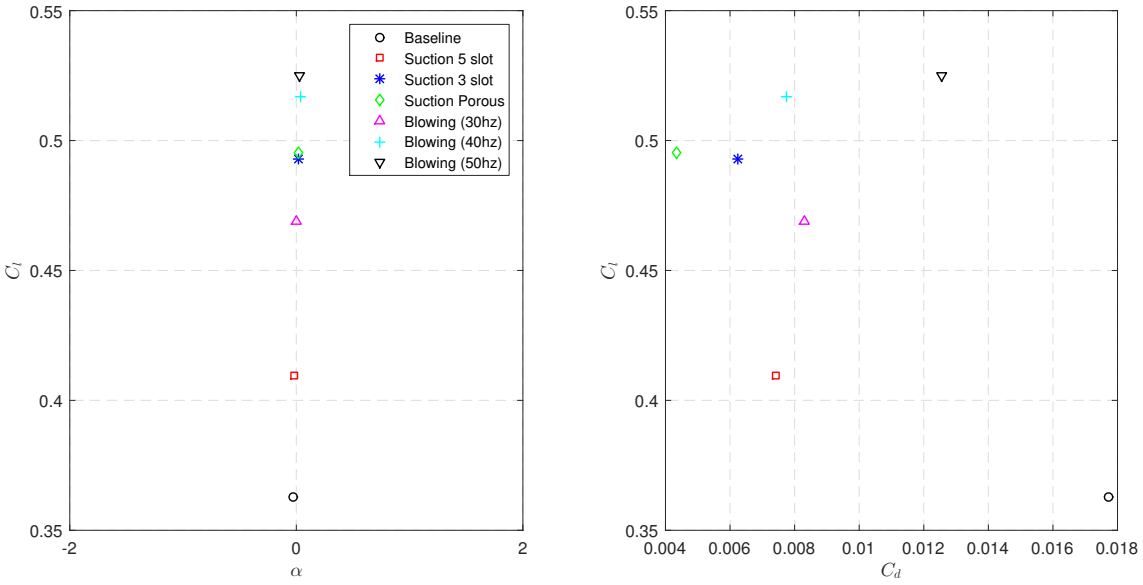

Figure 3.12: A comparison of the airfoil lift and drag at $\alpha = 0^\circ$ for various airfoil configurations.

3.2.3 Wake Comparisons

Measurements of the airfoil wake at the center span position were taken to calculate the drag of the airfoil section using momentum deficit theory. While this calculation was the primary purpose for the wake measurements, it is also of interest to compare the wakes produced by the airfoil between different suction and blowing levels. Figure 3.13 shows several airfoil wakes alongside a baseline no-suction or blowing wake shown in black. The first observation that should be made is that the wake for the baseline case is much wider than the wakes for any of the suction and blowing cases. This large wake is again due to the fact that the flow over the trailing edge region is likely separated when no suction is present. It is also interesting to note that the wake is deflected downwards, towards the lower surface of the airfoil for all of the suction and blowing cases when compared to the baseline case. This wake deflection could be interpreted as evidence of a circulation effect which is also consistent with the previous observation that increasing the suction level had a cambering effect on the airfoil [29].

From Figure 3.13, it can also be noted that the magnitude of the total pressure deficit between all of the cases is nearly identical at the center of the wake. This trend would be expected to be true for the baseline and suction cases. For the blowing cases, however, one would expect that some of the total pressure deficit would be recovered. The change in lift between these cases could partially account for this observation. There is, however, a small difference in

the peak values of ΔP_o between the three blowing cases. As the blowing level was increased from 50% full power to 83% full power, ΔP_o does decrease slightly. The fact that this decrease is so small is likely due to the blower's inability to supply adequate blowing power to the airfoil model. If the model were run with the design blowing velocity of 25% of the freestream velocity, it is expected that the reduction in total pressure deficit would be much larger.

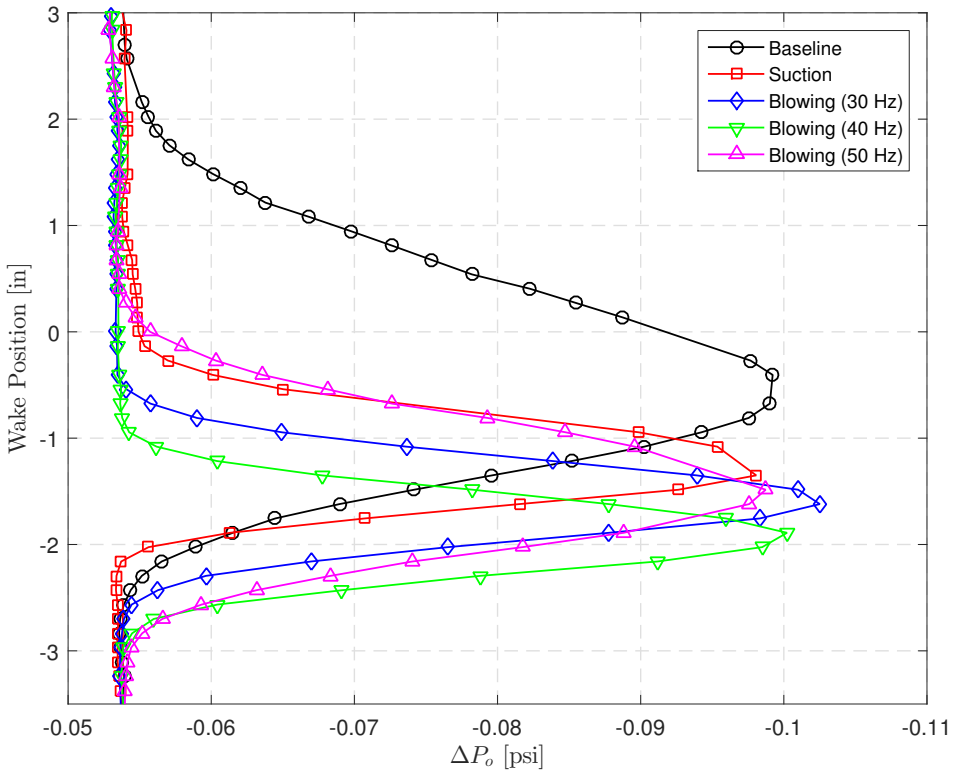

Figure 3.13: A comparison of the airfoil wake for various suction and blowing settings.

3.2.4 C_p Comparisons

A comparison of the airfoil pressure distributions for the same suction and blowing cases as the wake comparison is shown in Figure 3.14. It can be clearly observed that there is a significant difference between the trailing edge pressure distributions for the suction and blowing cases. This difference is due to the fact that a separate trailing edge region was manufactured for the suction and blowing case. No pressure taps could be located in the region of the airfoil consumed by the suction slot. As a result, the pressure distributions appear to be slightly shorter for the blowing cases when compared to the suction cases.

From Figure 3.14, it can be noted that the magnitude in the difference between the upper and lower surface pressure values increases when suction is applied, and further increases as blowing is applied and the blowing level is increased. There is little difference between the 66% (40 Hz) blowing case and the 83% blowing case, however, which

is another indication that the blower was approaching its limits and was unable to further increase the blowing level. This increase in the magnitude of the pressure difference between the upper and lower surfaces is also indicative of a circulation effect which was seen to increase the lift of the airfoil as blowing was applied.

By observing the baseline no-suction case shown in black, it can be seen that there is plateau in the value of C_p at the position which corresponds to the location of the suction slot. This observation serves to support the previous observations in the airfoil performance characteristics which suggested that the flow over the pressure recovery region was not as well-behaved as it was when suction was applied. From Figure 3.14, it can also be noted that the pressure distributions for the suction-enabled cases exhibit larger increases in pressure across the trailing-edge region. The contour of C_p values also have no plateau, and the pressure is recovered to a higher value than the baseline case.

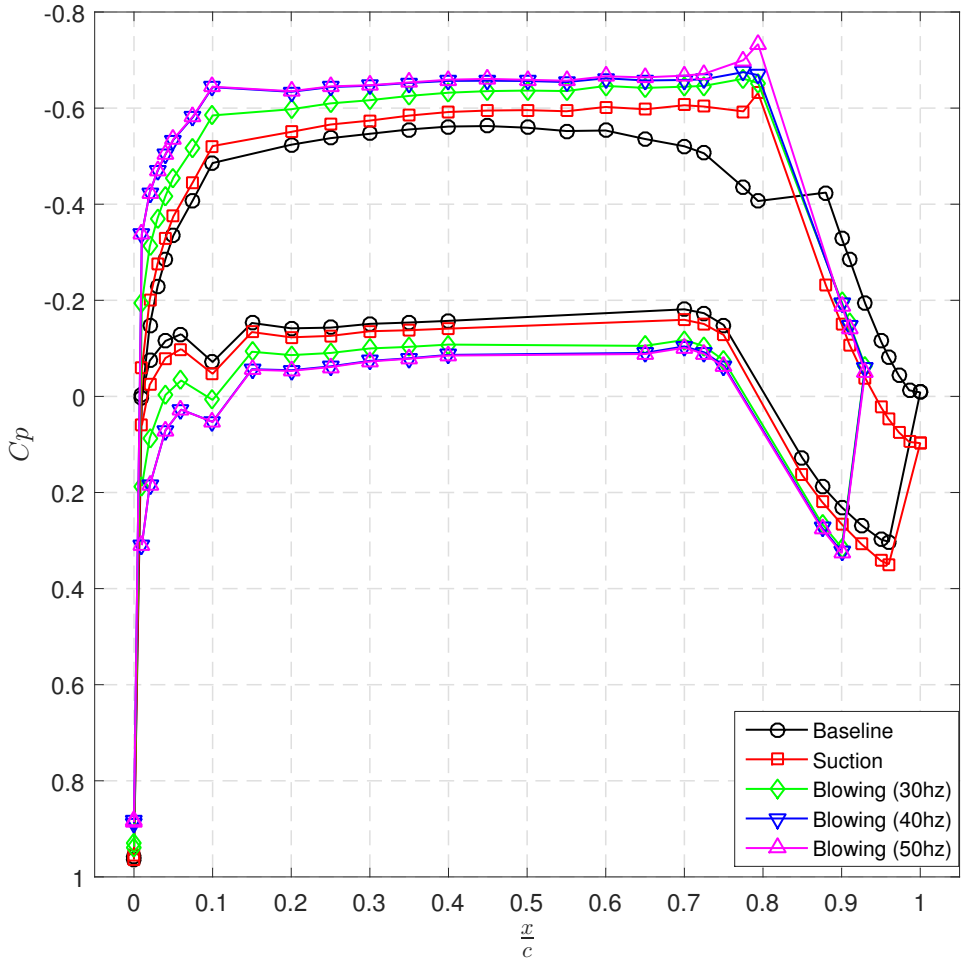

Figure 3.14: A comparison of the airfoil pressure distribution for various suction and blowing settings at $\alpha = 0°$.

A comparison of the C_p distributions was also made for an increasing angle of attack as shown for the baseline case in Figure 3.15, for the suction-only case in Figure 3.16, and for the suction and blowing case in Figure 3.17. For

convenience in determining trends, each of these graphs is split into positive angles of attack and negative angles of attack. Both the positive and negative angle of attack subplots contain the $\alpha = 0$ case for comparison.

The sweep through angles of attack for the baseline case as shown in Figure 3.15 show that the same plateau in C_p occurs over the suction region for all of the angles of attack investigated. These pressure distributions serve to reinforce the observation that the performance of the airfoil is separation-limited as the angle of attack is increased without the application of suction. It can also be noted from the negative angle of attack sweep that the plateau in C_p values across the trailing edge is less prominent, indicating that the separation limitations are more prominent at positive angles of attack.

The suction only airfoil pressure distributions for the same angles of attack are shown in Figure 3.16. The key difference between these distributions and the baseline distributions is that the pressure recovery region is now well behaved. The distributions indicate that the flow over the trailing edge region is attached for all of the angles of attack shown. A second difference is that the values of C_p across the upper surface of the airfoil are shifted towards the negative C_p direction, creating a greater pressure difference between the upper and lower surfaces. This phenomena was previously discussed for the $\alpha = 0^\circ$ case, but can be seen to also be true for the nonzero angles of attack which are shown in the figure as well. The pressure at the trailing edge tap of the upper surface can be seen to recover to a value slightly greater than $C_p = 0$, where the pressure was recovered to a value slightly lower than zero for the baseline airfoil case. A small suction peak in the C_p values on the upper surface can also be seen to occur directly before the suction slot region, which was also observed in the computational simulations as a result of the application of suction. This peak appears to be slightly more exaggerated for the negative angle of attack cases.

The pressure distributions for the same angles of attack are again shown in Figure 3.17 for the airfoil with suction and blowing. While a direct comparison between the suction-only and the suction-and-blowing case cannot be made due to the face that the blowing cases could not be run at the same power level of the centrifugal blower, several key observations can still be made. The suction peak induced by the suction slot seems to be much less pronounced for these cases, although this is likely due to the face that the blower is running at half-power as opposed to the full-power suction cases. A second result of this is that the pressure at the trailing edge tap recovers to a value slightly lower than 0. While the pressure distributions indicate that the airfoil was not performing at its full capacity, improvements over the baseline no-suction case can still be seen for the blowing case even at half-power, which indicates that proper suction and blowing would allow the airfoil to perform as designed.

3.2.5 Flow Visualization Results

The final aspect of the experimental tests which were performed on the designed Griffith/Goldschmied type airfoil was a series of surface oil flow visualization tests. The results of the flow visualization are shown in Figure 3.18 for

angles of attack of $0^\circ, 3^\circ, 4^\circ$, and 5°. Only the center portion of the airfoil surface which was spanned by the suction slot is shown in each of the pictures. The suction slot is visible from $\frac{x}{c} = 0.825$ to $\frac{x}{c} = 0.875$.

From the 0° case shown in sub-figure (a), the boundary-layer flow can be seen to remain laminar until the suction slot. After the suction slot, the flow remains attached and has transitioned to a turbulent boundary layer. The transition process is here induced by the presence of the suction slot. These transition characteristics are unique to the airfoil at a Mach number of 0.18 as tested in the wind tunnel. For the design Mach number of 0.7, transition was predicted to occur on the upper surface at the $\frac{x}{c} = 0.57$ location and is induced by natural transition processes as observed from the simulations [18].

For the higher angle-of-attack cases which are shown in sub-plots (b) through (c), the flow can also be seen to remain laminar until the suction slot. As the angle of attack is increased from 0°, the oil droplets aft of the suction slot region become less smeared, indicating a decrease in the shear stress at the wall. The 5° case shown in sub-plot (d) exhibits several flow features which are not evident in the lower angle of attack cases. First, the presence of a laminar separation bubble can be noted at the leading edge of the airfoil. Second, flow patterns left in the oil aft of the suction slot indicate that there are several regions of reversed flow.

The overall results of the flow visualization indicate that the suction slot is effective in promoting laminar flow over the foreword portion of the airfoil, as well as keeping the flow attached aft of the suction slot. These observations lead to the same conclusions about flow attachment which were previously discussed in the airfoil performance and pressure distribution results sections.

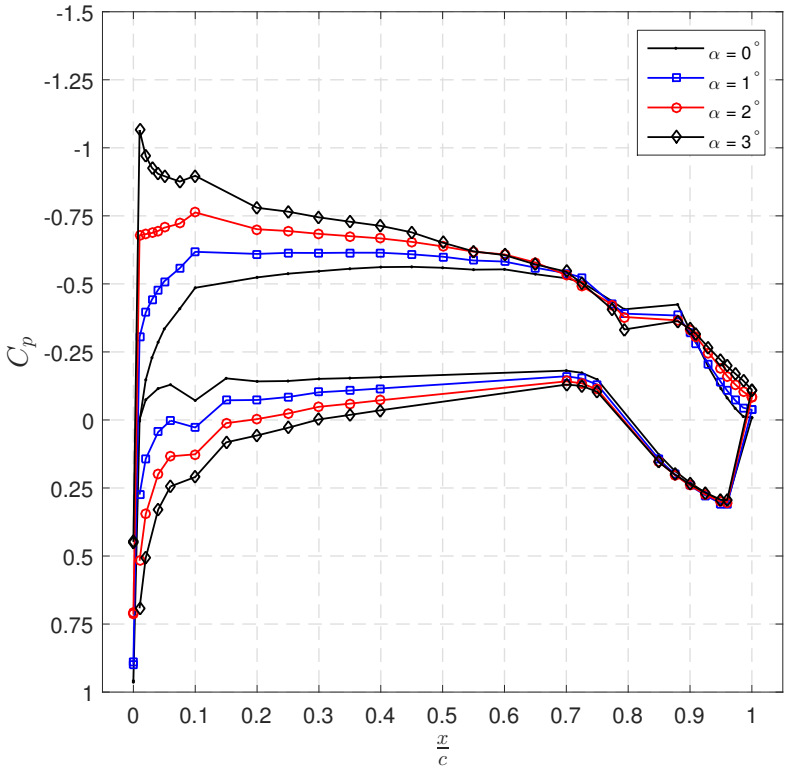

(a)

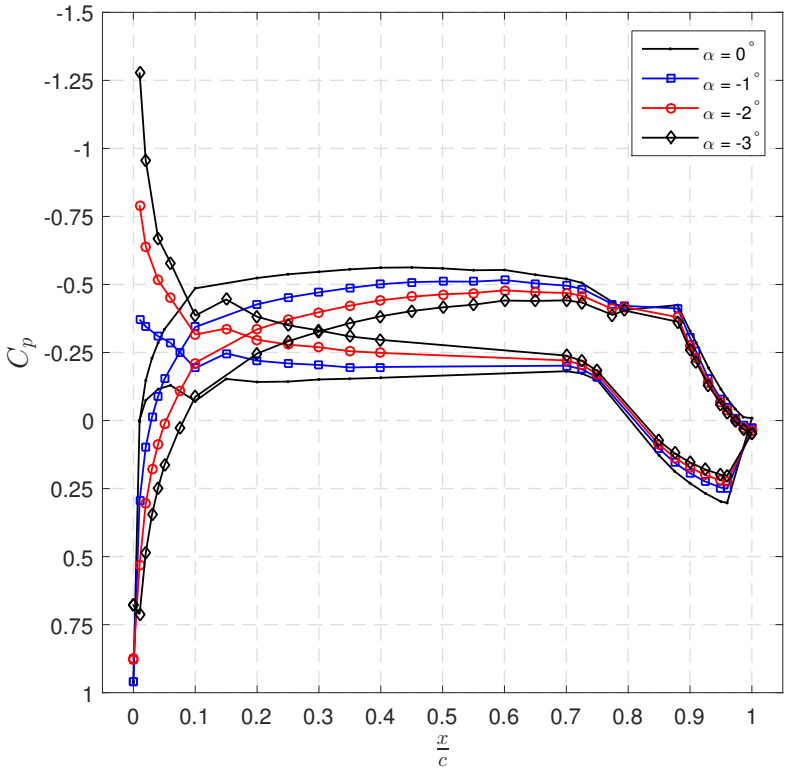

(b)

Figure 3.15: A comparison of C_p curves of the baseline airfoil for (a) positive α and (b) negative α.

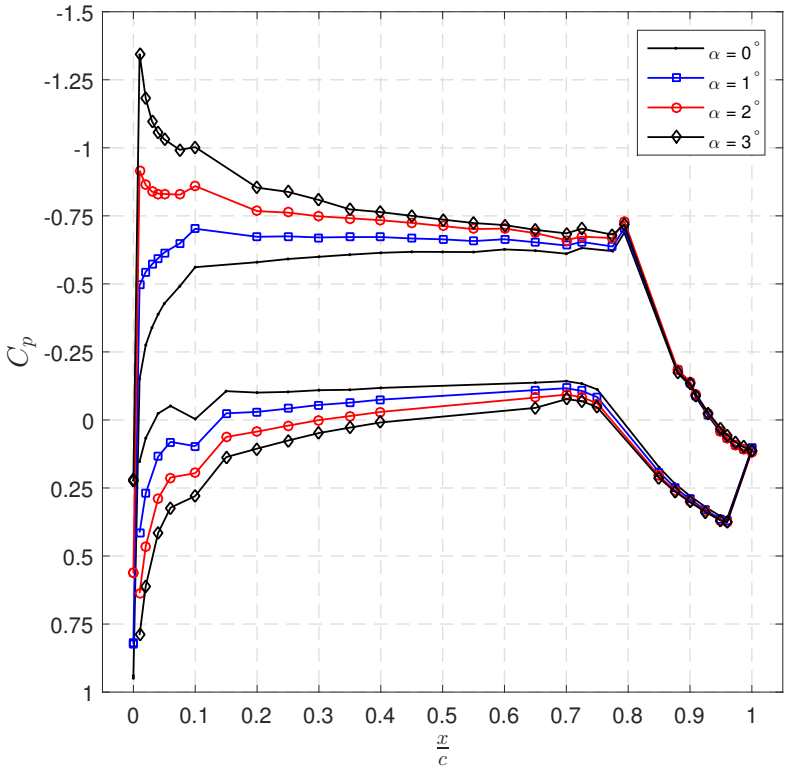

(a)

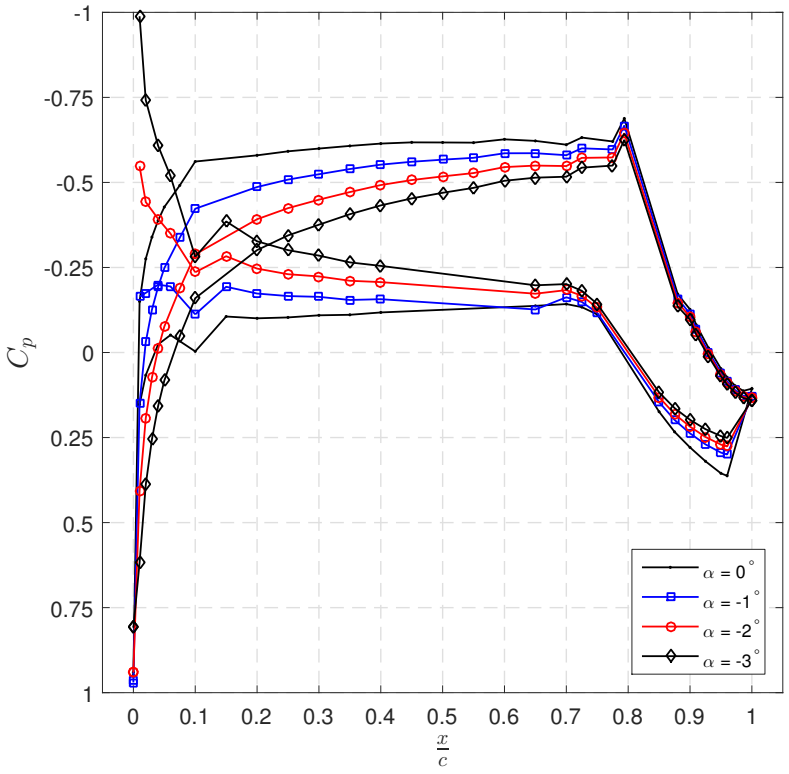

(b)

Figure 3.16: A comparison of C_p curves of the airfoil with suction for (a) positive α and (b) negative α.

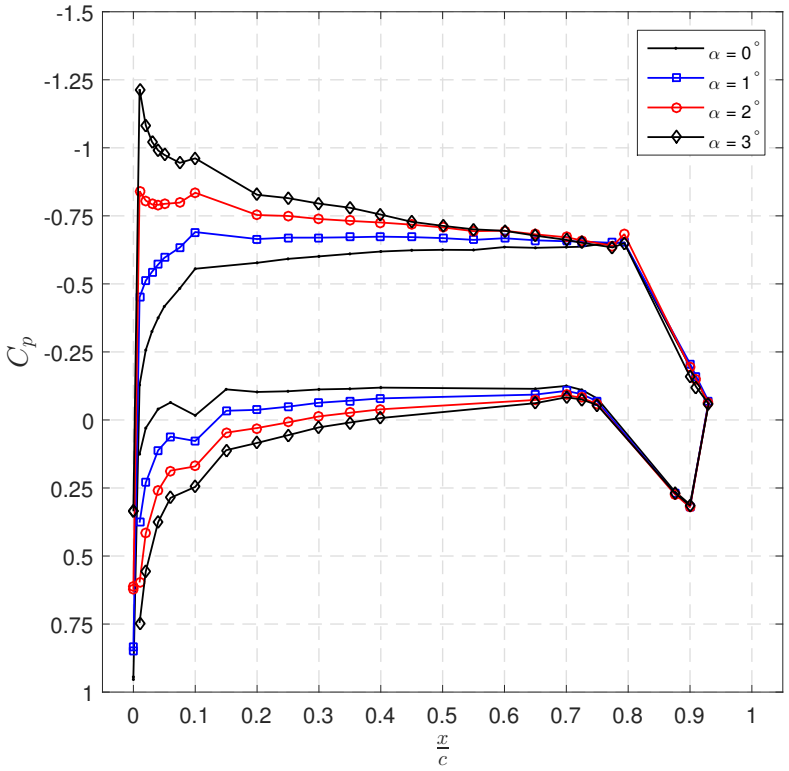

(a)

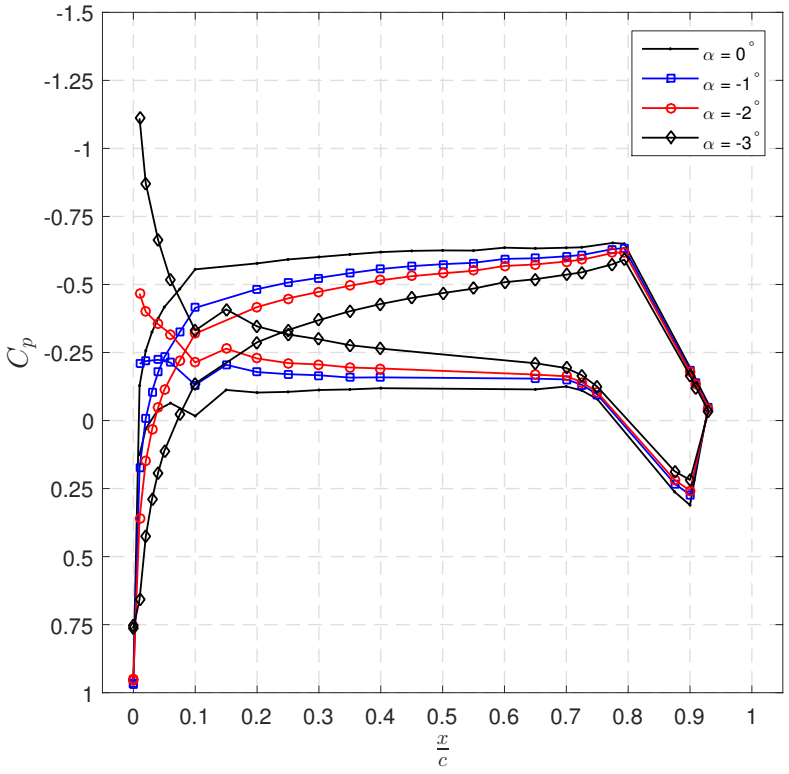

(b)

Figure 3.17: A comparison of C_p curves of the airfoil with suction and blowing for (a) positive α and (b) negative α.

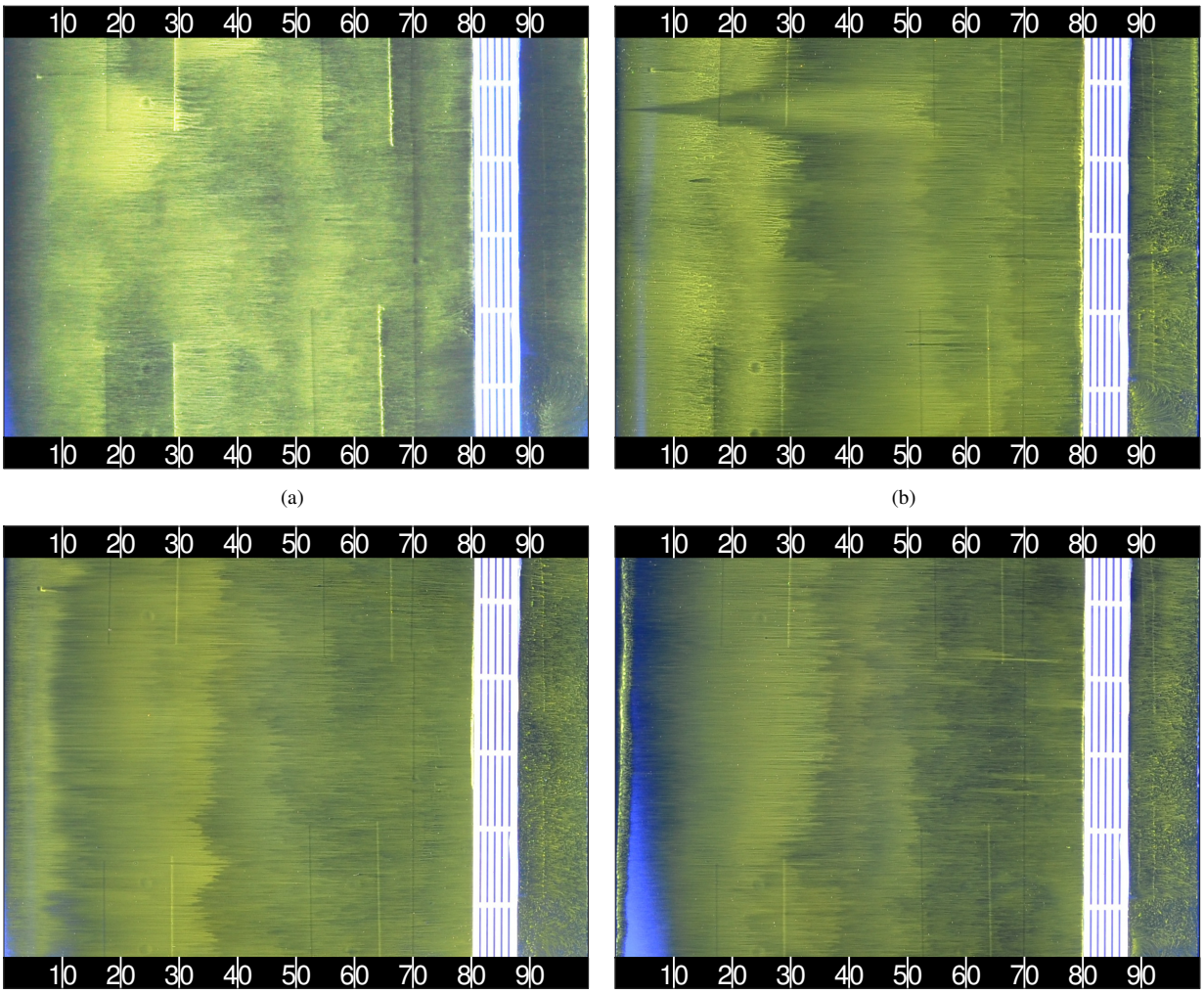

Figure 3.18: Surface oil flow visualization of airfoil upper surface at (a) $\alpha = 0°$, (b) $\alpha = 3°$, (c) $\alpha = 4°$, (d) $\alpha = 5°$.

Chapter 4

Conclusions

4.1 Summary of the NASA LEARN Project

The work which has been presented in this thesis was performed in support of a NASA LEARN project which aimed to develop a propulsive wing airfoil section. The developed wing section could be utilized on a future-generation high efficiency aircraft. The aspects of this study which were not a part of the work presented in this thesis, including the design of the propulsive wing section and a systems level analysis of the aircraft, are discussed in Ref. 18. A brief summary of these aspects of the LEARN study are discussed here.

During the airfoil design portion of the study, an ultra-low drag transonic airfoil section was designed. The airfoil used a suction-based pressure recovery system which enabled extended runs of natural laminar flow, pressure thrust, and wake filling from the suction mass flow ejected out of the trailing edge of the airfoil section. This airfoil section was designed based on the Griffith/Goldschmied propulsive airfoil concept, and aimed to extend the same principles of pressure thrust and wake filling to a higher, transonic Mach number. The inverse airfoil design tool Profoil was used in conjunction with the OVERFLOW RANS solver in order to converge upon the final geometry. The designed airfoil was 12.48% thick, which alleviated the issue of the low critical Mach number typically associated with Griffith/Goldschmied sections. With a suction velocity of $V/V_\infty = 6.5\%$, the airfoil produces a $C_l = 0.86$ at $\alpha = 0^\circ$ and maintains laminar flow to 57% chord on the upper surface and 45% on the lower surface. At this condition the airfoil produced C_d = 0.0052 (62% reduction over baseline) with just suction, and C_d = -0.0004 with suction and trailing-edge blowing. Results from the computational design of the airfoil section were extremely promising, indicating that the pressure drag negation concept typically associated with thicker Griffith/Goldschmied sections can be applied to thinner, higher Mach number airfoil sections.

To perform the systems analysis, the Boeing N+4 SUGAR Refined aircraft was selected for use as a baseline future-generation aircraft for comparison. The SUGAR Refined aircraft was modeled using the AVID ACS interdisciplinary aircraft synthesis tool. Performance of the aircraft as measured by the required block fuel per seat mile for a 900 nautical mile mission was compared between the baseline case and a case with the newly designed propulsive airfoil section utilized on the inner 70% of the SUGAR Refined wing span. Data from the cross-flow fan test described in

this thesis was used to estimate the power requirements of implementing the propulsive airfoil section. Results from the analysis indicated that an 11.8% reduction in block fuel per seat mile could be attained by implementing the new wing section on the advanced commercial transport aircraft concept. The results from the systems analysis are slightly optimistic, since it was assumed that the flaps could be replaced by the cross-flow fan (since they have been suggested for use in powered lift), and the structural weight of the fan support system could not be estimated at the time of the study. Even if an additional 10% were added to the weight of the wing, however, an 11.4% reduction in block fuel per seat mile could still be attained. These results show that the benefits gained by the decrease in drag produced by the newly designed airfoil section far outweigh the power required to run the system.

4.2 Summary of the Performed Experiments

In support of the airfoil design process as well as the systems analysis aspects of the NASA LEARN project, several wind tunnel tests were performed at the University of Illinois. These experiments included a low-speed wind tunnel test to validate the design tools utilized during the airfoil design portion of the study and to verify the pressure thrust concept, as well as a transonic wind tunnel test of an embedded cross-flow fan to produce data which could be used in the systems analysis. The key aspects of each of these wind tunnel test are briefly summarized in this section.

The transonic testing of the embedded cross-flow fan was performed in a modified supersonic wind tunnel with a 5"×5" test section. The cross-flow fan was embedded in the wall of the wind tunnel, and an SLA 3D printed part was used to complete the fan housing as well as to simulate the trailing edge of the newly designed airfoil section. Measurements were taken of the mechanical power required to run the fan at 5500 and 7000 rpm over a range of freestream Mach numbers of 0.4–0.7. These measurements were scaled for use in the systems analysis. Measurements of the total pressure, total temperature, and velocity in the exit duct of the fan were also taken to quantify the mass flow characteristics of the cross-flow fan. Finally, measurements of the pressure distribution over the representative trailing-edge expansion surface piece were also acquired to investigate the effects of the suction produced by the cross-flow fan on flow attachment and static pressure rise.

The low-speed wind tunnel test was performed in the 2.8'×4' open return wind tunnel at UIUC on an 18"-chord airfoil model. The suction slot of the airfoil was integrated across the center 14" of the span, and the suction plenum was routed to the top of the airfoil model where it interfaced with the centrifugal blower system which was used to supply the suction and blowing for the airfoil model during testing. The model was constructed with an interchangeable trailing edge, allowing it to be tested in a suction-only configuration, as well as in a suction and blowing configuration. Measurements were taken of the pressure distribution around the airfoil as well as the total pressure in the wake of the

airfoil to compute the lift and drag performance for a variety of angles of attack. All of the airfoil tests were performed at a Reynolds number of 1.8×10^6 and a Mach number of 0.18.

4.3 Conclusions from the Performed Experiments

4.3.1 Cross-flow Fan Test Conclusions

Experimental testing of the embedded cross-flow fan displayed that such a system can be used to provide the desired suction-based pressure recovery required by the designed propulsive airfoil in a transonic flow. Pressure tap measurements indicate that the fan was able to aid in pressure recovery. The fan-off pressure tap measurements for all Mach number cases indicated that the flow was detached over the expansion surface, while for all of the fan-on cases, the flow had become attached over the expansion surface. In addition to aiding in flow attachment, a discrete static pressure rise was produced by the cross-flow fan over the expansion surface aft of the suction slot. This static pressure rise over the representative trailing-edge region is important for the Griffith/Goldschmied concept to function, as it is the driving factor for the pressure thrust produced by the airfoil section.

Measurements of the total temperature, total pressure, and velocity in the exit duct of the cross-flow fan were used to compute the mass flow rate of the fan, as well as to compute the flow coefficient for scaling between the test case and the aircraft model used for the systems analysis. Results from this flow coefficient scaling indicated that the fan tip speed required to run the propulsive airfoil section on the SUGAR Refined aircraft was 76.8 ft/s, which is a 10% reduction from the 85.4 ft/s tip speed achieved in the experiment. Measurements of the velocity in the exit duct and computed values of the velocity at the fan inlet were used to compute the suction and blowing velocity ratios achieved in experiment. The achieved velocity ratios were near $\frac{V_{suction}}{V_\infty} = 0.11$ and $\frac{V_{blowing}}{V_\infty} = 0.35$ for all of the Mach number cases investigated. These values exceeded the required values of $\frac{V_{suction}}{V_\infty} = 0.0625$ and $\frac{V_{blowing}}{V_\infty} = 0.25$ as determined by the computational design process. This analysis confirmed that the cross-flow fan would be capable of supplying the required suction and blowing to power the newly designed propulsive wing section.

Direct measurements of mechanical power required by the fan were were used to compute a power coefficient which could be used to scale the required mechanical power from the experimental scale to the aircraft scale. This power coefficient also took into account the difference in density between the experimental and aircraft flight environments. Results from the power scaling indicated a mechanical power requirement of 187 kW to run a cross-flow fan in both wings of the Boeing SUGAR Refined baseline aircraft. When an 80% electrical efficiency was taken into account, this power requirement translated to 234.5 kW of electrical power to be provided by the aircraft power plants. Through the inclusion of four integrated drive generators, this power value can easily be obtained by the SUGAR Refined aircraft.

4.3.2 Airfoil Test Conclusions

Results from the low-speed wind tunnel test of the designed airfoil showed promise for the propulsive wing concept and provided reassurance that the tools used during the airfoil design process had accurately predicted the performance of the suction-enabled airfoil section. A comparison of the lift, drag, and moment polars between computational results for the same Mach and Reynolds numbers showed general good agreement, with a slightly lower lift curve slope for the experimental case. A comparison between predicted and measured airfoil pressure distributions also indicated that that the pressure distribution around the airfoil was accurately predicted, which was particularly important to ensure that the effects of the suction on the pressure distribution were being accurately modeled.

Comparisons were also made between several different levels of suction, ranging from no suction to full-powered suction. Results from this comparison indicate that there is only a slight increase in lift when suction is applied to the airfoil over the no-suction case, while there is a large reduction in drag with the application of suction. The quarter-chord pitching moment can also be seen to become slightly more negative as the suction level was increased. These characteristics are desirable, as they indicate a fault-tolerant behavior for the airfoil section. If the suction system were to become disabled during flight due to failure of an electrical or mechanical system, manageable drag penalties would occur without a major loss in lift.

Comparisons were also made between the drag and lift produced at zero angle of attack for several different suction plenum covers. The lowest drag by far was produced by the porous plate suction plenum cover, and the highest drag was produced by the five-slotted suction plenum cover. The three-slotted suction plenum cover drag value was between these two.

Lift, drag, pressure distributions, and airfoil wakes were also compared between different power levels of the suction-and-blowing enabled airfoil. Results from the comparison of lift indicated that increased levels of blowing led to increases in the lift coefficient. The blowing level did not appear to have a drastic effect on reducing drag, however. This is likely due to the fact that the full-powered blowing level could not be obtained during the experiment. This could also be a result of a change in drag due to the increased lift produced by the blowing. A comparison of the airfoil wakes for the different levels of suction and blowing indicate that the wake becomes increasingly deflected downwards as the suction and blowing level is increased. This observation is indicative of a circulation control effect which may play a role in the observed increase in lift as suction/blowing levels are increased. The wake deficit region is also narrowed with the application of suction and blowing, which plays a role in the reduction of drag. The comparison of pressure distributions for different levels of suction/blowing show an increased pressure difference between the upper and lower surfaces of the airfoil as the suction/blowing level is increased. This also supports the observation that a circulation control effect is occurring.

Results from the oil surface flow visualization indicate that the suction system is able to maintain laminar flow from the leading edge up until the suction slot for the investigated angles of attack between 0° and 5°. After the suction slot, the flow transitions to turbulent, with slower flow velocities as the angle of attack is increased. The presence of a laminar separation bubble can also be noted at 4°.

All of the results which have been discussed also serve to indicate that the performance of the airfoil section is highly separation limited in the absence of applied suction. This observation is no surprise, as the pressure recovery over short trailing-edge region of the airfoil is completely reliant on the presence of suction. A comparison of the pressure distributions through an angle-of-attack range of -3° to 3° for the baseline case and the suction-enabled case also supports this observation.

4.4 Recommendations and Future Work

The author would recommend several things for future researchers who aim to experimentally test cross-flow fan performance. The most challenging aspect of the experimental design was selecting a motor which could meet the power requirements of the cross-flow fan. The main reason for this was a lack of data on cross-flow fan power requirements in high-speed flows. For this purpose, the power data which was collected during the experiment is presented in Appendix A. It is also important when selecting a motor to ensure that the motor can supply the required power over the full range of desired rotational speeds.

An additional aspect of the study which was planned but not performed due to time constraints was the collection of particle image velocimetry data over the cross-flow fan inlet and expansion surface region. These data would have been very useful in verifying that the housing configuration was properly designed, and that there were no regions of reversed flow present near the fan inlet. These data would also be useful to better characterize the flow features which are present during the operation of a cross-flow fan in transonic flow.

It is also recommended that care be taken when designing a suction system which utilizes suction sources external to an airfoil model. The performance of the suction system was limited due to the small diameter of the holes in the top of the airfoil model which interfaced with the blower system. The small holes created too great of a pressure rise for the centrifugal blower to operate at full power. The author would suggest that the suction system be interfaced in such a way that there are limited to no restrictions in the tubing, and that the suction is supplied through both ends of the airfoil to achieve a more even distribution of suction over the slot. A non-intrusive method of measuring the suction mass flow should also be implemented to avoid the blockage created by a traditional mass flow meter.

Overall results from the airfoil design, transonic cross-flow fan testing, and systems level analysis show great promise for the proposed propulsive wing concept to meet the NASA N+3 aircraft efficiency goals. Future develop-

ment of this propulsive wing concept would require the design of a new suction-enabled laminar flow transonic airfoil with a higher design Mach number of 0.8 to ensure commercial viability. A validation of the selected airfoil design in a large-scale transonic wind tunnel experiment would also be necessary. Additionally, a new cross-flow fan housing will need to be designed for the airfoil concept and the capabilities of a cross-flow fan powered high-lift configuration should be evaluated. A final systems-level analysis would also be necessary using the experimental validation data in order to quantify the final fuel savings expected from this airfoil concept.

References

[1] Felder, J. L., Tong, M. T., and Chu, "Sensitivity of Mission Energy Consumption to Turboelectric Distributed Propulsion Design Assumptions on the N3-X Hybrid Wing Body Aircraft," AIAA Paper 2012-3701, 48th AIAA/ASME/SAE/ASEE Joint Propulsion Conference and Exhibit, Atlanta, GA, 2012.

[2] http://www.nasa.gov/content/the-double-bubble-d8 0/#.U96a5mM0B_6.

[3] Bradley, M. and Droney, C., "Subsonic Ultra Green Aircraft Research: Phase I Final Report," NASA/CR2011-216847, April 2011.

[4] Felder, J. L., Kim, H. D., and Brown, G., "An Examination of the Effect of Boundary Layer Ingestion on Turboelectric Distributed Propulsion Systems," AIAA Paper 2011-300, 49th AIAA Aerospace Sciences Meeting including the New Horizons Forum and Aerospace Exposition, Orlando, FL, 2011.

[5] Richards, E. J., S., W. W., and R., G. J., "Tests of a Griffith Aerofoil in the 13 ft x 9 ft Wind Tunnel Part 1, Part 2, Part 3, Part 4, Lift, Drag, Pitching Moments and Velocity Distributions," ARC R&M-2148 ARC-7464 ARC-7561 ARC-8054 ARC-8055, 1944.

[6] Goldschmied, F., "Fuselage Self-Propulsion by Static-Pressure Thrust: Wind-Tunnel Verification," AIAA Paper 87-2935, 1987.

[7] Goldschmied, F., "Airfoil Static-Pressure Thrust: Flight Test Verification," AIAA Paper 90-3286, 1990.

[8] Goldschmied, F., "Thick-Wing Spanloader All-Freighter: Design Concept for Tomorrow's Air Cargo," AIAA Paper 90-3198, 1990.

[9] Cella, U., Quagliarella, D., Donelli, R., and Imperatore, B., "Design and Test of the UW-5006 Transonic Natural-Laminar-Flow Wing," Journal of Aircraft, Vol. 47, No. 3, 2010, pp. 783-795.

[10] Sandercock, D. M. and Sanger, N. L., "Some Observations of the Effects of Radial Distortions on Rrformance of a Transonic Rotating Blade Row," NASA TN D-7824, 1974.

[11] Tamaki, T. and Nagano, S., "Effects Of Inlet Distortions On A Multi-stage Compressor," AIAA Paper 79-7003, 1979.

[12] Hancock, J. P., "Test of a High Efficiency Transverse Fan," AIAA Paper 80-1243, 1980.

[13] Harloff, G. and Wilson, D., "Cross-Flow Propulsion Fan Experimental Development and Finite-Element Modeling," Journal of Aircraft, Vol. 18, No. 4, 1981, pp. 310-317.

[14] Gologan, C., Mores, S., Steiner, H., and Seitz, A., "Potential of the Cross-Flow Fan for Powered-Lift Regional Aircraft Applications," AIAA Paper 2009-7098, 2009.

[15] Dygert, R. K. and Dang, T. Q., "Experimental Investigation of Embedded Cross-Flow Fan for Airfoil Propulsion/Circulation Control," AIAA Paper 2007-3568, 45th AIAA Aerospace Sciences Meeting and Exhibit, Reno, NV, 2007.

[16] Dang, T. and Bushnell, P., "Aerodynamics of Cross-Flow Fans and their Application to Aircraft Propulsion and Flow Control," Progress in Aerospace Sciences, Vol. 45, 2009, pp. 1-29.

[17] Kummer, J., "Simulation of the Cross-Flow Fan and Application to a Propulsive Airfoil Concept," PhD Thesis, Syracuse University, 2006.

[18] Perry, A. T., Ansell, P. J., Kerho, M., Ananda, G., and D'Urso, S., "Design, Analysis, and Evaluation of a Propulsive Wing Concept," 34th AIAA Applied Aerodynamics Conference, D.C., 2016.

[19] Kummer, J. D. and Dang, T. Q., "High-Lift Propulsive Airfoil with Integrated Crossflow Fan," Journal of Aircraft, Vol. 43, No. 4, July-August 2006.

[20] Schreiber, C. W., "Effect of Span Variation on the Performance of a Cross Flow Fan," Masters Thesis, Naval Postgraduate School, June 2006.

[21] Ackeret, J., "Present and future problems in airplane propulsion," Schweizer Bauzeitung 1938, NACA TM no. 976.

[22] Duddempudi, D., "CFD Investigation of Flow over a Generic FanWing Airfoil," AIAA Paper 2005-636, 43rd Aerospace Sciences Meeting and Exhibit, Reno, NV, January 2005.

[23] Kummer, J. D. and Allred, J. B., "Hybrid Axial and Cross-Flow Fan Propulsion for Transonic Blended Wing Body Aircraft," AIAA Paper 2012-3702, 48th Joint Propulsion Conference and Exhibit, Atlanta, GA, July 2012.

[24] Chang, W., "Design and Development of a Rectangular Supersonic Wind Tunnel Facility for the Study of Shock/Boundary Layer Interactions," Masters Thesis, University of Illinois at Urbana-Champaign, 2011.

[25] Farokhi, S., "Aircraft Propulsion," Wiley, New York, 2009.

[26] Tropea, C., Yarin, A., and Foss, J., "Springer Handbook of Experimental Fluid Mechanics," Springer-Verlag, Berlin, 2007.

[27] Jones, B. M., "Measurement of Profile Drag by the Pitot-Traverse Method," British Aeronautical Research Council R & M, 1688, London, England, 1936.

[28] Schlichting, H., "Boundary-Layer Theory," McGraw-Hill Book Company, New York, 8th ed., 2000.

[29] Owen, F. K. and Owen, A. K., "Measurement and Analysis of Circulation Control Airfoils," Applications of Circulation Control Technologies - Progress in Astronautics and Aeronautics, Volume 214.

Appendix: Cross-Flow Fan Power Data

All of the data from the cross-flow fan power measurements are represented in a more user-friendly format in Figure A.1. It is recommended that the user choose the data points with the color most closely matching the desired operating RPM and then perform a simple linear fit to the data to obtain a Mach vs. Power curve for the application of interest. Note that this is the same power data which was represented in Figure 3.7, now shown to allow for easier extraction of data.

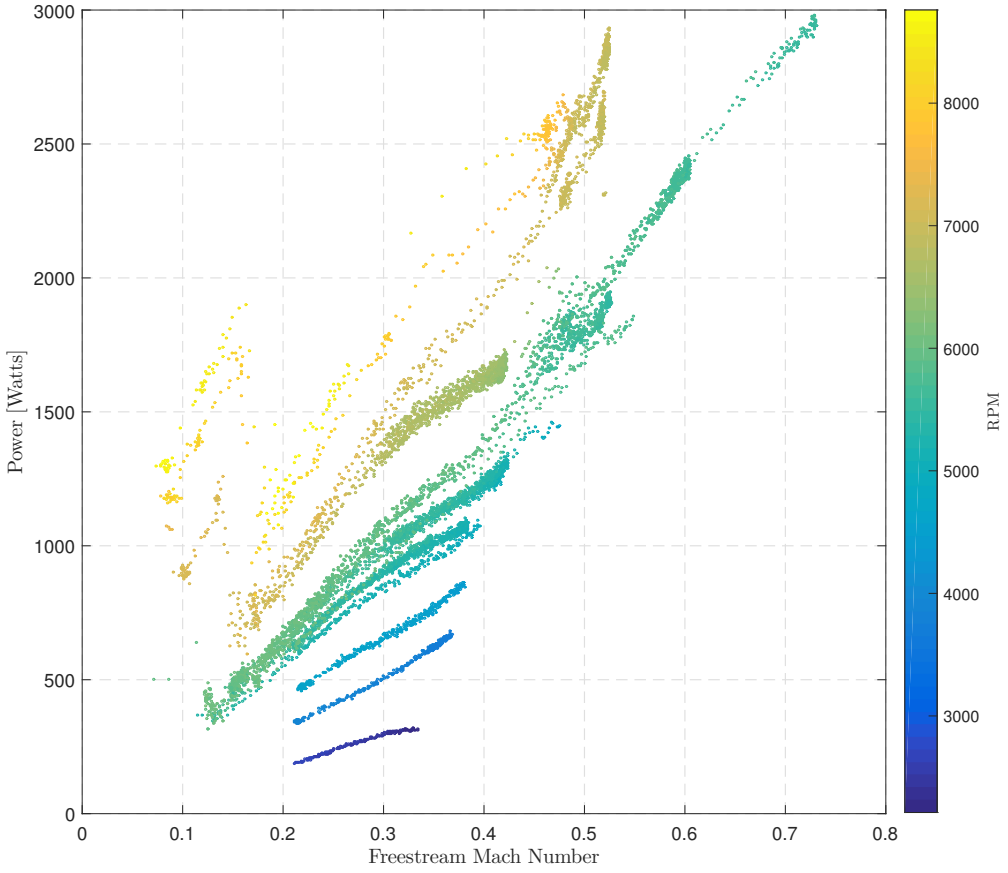

Figure A.1: Cross-flow fan power data.